POLITECNICO DI MILANO
Department of Aerospace Science and Technology

PERFORMANCE-BASED PRELIMINARY SIZING OF AIRCRAFT WITH DISTRIBUTED PROPULSION

Supervisor:
Prof. Lorenzo Trainelli
Co-Supervisors:
Prof. Carlo E. D. Riboldi
Prof. Alberto L. M. Rolando

Master of Science thesis of:
Andrea Matrone 883661

Academic Year 2019/2020

Abstract

In recent years, an increased focus on electric propulsion applications for both ground vehicles and airplanes has been observed in recent years, thanks to more reliable and performing batteries and electric motors. Electric propulsion offers fundamentally different characteristics that enable distributed propulsion solutions, thanks to their scalable nature, without significant losses in efficiency or specific power. The present work focuses on establishing a general procedure to design an electric aircraft with a distributed electric propulsion (DEP) system from a conceptual point of view and to assess energy consumption and other advantages. A DEP model predicting the increase of aerodynamic coefficients with respect to the conventional case is developed and validated. Based on that, a procedure for the performance-based sizing of DEP aircraft with an arbitrary number of propulsive units is established and validated for the case of the NASA X-57 Maxwell aircraft. This new technique is implemented in the Hyperion tool, dedicated to electric and hybrid-electric aircraft preliminary sizing. As a final application, four varied configurations of the NASA X-57 are analyzed, highlighting strengths and weaknesses of DEP solutions.

Keywords: Electric Aircraft, Distributed Electric Prolusion, Sizing Matrix Plot, Hyperion Program.

Sintesi

Un aumento nell'interesse su applicazioni elettriche alla propulsione sia per veicoli di terra che per aeroplani è stato osservato nel corso degli ultimi anni, grazie a batterie e motori elettrici più affidabili e performanti. La propulsione elettrica offre caratteristiche fondamentalmente diverse dalla propulsione aerea convenzionale che permettono lo sviluppo della propulsione distribuita per via del ridimensionamento dei motori senza una significativa perdita di efficienza o potenza specifica. Il presente lavoro si focalizza sullo stabilire una procedura generale per la progettazione concettuale di un velivolo elettrico che utilizza la configurazione DEP e di valutare il sistema di dimensionamento preliminare per studiare i vantaggi strutturali ed energetici. Un modello DEP per la stima dell'aumento dei coefficienti aerodinamici con l'implementazione della propulsione distribuita è stato sviluppato e convalidato utilizzando velivoli elettrici esistenti come riferimento, effettuando un confronto sia con analisi CFD sia con dati sperimentali. Il dimensionamento preliminare è stato condotto tramite il modello DEP in modo da generare una procedura standard nel caso di un aereo che utilizza la propulsione distribuita, valutando i vantaggi che si possono ottenere con l'aumento del numero di motori elettrici sulla superficie alare. La fase di dimensionamento preliminare è stata convalidata studiando il caso dell'aereo elettrico NASA X-57 Maxwell. La procedura sviluppata per la grandezza dell'ala e la potenza dei motori con DEP è stata inserita nel programma Matlab chiamato Hyperion, utilizzato per il dimensionamento preliminare di progetto di velivoli elettrici. E' stato svolto il dimensionamento preliminare di progetto per quattro configurazioni differenti relative all'aereo NASA X-57 Maxwell, evidenziando pregi e difetti della propulsione distribuita.

Parole chiave: Aereo Elettrico, Propulsione Elettrica Distribuita, Dimensionamento Preliminare di Progetto, Programma Hyperion.

Table of contents

List of illustrations

List of tables

List of symbols

Symbols	Names	Units
α	Angle of Attack	deg
θ	Angle that the slipstream makes with the propeller	deg
Γ	Circulation	m^2/s
ρ	Density	kg/m^3
∞	Freestream	–
μ	Friction coefficient for runway surface	–
ω	Induced velocity	m/s
χ	Ratio between T_{DP} and T	–
μ	Ratio of the freestream velocity to slipstream velocity	–
Λ	Ratio of the slipstream width to height	–
β	Slipstream height ratio	–
$\Lambda_{c/2}$	Half-chord wing sweep angle	deg
ΔC_D	Augmented Drag coefficient due to DEP	–
ΔC_L	Augmented Lift coefficient due to DEP	–
ρ_{CR}	Cruise density	kg/m^3
ρ_{TO}	Take-off density	kg/m^3
α_i	Induced angle of attack	deg
α_{twist}	Twist angle relative to wing horizontal frame	deg
ΔY	Fraction of wing span occupied by the DP array	m
Δy	Spanwise separation parameter	m
a	Speed of sound	m/s
a'	Experimentally-determined constant	–
A	Tip vortex contraction coefficient	–
a_o	Lift curve slope	–
a_P	Axial induction factor at propeller disk	–
AR	Wing aspect ratio	–
AR_μ	Aspect ratio from Jameson's theory	–
a_w	Axial induction factor at wing leading edge	–
B	Number of blades	–
b	Wing span	m
b_e	Effective wing span	m

Symbols	Names	Units
b_f	Fuselage width	m
c	Wing chord length	m
c_o	Non-dimensional wing chord	–
$C_{D\,1}$	Drag coefficient in climb configuration	–
$C_{D\,CR}$	Drag coefficient in cruise configuration	–
C_D	Drag coefficient	–
C_d	Section drag coefficient	–
$C_{D\,TO}$	Drag coefficient in take-off configuration	–
$C_{D\,u}$	Drag coefficient unblown wing	–
C_{Do}	Drag coefficient due to friction and dynamic pressure	–
C_{Di}	Drag coefficient induced by the lift force	–
c_f	Sectional skin friction coefficient	–
$C_{L\,1}$	Lift coefficient in climb configuration	–
$C_{L\,CR}$	Lift coefficient in cruise configuration	–
C_L	Lift coefficient	–
$C_{L\,R}$	Lift coefficient at take-off rotation	–
C_l	Section Lift coefficient	–
$C_{L\,TO}$	Lift coefficient in take-off configuration	–
$C_{L\,u}$	Lift coefficient unblown wing	–
C_p	Pressure coefficient	–
CGR	Climb gradient	–
D	Drag	N
D	Propeller diameter	m
D_1	Contracted slipstream diameter	m
e	Oswald span efficiency factor	–
ep	Effective value aft of the propeller	–
g	Gravitational acceleration	m/s^2
h	Geopotential height	m
H	Induced velocity parameter	–
i_p	Propeller slipstream inclination angle	deg
J	Propeller advance ratio	–
k	Circulation multiplier	–
K	Induced drag factor	–
K_1, K_2	Tip vortex translation coefficients	–
K_L	Lift multiplier	–

Symbols	Names	Units
L	Lift	N
L/D	Lift-to-Drag ratio	—
M	Mach number	—
M_a	Non propulsive airframe mass	kg
M_b	Battery pack mass	kg
M_{HLM}	High-lift motor mass	kg
M_{TM}	Wingtip motor mass	kg
M_{RM}	Motor mass at wing root	kg
MCP	Maximum continuous power	kW
n	Blade rotational frequency	rad/s
N	Number of propellers	—
$OXYZ$	Fixed coordinate system	—
p	Propeller	—
P_b	Engine power	W
q	Dynamic pressure	Pa
q	Velocity induced by the wing	m/s
R	Propeller radius	m
R_o	Radius of propeller hub	m
Re	Reynolds number	—
ROC	Rate of climb	m/s
r_t	Radial contraction of the tip vortex in the propeller wake	m
r_v	Radial contraction of a vortex from the point x on the blade	m
s	Increase in velocity in the fully contracted slipstream	m/s
s	Non-dimensional wingspan	—
$\check{S}$	Point on to the propeller blade	—
S	Wing surface	m²
S_L	Landing distance	m
S_{LG}	Landing ground run	m
S_{TO}	Take-off run	m
S_{TOG}	Take-off ground	m
SOC	State of charge	—
t	Non-dimensional wing chord	—
T	Thrust	N
T_c	Non-dimensional thrust coefficient of single propeller	—

Symbols	Names	Units
T_{DP}	Thrust of the DP array	N
$Þ$	Blade angle at 0.7 of the blade radius	deg
u, v, w	Velocity components	m/s
V	Velocity	m/s
V_∞	Freestream velocity	m/s
V_{CR}	Cruise speed	m/s
$V_{CR\,MAX}$	Maximum cruise speed	m/s
V_{ia}	Velocity induced by sheet vortices	m/s
V_{il}	Velocity induced by free vortices	m/s
V_j	Slipstream velocity	m/s
V_S	Stall speed	m/s
W_L	Aircraft landing weight	N
W_{TO}	Aircraft maximum take-off weight	N
W_{TO}/P_b	Power loading	s/m
W_{TO}/S	Wing loading	N/m²
x	Axial propeller position	m
x_C	Axial propeller position as function of chord	—
x_t	Axial convection of propeller tip vortex	m
x_v	Axial convection of any vortex of the propeller wake	m
y	Radial propeller position	m
δ	Ratio between propeller radius and wing span	—
δ	Ratio between shaft power ant maximum shaft power	—
ζ	Geometric parameter related to the position of the propeller	—
η_P	Propulsive efficiency	—
λ	Empirical factor from Smelt and Davies' theory	—
λ'	Empirical constant	—
ξ	Fraction of blade radius	—
ξ	Lateral clearance between two propellers	—
τ	Angle at wing trailing edge outer	deg
φ	Propeller installation angle	deg
ψ	Azimuth coordinate in the propeller wake	deg
Ω	Propeller rotational speed	rad/s

List of acronyms

Acronyms	Meaning
AEO	All Engines Operative
AOA	Angle of Attack
BEM	Boundary Element Method
CFD	Computational Fluid Dynamics
CR	Cruise
CS	Certification Specification
CGR	Climb Gradient
DEP	Distributed Electric Propulsion
DEP-AO	Distributed Electric Propulsion – Always On
DP	Distributed Propulsion
EASA	European Aviation Safety Agency
FAA	Federal Aviation Administration
FAR	Federal Aviation Regulation
FUN3D	Fully Unstructured Navier-Stokes
FWA	Free Wake Analysis
HEIST	Hybrid-Electric Integrated Systems Testbed
HEP	Hybrid-Electric Propulsion
LEAPTech	Leading Edge Asynchronous Propeller Technology
LND	Landing
MTOW	Maximum Take-Off Weight
NACA	National Advisory Committee for Aeronautics
NASA GAW-1	National Aeronautics and Space Administration General Aviation Airfoil
NASA	National Aeronautics and Space Administration
OEI	One Engine Inoperative
ROC	Rate Of Climb
SCEPTOR	Scalable Convergent Electric Propulsion Technology Operations Research
SMP	Sizing Matrix Plot
STAR-CCM+	Simulation of Turbulent flow in Arbitrary Regions - Computational Continuum Mechanics
TO	Take-Off
TOP_{23}	Take-Off Parameter CS Part 23
TOP_{25}	Take-Off Parameter CS Part 25
USM3D	Unstructured Software System

Introduction

The use of electric motors for aircraft propulsion is a topic of increasing interest in the aviation community, largely due to the significant increase in the efficiency of such motors with respect to the traditional internal combustion engines. For light aircraft, these motors are more compact, lighter, quieter, and more reliable than the reciprocating combustion engines that are currently used for primary propulsion. The relatively scale-invariant nature of efficiency respect to power level (and motor size) tends to enable more distributed propulsion architectures than seen with typical thermodynamic cycles used for propulsion. In particular, Distributed Electric Propulsion (DEP) architectures can yield a net benefit in total efficiency due to synergistic airframe-propulsive coupling [3]. This further reduces the penalty associated with a heavier on-board energy storage mechanism, as the overall aerodynamic efficiency can be improved. National Aeronautics and Space Administration (NASA) has been investigating the benefits of DEP technology, including development of ground test articles, and more recently on the design of a flight demonstrator to establish and verify some of the potential benefits associated with this technology [1, 2].

The purpose of this study is therefore to develop a new conceptual design method, which sizes the wing and propulsion system for aircraft featuring with DEP system.

First, an innovative DEP model is developed and validated: the increase of aerodynamic coefficients with DEP must be estimated in order to incorporate the aero-propulsive interaction effects in the design process. With the purpose to assemble a valid airframe-propulsion-system interaction model, the DEP model involves a series of assumptions and semi-empirical methods specifically focused on aircraft featuring leading edge DP.

Secondly, the traditional preliminary sizing methodology [26, 28, 33] is modified in order to consider the effect of aerodynamic coefficients computed through the DEP model. This leads to a set of modified aircraft performance equations, which are collected in a wing loading – power loading diagram called Sizing Matrix Plot (SMP) in order to provide a visual representation of the design space.

Very few and mostly recent preliminary sizing methods are available in literature for pure-electric and hybrid-electric aircraft configurations, especially embedding DEP capabilities [6, 34]. While these procedures usually provide aero-propulsive interaction estimation methods, they build on textbooks (mainly [26, 28, 33]) for what concerns flight performance and mission requirements (take-off distance, best rate of climb, high speed cruise, stall speed and landing). The added value of this work is to accurately investigate how DEP influences every single mission requirement equation and highlight the changes in the feasible design space within the SMP.

Finally, the new sizing procedure for wing area and engine sizing is implemented in the Hyperion program [30, 35], a tool for electric aircraft preliminary sizing developed at Politecnico di Milano.

The new sizing procedure for wing area and engine sizing is implemented in Hyperion program, a tool for electric aircraft preliminary sizing. The new DEP preliminary design phase is evaluated for four different configurations of the NASA X-57 Maxwell aircraft, in order to study how the DEP influences the design of the vehicle and the complete mission profile. The NASA X-57 Maxwell aircraft will be the reference aircraft for analysis and comparison since it is the NASA's first all-electric experimental

aircraft with the goal to advance certification approaches for distributed electric propulsion in emerging electric aircraft markets.
With the proposed DEP preliminary design phase, it is possible to rapidly explore the design space, to estimate the optimal wing loading and power loading, to carry out sensitivity analyses and to evaluate the impact of DEP on the overall performance of the aircraft. Even though the application described in this work will focus on wing-mounted DP systems, the rationale followed in this process can be extended to other novel propulsor layouts such as tip-mounted propellers.

Structure of the work

Chapter 1 – Problem description. The DEP is introduced and a literature survey is carried out to compare the estimation of the increment in aerodynamic coefficients for different methods and approach developed by various authors.
Chapter 2 – Development and validation of DEP model. Considering theoretical analyses and studies, the DEP model is developed in order to compute the increment in aerodynamic coefficients with DEP system. The new model is tested with a validation phase where it is analysed through a comparison with experimental results and CFD results.
Chapter 3 – Preliminary sizing for DEP aircraft. The possibility to apply the DEP model to the generation of an innovative sizing matrix plot is discussed. For each aircraft performance requirement it is defined a new formulation for propeller-driven aircraft with DEP system, generating the new DEP preliminary sizing phase.
Chapter 4 – Application of DEP preliminary design phase. The new sizing procedure is implemented in Hyperion program, a tool for electric aircraft preliminary sizing. The DEP preliminary design phase is evaluated considering four different configurations of the NASA X-57 aircraft, studying how the DEP influences the design of the vehicle and performances.
Chapter 5 – Conclusions and future work. Outcomes and results of this work are highlighted and possible future developments of the DEP preliminary design phase are discussed.

Chapter 1 – Problem Description

In this first chapter, the Distributed Electric Propulsion (DEP) is described to highlights the advantages that this type of powered flight propulsion system can generate during a typical mission profile. After a literature survey on DEP system, an illustration of models capable to estimate the increments in aerodynamic coefficients is given, taking into account existing studies and discussing the methods proposed in the literature. In the last part of the chapter, a comparison between the most interesting models analysed is offered, in order to select the best approach to the prediction of the variation in aerodynamic performance with DEP system when compared to the conventional case.

1.1 Distributed Electric Propulsion

In the last decade, aircraft concepts using electricity for some or all of their propulsive power have captured the public imagination and garnered great attention in the popular press. Several start-up ventures have been established, proposing aircraft concepts with DEP.
DEP is a type of powered flight propulsion system for fixed-wing aircraft in which engines are distributed about a vessel. Its goal is to increase performance in fuel efficiency, emissions, noise, landing field length and handling performance. DEP is typically accomplished by spanwise distribution of partially or fully embedded multiple small propellers or fans along the wing. An example is given in Figure 1.1.

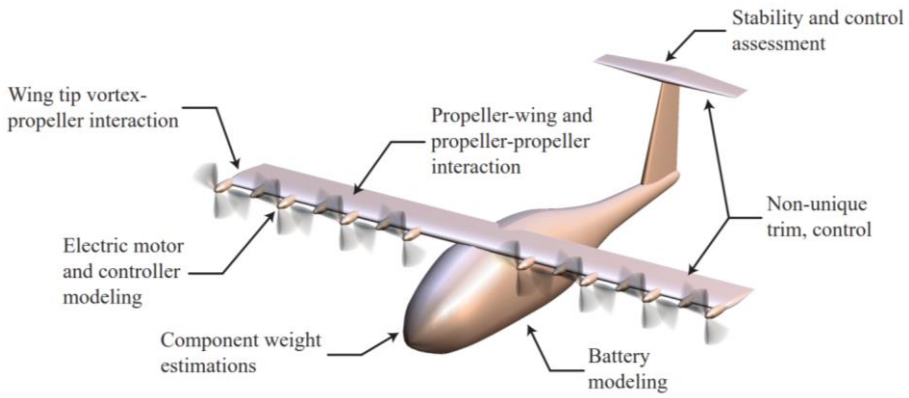

Figure 1.1: Notional distributed propeller configuration [11].

Electric propulsion is an enabler of distributed propulsion, given its inherent ability to scale motors without a significant loss of efficiency or specific power. Electric motors are physically smaller, making wingtip and tailcone installations feasible (as in the NASA X-57 Maxwell aircraft). Since the boundary layer extends to a small, finite thickness past the wing or fuselage, numerous small electric fans may cover larger portions of the wing and body and ingest a higher fraction of boundary layer flow than a few larger-diameter turbine propulsors.

There are two proposed aerodynamic benefits of DEP: installation drag reduction and high lift augmentation [5]. Engine nacelles and pylons introduce propulsion installation drag, comprised of friction, interference, and wave drag. Along with nacelle and fan weight, propulsive aerodynamic drag serves as a practical limit on turbofan bypass ratio. The cited studies showed an 8% installed drag reduction by embedding distributed propellers in the wing on a transonic military transport concept. Engine installations embedded in the fuselage surface may save wetted area equivalent to nearly half of a typical podded nacelle.

High-lift augmentation through distributed propulsion reduces cruise drag by enabling higher wing loading (and therefore, lower wetted wing area and viscous drag). With higher overall lift coefficient C_L, approach speed and take-off field length constraints can be met with a smaller wing. Stoll et al. [4] show this advantage with a comparison between Cirrus SR22 aircraft and the Leading Edge Asynchronous Propeller Technology (LEAPTech) aircraft. The LEAPTech wing is analysed using steady Computational Fluid Dynamics (CFD) with propellers modelled as actuator disks. CFD results of the resulting wing design curve show a $C_{L\,MAX}$ of over 5.2 and a relatively flat C_L - α curve due to the influence of the propeller downwash on the effective Angle Of Attack (AOA) experienced by the wing.

A similar CFD analysis, although without propulsion effects, was performed on the entire LEAPTech aircraft in cruise conditions, resulting in a lift-to-drag ratio L/D of 22.4, which compares favourably to the Cirrus SR22 where L/D is 11.

The propellers along the leading edge of the wing are used to enhance high-lift performance by increasing the dynamic pressure over the wing at low speeds, thus enabling a smaller wing. Given identical drag polars, the maximum lift-to-drag ratio L/D_{MAX} occurs at a higher velocity: this value (and therefore aerodynamic efficiency) at higher speeds are generally higher for smaller wings [3].

In order to have a complete picture of these benefits, Figure 1.2 shows the increase of aerodynamic coefficients with DEP technology for the NASA X-57 Maxwell aircraft using CFD methods [1]. The corresponding operating conditions are: V=58 KTAS, M=0.0878, Re=1.33e^6, h=0 m. For the blown case, high-lift wing power conditions refer to a power setting of 4548 RPM, 164.4 hp (13.7 hp/prop).

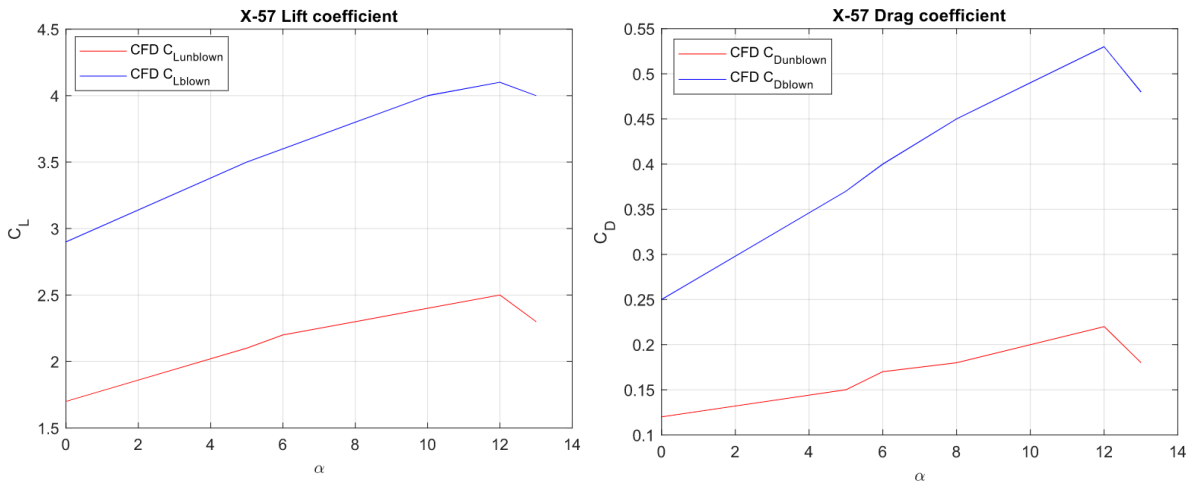

Figure 1.2: Aerodynamic coefficients for the NASA X-57 wing with high-lift system and wingtip nacelles [1].

For this case, when the DEP system is operating with total thrust of 2652.92 N, the conservative estimate of effective $C_{L\ MAX}$ is 4.202 at AOA of 12° with the blown, high-lift wing. Therefore, the conservative estimate of the lift augmentation from the high-lift DEP system is 1.76, calculated from the ratio of the DEP blown wing $C_{L\,MAX}$ of 4.202 to the unblown wing $C_{L\,MAX}$ of 2.439.

1.2 Models to estimate ΔC_L and ΔC_D

For the early-phase design of an electric aircraft, it is necessary to understand how aerodynamic coefficients vary with DEP and so how lift augmentation from high-lift propellers can be rapidly assessed to facilitate conceptual design. To this end, the following provides an overview of the most interesting applicable aerodynamic models.

1.2.1 Smelt and Davies's approach

Smelt and Davies [9] developed a simple method to obtain the lift augmentation from upstream propellers on a downstream wing in the 1930s. Their theory relies on the same principles of classical momentum theory to analyse the propeller action and their slipstreams; it ignores any influence of the wing on the propeller and is only applicable to relatively lightly loaded propellers and wings without flaps. Their work is widely cited and appears to be still generally accepted as a reasonable first-order estimate of propeller lift augmentation (within the limits of the cited assumptions).

Smelt and Davies noticed that previously developed theories could provide reasonable results for wings with relatively small chord lengths in comparison to the propeller slipstream diameter, but these theories would fail when considering wings with larger chords. Based on their observations of experimental results and their understanding of the inner physics, Smelt and Davies postulated maximum and minimum values for the increase in lift from a wing in a propeller slipstream and developed a relationship based on the aspect ratio of the wing in the slipstream that dictated where between these two extremes a particular configuration would fall.

The maximum increase in lift is theorized to occur when the chord is small in comparison to the slipstream diameter, and the resulting maximum lift increase is proportional to the change in the dynamic pressure in the slipstream. They represent this lift change as in the following equation, where C_{L0} is the lift coefficient without propeller blowing, D_1 is the contracted slipstream diameter and the factor s is the increase in velocity in the fully contracted slipstream such that the local flow velocity at a given distance aft of the disk is $V_\infty(1+s)$.

$$\Delta C_L = C_{L0}\frac{D_1 c}{S}((1+s)^2 - 1) \cong C_{L0}\frac{D_1 c}{S}2s \tag{1}$$

The approximate relationship holds for lightly loaded propellers (relatively small values of s). The minimum increase in lift would occur when the slipstream diameter is small in comparison to the wing

chord. This minimum lift increase would be proportional to the velocity increase in the slipstream, which can be represented mathematically as the following equation and is equivalent to assuming that the circulation around the wing is unchanged from the case without blowing.

$$\Delta C_L = C_{L0} \frac{D_1 c}{S} s \tag{2}$$

They justify the assumption of an unchanged wing circulation by considering the shed vortices from the wing. Near the edges of the slipstream boundary, the wing will shed stronger vortices than near the centre of the blown portion. These vortices will induce downwash that reduces the effective angle of attack of wing sections near them. As the slipstream width decreases, these stronger vortices move closer to the propeller centreline and have a larger impact on the flow over the wing. The form of the previous two equations are such that they can be represented as an unique equation, where the λ parameter will vary from a minimum value of 1 to a maximum of 2 to represent these equations.

$$\Delta C_L = C_{L0} \frac{D_1 c}{S} \lambda s \tag{3}$$

To determine an appropriate value for λ based on a given geometry, Smelt and Davies developed an empirical relationship between λ and the aspect ratio of the wing immersed in the slipstream.

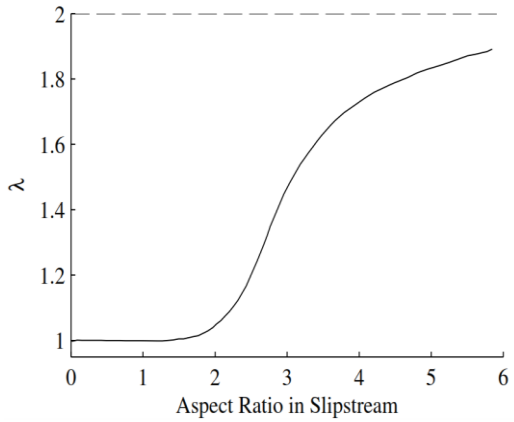

Figure 1.3: Empirical factor describing the amount of lift augmentation from propellers [8].

There is no discussion of how this relationship is precisely obtained, but it shows good agreement with the experimental data presented in their paper. As can be seen from Figure 1.3, there is a sigmoid-like variation of λ with the aspect ratio in the slipstream. The value of λ is effectively 1 from aspect ratios of zero to approximately 2. There is a sharp rise in λ from aspect ratios of 2 to approximately 4, and then the rate of increase in λ begins to decrease. Smelt and Davies only show the relationship between λ and aspect ratio in the slipstream for aspect ratios of up to 6, but it can be assumed that the value of $\lambda = 2$ is only achieved in the limit as the aspect ratio becomes infinitely large.

Smelt and Davies also present a relationship describing how the lift varies as the angle the propeller slipstream makes with the freestream, θ_0, changes. First, they recognize that the angle that the slipstream initially makes with the propeller, θ_0, will be reduced by some amount due to viscous forces by the time it encounters the wing. They present the following equation to calculate the effective reduction of this angle from θ_0 to θ as a function of the distance aft of the propeller, x, and the propeller diameter, D.

$$\frac{1}{\theta^{0.8}} = 0.016\frac{x}{D} + \frac{1}{\theta_0^{0.8}} \tag{4}$$

Practically, this results in a very small reduction in the angle unless both the initial angle and the distance are relatively large. With the value of θ in hand, they estimate the total increase in lift from an inclined slipstream with the following equation, where a_o is the lift curve slope of the wing section airfoil and λ' is an empirical constant.

$$\Delta C_L = C_{L0}\frac{D_1 c}{S}s(\lambda C_{L0} - \lambda' a_0 \theta) \tag{5}$$

From their experiments, they determine that a value of λ'=0.6 provided reasonable results. Unfortunately, there is no discussion of how the empirical constant λ' should be selected in general, though they imply that the value of 0.6 should be sufficient so long as propeller inclinations within the ranges of their experiments (where the propeller makes no more than a 10° angle with the freestream) are analysed.

1.2.2 Jameson's approach

Jameson [10, 14] is interested in studying STOL aircraft concepts with multiple propellers. He considered the situation where the propeller slipstreams would effectively merge to form a single, wide slipstream. In his analysis, Jameson assumes that the velocity in the propeller slipstreams is uniform with a velocity of V_j purely in the axial direction. The swirl from the propellers is neglected, and the slipstream extends aft parallel to the free stream direction (i.e., it is not deflected by the wing). Furthermore, the flow is assumed inviscid and incompressible, and the height of the slipstream must be greater than half the wing's chord length.

Although Jameson studies the coupling of his method with both lifting line theory and slender body theory to predict wing lift, these solutions include Fourier series, which require computation to practically resolve into a solution due to their infinite summations. However, Jameson was able to determine an analytic solution to the potential equations for a case where the slipstreams from the propellers merge to form a large elliptic slipstream that extended beyond the wing tips, so that the tips are located at the foci of the ellipse and the wing downwash is constant. Although this case is not likely

to occur in practice, the method is sufficiently simple that it may help build insight into the general trades present in aircraft with many propellers.

To present the equations, Jameson defines μ as the ratio of the freestream velocity to slipstream velocity ($\mu = V_\infty/V_j$), and Λ represents the ratio of the slipstream width to height. Ultimately, the effect of the slipstream can be approximated as an effective reduction in the aspect ratio from the baseline value, AR, to AR_μ, which can be calculated from the following equation.

$$AR_\mu = AR\frac{1+\Lambda\mu^2}{\Lambda+\mu^2} \tag{6}$$

If the wing has a large aspect ratio, then lifting line theory will provide reasonable results for aggregate wing lift and drag. Furthermore, if the lift and drag coefficients are non-dimensionalized by the velocity in the jet rather than the freestream, the equations take the same form as with conventional lifting line theory. The lift coefficient can be found from the following equation, where α is the angle of attack as measured from the zero-lift line. This equation effectively models the jet as a modification to the lift curve slope of the airfoil.

$$C_{Lj} = \left(\frac{a_0}{1+\frac{a_0}{\pi AR_\mu}}\right)\alpha = C_L\mu^2 \tag{7}$$

The induced angle of attack can be found from the following equation.

$$\alpha_i = \frac{C_{Lj}}{\pi AR_\mu} \tag{8}$$

Finally, the induced drag can be determined following the process.

$$C_{Dij} = \alpha_i C_{Lj} = \frac{{C_{Lj}}^2}{\pi AR_\mu} = \mu^2 C_{Di} \tag{9}$$

1.2.3 Patterson's approach

Patterson and German [7, 8, 11] derive a two-dimensional model for predicting wing lift augmentation from high-lift propellers. This approach considers configurations in which propellers are installed upstream of a wing, and the two-dimensional geometry under consideration is shown in the following figure. The figure shows the orientation of the freestream velocity vector $\boldsymbol{V_\infty}$, the propeller disk plane, the slipstream velocity from the propeller $\boldsymbol{V_p}$, and the local wing section chord line relative to the reference chord line of the wing. The airfoil at any given wing section may be twisted from the wing reference chord by an angle α_{twist}, and positive twist is shown in the figure. The propeller is located

forward of the wing and is inclined at an angle of φ relative to the wing frame's vertical; a positive φ is shown in the figure and indicates an upward tilt of the resultant thrust vector from the propeller relative to the wing reference chord.

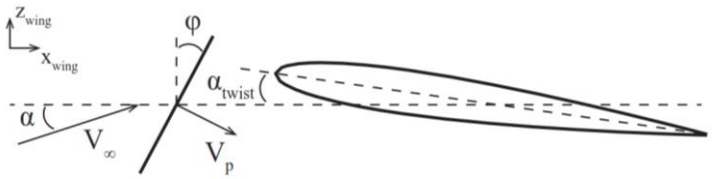

Figure 1.4: A two-dimensional cross section of the geometry under consideration relative to the wing reference frame [7].

The geometry in Figure 1.4 can also be formulated relative to the local airfoil chord line as shown in Figure 1.5.

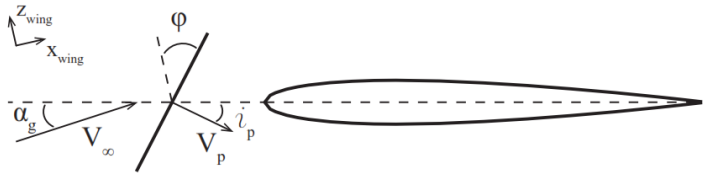

Figure 1.5: Orientation of freestream velocity and propeller disk with respect to a local airfoil section [7].

In the local reference frame of the airfoil sections, only two angles, α_g and i_p, describe the direction of the incoming velocity vectors $\boldsymbol{V_\infty}$ and $\boldsymbol{V_p}$, respectively. The local geometric angle of attack, α_g, can be written in terms of the local twist and the wing angle of attack.

$$\alpha_g = \alpha + \alpha_{twist} \tag{10}$$

Consistent with momentum theory, it is possible to model the propeller slipstream as a uniform velocity flow oriented in the direction of the disk normal axis. With the assumption that $\boldsymbol{V_p}$ is perpendicular to the propeller disk, the incoming angle of the slipstream, i_p, can be written in terms of the local twist and the propeller installation angle.

$$i_p = \varphi - \alpha_{twist} \tag{11}$$

For two-dimensional geometry, reference is made in terms of the local variables i_p and α_g as opposed to the variables φ and α. The slipstream from the propeller causes a change in the effective angle of attack of the airfoil as illustrated in Figure 1.6. The effective angle of attack behind the propeller, α_{ep}, is defined

between the chord line and the effective velocity $\boldsymbol{V_{ep}}$ behind the prop, which is a vector sum of the freestream and slipstream velocities ($\boldsymbol{V_{ep}} = \boldsymbol{V_\infty} + \boldsymbol{V_p}$).

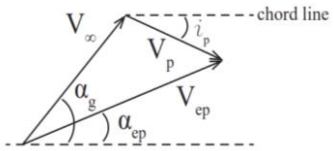

Figure 1.6: Vector diagram showing the effective angle of attack behind the prop resulting from the axial component of the propwash over the wing [7].

An expression for the effective angle of attack of the airfoil section behind the propeller in terms of the geometric angle of attack, the freestream velocity, the velocity of the slipstream, and the local slipstream inclination angle is given in Equation 12. This relationship is derived from the geometry presented in Figure 1.6:

$$\tan \alpha_{ep} = \frac{V_\infty \sin \alpha_g - V_p \sin i_p}{V_\infty \cos \alpha_g + V_p \cos i_p} \tag{12}$$

For small angles of attack and small inclination angles, the previous equation can be reduced to the following equation:

$$\alpha_{ep} \cong \frac{V_\infty \alpha_g - V_p i_p}{V_\infty + V_p} = \frac{\alpha_g - (V_p/V_\infty) i_p}{1 + (V_p/V_\infty)} \tag{13}$$

Finally, the magnitude of the effective local velocity behind the propeller can also be determined from the geometry as in Equation 13:

$$V_{ep} = \sqrt{V_\infty^2 + 2V_\infty V_p \cos(\alpha_g + i_p) + V_p^2} \tag{14}$$

1.2.3.1 Two-dimensional model

Considering the case in which the propeller is inclined upward, $i_p > 0$, the circulation is expected to decrease relative to the unblown wing because $\omega_{new} < \omega_\infty$. Additionally, the angle of attack of the airfoil is decreased ($\alpha_{ep} < \alpha_g$). If the circulation strength decreases by some factor k (where $k < 1$), then Γ_{new} corresponds to $k\Gamma_\infty$ and the percentage increase in the section lift can be expressed as in the following equation.

$$\frac{\Delta C_l}{C_{l\infty}} = k \frac{V_{ep}}{V_\infty} - 1 \tag{15}$$

Since the induced velocity from a point vortex is directly proportional to the vortex strength, k can be expressed in terms of induced velocity ratio as shown in equation 16.

$$k = \frac{\omega_{new}}{\omega_{\infty}} = 1 - \frac{V_p \sin i_p}{V_{\infty} \sin \alpha_g} \tag{16}$$

The percentage change in the lift can then be expressed in terms of the freestream velocity, local slipstream velocity, local propeller inclination angle, and geometric angle of attack.

$$\frac{\Delta C_l}{C_{l\infty}} = \left(1 - \frac{V_p \sin i_p}{V_{\infty} \sin \alpha_g}\right) \frac{\sqrt{V_{\infty}^2 + 2V_{\infty}V_p \cos(\alpha_g + i_p) + V_p^2}}{V_{\infty}} - 1 \tag{17}$$

This equation is valid also for the case in which the propeller normal axis is aligned with the local aifoil chord ($i_p = 0$) and the case in which the propeller normal axis is inclined downward below the freestream velocity.

The above analysis has assumed that the airfoil section is completely immersed in a very wide slipstream flow. However, the diameter of the propeller will likely not be large compared to the wing chord. Additionally, the contraction of the slipstream aft of the propeller will further reduce the effective diameter of the slipstream relative to the diameter of the propeller. In general, it is of interest to be able to study configurations in which the diameter of the propeller is smaller than the wing chord. In these cases, the assumptions made in the simple models presented above will not directly hold and must be modified. To account for the effects of finite slipstream height, the theory presented in this section is modified by applying a multiplicative factor β, to the propeller slipstream velocity $\boldsymbol{V_p}$. This factor is bounded between zero and one with $\beta = 0$ corresponding to $h/c = 0$ and $\beta = 1$ strictly holding only in the limit as h/c approaches infinity.

A surrogate model for β is developed as a function of three design parameters:

1. The ratio of the disk radius to the chord of the airfoil (R/c).
2. The velocity of the contracted slipstream far downstream of the disk.
3. The distance upstream of the leading edge the disk is placed.

For the model developed, the vertical height of the disk and the angle of the disk relative to the freestream are kept constant. To make data obtained from simulations useful in a computational design environment, the surrogate model is fit to the data. To fit the surrogate model, four separate fourth-order polynomials in the form of the following equation are fit to the data at V_{ep}/V_{∞} values of 1.25, 1.5, and 2.0 resulting in 12 total polynomials.

$$\beta = f_0 + f_1\left(\frac{R}{c}\right) + f_2\left(\frac{R}{c}\right)^2 + f_3\left(\frac{R}{c}\right)^3 + f_4\left(\frac{R}{c}\right)^4 \tag{18}$$

Next, the variation of the each of the coefficients ($f_0, f_1, \ldots, f_4$) is approximated as a second order response surface equation of the axial propeller position as function of chord (x/c) and V_{ep}/V_∞ variables as shown in the following equation.

$$f_i = k_{i0} + k_{i1}\left(\frac{x}{c}\right) + k_{i2}\left(\frac{x}{c}\right)^2 + k_{i3}\left(\frac{x}{c}\right)\left(\frac{V_{ep}}{V_\infty}\right) + k_{i4}\left(\frac{V_{ep}}{V_\infty}\right) + k_{i5}\left(\frac{V_{ep}}{V_\infty}\right)^2 = K_i\, X \tag{19}$$

The resulting values of the coefficient row vectors are given in the next equations and these thirty numbers define the surrogate model.

$$\begin{cases} K_0 = [0.378269 \;\; 0.748135 \;\; -0.179986 \;\; -0.056464 \;\; -0.146746 \;\; -0.015255] \\ K_1 = [3.071020 \;\; -1.769885 \;\; 0.436595 \;\; 0.148643 \;\; -0.9889332 \;\; 0.197940] \\ K_2 = [-2.827730 \;\; 2.054064 \;\; -0.467410 \;\; -0.277325 \;\; 0.698981 \;\; -0.008226] \\ K_3 = [0.997936 \;\; -0.916118 \;\; 0.199829 \;\; 0.157810 \;\; -0.143368 \;\; -0.057385] \\ K_4 = [-0.127645 \;\; 0.135543 \;\; -0.028919 \;\; -0.026546 \;\; 0.010470 \;\; 0.012221] \end{cases} \tag{20}$$

The final surrogate model can be represented in a single equation.

$$\begin{cases} \beta = K_0 X + K_1 X\left(\frac{R}{c}\right) + K_2 X\left(\frac{R}{c}\right)^2 + K_3 X\left(\frac{R}{c}\right)^3 + K_4 X\left(\frac{R}{c}\right)^4 \\ X = \left[1 \;\; \frac{x}{c} \;\; \left(\frac{x}{c}\right)^2 \;\; \left(\frac{x}{c}\right)\left(\frac{V_{ep}}{V_\infty}\right) \;\; \left(\frac{V_{ep}}{V_\infty}\right) \;\; \left(\frac{V_{ep}}{V_\infty}\right)^2\right]^T \end{cases} \tag{21}$$

The percentage change in the lift should be modified to include the β parameter. The inclusion of this parameter will reduce the lift increase predicted in all circumstances.

$$\frac{\Delta C_l}{C_{l\infty}} = \left(1 - \frac{\beta V_p \sin i_p}{V_\infty \sin \alpha_g}\right) \frac{\sqrt{V_\infty^2 + 2\beta V_\infty V_p \cos(\alpha_g + i_p) + (\beta V_p)^2}}{V_\infty} - 1 \tag{22}$$

At different locations behind a propeller, the value of β will vary from a maximum to zero as the two dimensional height of the propeller decreases from the diameter at the centre to zero at the tip.

1.2.3.2 Three-dimensional extension

The approach of extending the model to three dimensions [8] relies on the assumption that the propeller slipstream is directed purely in the axial direction and can be abstracted to a single average value as is discussed above in relation the past equation. This assumption has been made extensively in the literature with roots in simple momentum theory. Although the results from the assumptions of a “jet" blowing a wing have often predicted greater lift increases than observed in experiments, the assumption provides a reasonable starting point from which more detailed analyses can be performed.

Additionally, one of the poor assumptions inherent in many of the previous studies will be addressed to greatly increase the accuracy of this method. Consequently, this approach is adopted for the conceptual design analyses of interest in this dissertation.

A simple extension of the methods above to three dimensions can be performed as follows when adopting the approach described above. The fractional increase in the wing lift due to that of a single propeller can be estimated with the following equation.

$$\frac{\Delta C_L}{C_{L\infty}} = \left(\frac{\Delta C_l}{C_{l\infty}}\right)\left(\frac{b_{blown}}{b}\right) \tag{23}$$

The term $\Delta C_l/C_{l\infty}$ can be determined from the equation above that is appropriate for the geometry under consideration, b is the wingspan, and b_{blown} is the span of the wing immersed in the slipstream of the single propeller. This equation makes several assumptions in addition to those made above to determine $\Delta C_l/C_{l\infty}$:

1. Swirl is either negligible or the effects of swirl on one side of the propeller disk effectively cancel out the effects of swirl on the opposite side of the disk.
2. The slipstream velocity is assumed to be constant behind the propeller. Because of this assumption, this model can very easily be paired with basic momentum theory, which assumes a uniform velocity increase aft of a propeller disk. In reality, the velocity in the propeller slipstream will vary with radial station. If a radial variation of the velocity is known, either a single average velocity should be input into the above equation or an integration of the two dimensional solutions for $\Delta C_l/C_{l\infty}$ developed above should be performed.
3. No section of the wing behind the propeller is at or near stall (all local wing sections are at angles of attack in the linear region of the lift curve).
4. The propellers should not extend all the way to the wing tips. The flow at the airfoil sections near the tip cannot be approximated well by a two-dimensional airfoil and this method is incapable of capturing any interaction between the propeller vortex structure and wing tip vortex.

The previous equation can be generalized to account for wings with *N* propellers and/or sections of wing twist (DEP). In this equation, the percentage lift increase of the wing section i and the percentage of the span in the propeller slipstream of section i are combined with all other sections to give the net effect on the entire wing.

$$\frac{\Delta C_L}{C_{L\infty}} = \sum_{i=1}^{N}\left(\frac{\Delta C_l}{C_{l\infty}}\right)_i\left(\frac{b_{blown}}{b}\right)_i \tag{24}$$

One question that arises is how the blown wingspan should be calculated. Generally, the slipstream from the propeller will contract as it moves aft, so the span of the blown portion aft of the propeller will be reduced from the diameter of the propeller. The further ahead of the wing the propeller is located the larger the slipstream contraction. One estimate of the slipstream contraction can be made from

momentum theory principles and is shown in the following equation, where D_s is the contracted diameter, D is the propeller diameter, a is the axial induction factor, and x is the (dimensional) axial distance aft of the propeller.

$$b_{blown} = D_s = D\sqrt{\frac{1+a}{1+a\left(1+\frac{x}{\sqrt{x^2+\frac{D^2}{4}}}\right)}} \tag{25}$$

However, this equation should be used with caution, as the calculation of the slipstream contraction is not necessarily a simple task. If the propellers are lightly loaded, the slipstream contraction is only a few percent at most. For early-phase design studies and particularly for true “back of the envelope" calculations, the wing span immersed in the slipstream b_{blown} can be approximated assuming that there is no contraction of the propeller slipstream.

1.2.4 Reynard de Vries’ approach

The derivations presented in reference [6] are applicable to Hybrid-Electric Propulsion (HEP) aircraft with generic propulsion-system layouts. This section demonstrates how the method can be applied to tube-and-wing aircraft featuring leading-edge distributed-propulsion systems.
A series of “Delta” terms (ΔC_L, ΔC_{D0}, ΔC_{Di}) must be estimated in order to incorporate the aero-propulsive interaction effects in the design process. A preliminary method for wing leading-edge mounted, distributed tractor-propellers is proposed in this section. It is worth highlighting that the design procedure is also applicable to other novel propulsion-system layouts if the corresponding “Delta” models are determined.

1.2.4.1 Geometrical description of the DP system

Before evaluating the Delta terms, a simplified geometrical description of the system is required. This simplified representation assumes that the wing has a rectangular planform of span b and chord c, and that the propulsors are not located near the wing root or tip. The Distributed Propulsion (DP) system is considered to be an array of N propulsors of diameter D ($N/2$ propulsors per semi-wing, where N is equal to N_1 or N_2 depending on whether the system corresponds to the primary or secondary powertrain, respectively), aligned in spanwise direction with a separation parameter Δy. The propulsors are positioned at an angle α relative to the freestream velocity vector. A description is given in Figure 1.7.

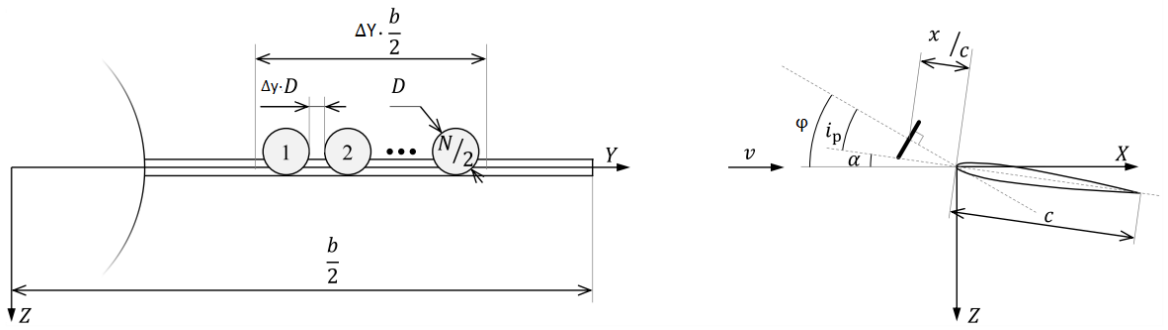

Figure 1.7: Simplified DP system representation, indicating the main geometrical parameters [6].

For a given number of propulsors and fraction of wingspan occupied by the DP array ΔY, the diameter of the propulsors can be computed with the following equation.

$$D = \frac{\Delta Y}{N(1+\Delta y)} b \tag{26}$$

N and ΔY are selected as design variables, while the diameter of the propulsors is left as dependent variable. This approach is preferred since the span interval along which propulsors are installed can be limited by structural or geometrical constraints.
The thrust required from a single propulsor can be expressed as a non-dimensional thrust coefficient.

$$T_c = \frac{1}{N} \frac{T_{DP}}{\rho v^2 D^2} \tag{27}$$

Where v and ρ are the velocity and density of the freestream respectively. Although in this configuration the freestream velocity v perceived by the propulsors is approximately equal in magnitude to the flight speed V, different symbols are used to distinguish between the inflow velocity relative to the propulsors, and the velocity of the aircraft in an inertial reference frame.

1.2.4.2 Aerodynamic model

The method proposed in this section is based on the approach of Patterson and German [8]. Modelling the impact of tractor propellers on wing performance boils down to estimating the “Delta” terms. Several assumptions are required in order to obtain a reasonable estimation with the information available in the preliminary sizing phase. Firstly, the propeller is modelled as an actuator disk in uniform axial inflow, and thus the upstream effect of the wing on the propeller is neglected. Secondly, the effect of each propeller on the adjacent ones is neglected. Thirdly, the wing is assumed to have a symmetric airfoil. Furthermore, the flow is attached, and the wing is fully immersed in the slipstream such that half of the slipstream flows under the wing and half over the wing. Finally, the effect of the propellers on the wing is limited to the spanwise interval occupied by the disks ΔY, and the effect on the

wing is uniform in spanwise direction. Due to these strong simplifications, the accuracy of this approach requires further investigation, especially in high-lift conditions.

Nonetheless, its simplicity and sensitivity to top-level design parameters make it suitable for the preliminary sizing phase and useful to demonstrate the applicability of the proposed sizing method. The first step is to compute the axial induction factor at the propeller disk a_P as a function of the propeller thrust coefficient, given by the following equation relative to the actuator disk theory.

$$a_P = \frac{V_P - V}{V} = \frac{1}{2}\left(\sqrt{1 + \frac{8\,T_c}{\pi}} - 1\right) \tag{28}$$

Where V_P - V is the velocity increase at the propeller disk. Due to contraction, the slipstream velocity impinging on the wing is higher than at the propeller disk. In order to evaluate the velocity induced by the propellers at the wing leading edge, it is necessary to express the axial position of the propeller as a fraction of its radius.

$$\frac{x}{R} = \frac{(x/c)}{(R/c)} \tag{29}$$

It is now possible to compute the contraction ratio of the slipstream at the wing leading edge with the following equation derived from momentum theory principles.

$$\frac{R_w}{R} = \sqrt{\frac{1 + a_P}{1 + a_P\left(1 + \frac{\frac{x}{R}}{\sqrt{\left(\frac{x}{R}\right)^2 + 1}}\right)}} \tag{30}$$

From conservation of mass in incompressible flow the axial induction factor at wing leading edge can be derived.

$$a_w = \frac{a_P + 1}{\left(\frac{R_w}{R}\right)^2} - 1 \tag{31}$$

This makes it possible to know the velocity increase due to the thrust generated by the propellers at the wing leading edge is known. Following the derivation of Patterson and German [7, 8] and modifying their equation considering a flat plate $C_{l\infty} = 2\pi \sin(\alpha)$, one can compute the sectional lift coefficient increase.

$$\Delta C_l = 2\pi\left[(\sin\alpha - a_w\beta\sin i_p)\sqrt{(a_w\beta)^2 + 2a_w\beta\cos(\alpha + i_p) + 1} - \sin\alpha\right] \tag{32}$$

Where α is the geometric angle of attack of the wing and β is a finite slipstream correction factor. Since in the sizing process the angle of attack of the wing is unknown, it has to be estimated using the three dimensional lift coefficient. For this, the expression presented by Roskam [15] can be used to determine the geometric angle of attack.

$$\alpha = \left(\frac{C_{L\,u}}{2\pi\, AR}\right)\left[2 + \sqrt{AR^2(1-M^2)\left(1 + \frac{\tan^2 \Lambda_{c/2}}{1-M^2}\right) + 4}\right] \tag{33}$$

In the above equation M is the freestream Mach number, the parameter $\Lambda_{c/2}$ is the wing half-chord sweep angle and the symbol $C_{L\,u}$ is the lift coefficient of the isolated wing. Since the aero-propulsive model assumes a rectangular wing, in this case the sweep angle is $\Lambda_{c/2} = 0$. The lift coefficient increase in three dimensions can be computed with geometrical consideration.

$$\Delta C_L = \Delta C_l \cdot \Delta Y \tag{34}$$

Determining the finite slipstream correction factor β is a critical step in the process. If this term is neglected, the lift increase can be significantly over-estimated, especially for small ratios between the slipstream radius and wing chord, as is the case for DEP. To this end, Patterson [8] generated a surrogate model based on CFD simulations of an actuator disk in front of a two dimensional wing with a modified NACA 0012 airfoil. The surrogate model is used in this study to compute β as a function of a_P, x/c and R/c.

In order to evaluate the impact of the propeller on wing drag, several contributions have to be analysed. Firstly, the increase in zero-lift drag is related to the increase in friction drag on the wing surface due to increased dynamic pressure in the slipstream. This contribution can be calculated using the following equation.

$$\Delta C_{D0} = a_w^2 c_f \cdot \Delta Y \tag{35}$$

Where c_f is the sectional skin friction coefficient, for which a typical value of 0.009 can be used. Since at this stage of the design process not enough information is available to obtain a meaningful estimation of the change in wetted area when replacing one large nacelle by multiple smaller ones, this contribution to ΔC_{D0} is neglected.

The increase in lift-induced drag can be attributed to an increase in C_L on one hand, and to a change in the Oswald factor on the other. The former can be estimated by assuming a parabolic polar.

$$\Delta C_{Di} = \frac{\Delta C_L^2 + 2C_{L\,u}\,\Delta C_L}{\pi\, AR\; e} \tag{36}$$

The change in Oswald factor due to aero-propulsive interaction, meanwhile, is assumed to be limited to a change in the span efficiency of the wing. However, the variation in span efficiency depends on a large

number of design parameters and operating conditions, and is therefore difficult to estimate analytically. At high thrust settings, the increased velocity and swirl in the propeller slipstream lead to pronounced peaks in the spanwise loading distribution, decreasing the span efficiency. At low thrust settings, on the other hand, the trends are less clear. The aero-propulsive model is evaluated with an Oswald factor with a value between 0.6 < e < 0.8 that leads to a nearly perfect agreement between the predicted drag coefficient values.

1.2.5 Marretta's hybrid numerical technique

Marretta's model [12] is based on a hybrid numerical technique, the Free Wake Analysis (FWA) and Boundary Element Method (BEM), applied to the wakes of a propeller and a wing, respectively. The research focused on the wing pressure coefficient distribution related to the altered upstream conditions of the coupled propeller, hence the wing loads and the pitching moment are computed. The results confirm the advantages of the present approach using the FWA and BEM to identify the aerodynamic features of the mutual interference of a wing and a propeller at angle of attack and at a fixed propeller operating condition.
The investigation considered here is purely computational and it is assumed that the flow is ideal and inviscid and the flowfield is inviscid and quasi steady behind the propeller. The algorithm based on the hybrid FWA-BEM approach is applied to find the mutual influence of the wing and propeller and its effects on aircraft performance.

1.2.5.1 FWA propeller model

In order to discuss the mutual three-dimensional wing-propeller influence, the wake from the propeller blades is considered and the FWA approach is first applied to an isolated propeller. This iterative method is based on a convergence criterion imposed on the sheet of vortices leaving each blade to form the propeller wake, which is made up of all the vortex lines starting from the points on the blade. The tip vortex line radial contraction r_t, and axial convection x_t, are related to the wake azimuth ψ and are valid in the region near the propeller disk, the so called near wake. Beyond a value ψ_s (far-wake), the flow becomes unstable. Anyway, the convection dominance of propeller flows like that of interest here makes this essentially irrelevant. For the propeller wake, the convergence criterion stops the description of the helicoidal vortex sheets at a certain downstream distance (assigned through a particular value ψ_s for which a dependence on the advance ratio J and the number of blades B is also provided based on experiment). Farther downstream, the wake is considered an infinite solenoid having constant diameter. The following equation relates the value of ψ_s to J, p, and the number of blades B.

$$(\psi_s - \psi_B)B\psi_B = 0.25\left[8.5 - \frac{p}{10} - J(J+2)\right] \tag{37}$$

ψ_B is the angle between each blade, J is the advance ratio, and β is the blade angle at 0.7 of the blade radius, R. For the tip vortex paths there are the following equations.

$$\begin{cases} \frac{r_t}{R} = A + (1-a)e^{-\frac{\psi}{B}} & for\ 0 \le \psi \le \psi_s \\ \frac{x_t}{R} = K_1\left(\frac{\psi}{\psi_B}\right) & for\ 0 \le \psi \le \psi_B \\ \frac{x_t}{R} = K_1 + K_2\left(\frac{\psi}{\psi_B} - 1\right) & for\ \psi_B \le \psi \le \psi_s \end{cases} \tag{38}$$

Assuming the parameter a as an experimentally determined constant, and A, K_1 and K_2 as related to β and J. by similarity, the relationship between the inner vortex line radial contraction r_v, and the vortex contraction is expressed in the following equation.

$$\begin{cases} \frac{r_v}{R} = \xi r_t \psi & for\ 0 \le \psi \le \psi_s \\ \frac{x_v}{R} = H(r,0)\psi & for\ 0 \le \psi \le \psi_B \\ \frac{x_v}{R} = H(r,0)\psi_B + H(r,\psi_B)(\psi - \psi_B) & for\ \psi_B \le \psi \le \psi_s \end{cases} \tag{39}$$

Where the functions $H(r, o)$ and $H(r, \psi)$ depend on the coordinates of the vortex filament (ψ, ψ_B). The velocities u, v, w induced by the wing and its wake at any point on the blade, P, may be calculated by relating the wing lift coefficient, C_l, to the wing and wake vortex strengths. H may be found as a function of the induced velocity components u, v, and w, and ψ.

$$H(u,v,w,\psi,r) = \left(\frac{\pi}{180}\right)(V_\infty + u)\xi/[\Omega r + v\cos\psi - w\sin\psi] \tag{40}$$

It should be noted that the induced velocity, w, is given, as will be seen later, by half the Hilbert term. Through Biot-Savart's law, applied to the blade circulation $\Gamma(\xi)$ and to the trailing wake vortices, one obtains the induced velocity at any point in the wake as follows.

$$V_P = \frac{1}{4\pi}\int_{R_0}^{R} \Gamma(\xi)\frac{dl \times r}{r^3} + \frac{1}{4\pi}\int_{\xi_0}^{1}\left[\frac{-d\Gamma(\xi)}{d\xi}\int \frac{dl \times r}{r^3}\right]d\xi \tag{41}$$

In the above equation $\boldsymbol{r}$ represents the position vector of a space point P in the vortex coordinates system, $\Gamma(\xi)$ is the vortex filament leaving the point ξ of the blade, and $\boldsymbol{dl}$ is the vector parallel to the direction of the bound vortex in the first integral, and to the trailing vortex filaments in the second one. By noting that the bound vortices hardly ever influence the near wake region, we suppose this influence may well not be large and $\boldsymbol{dl} \times \boldsymbol{r}$ vanishing. Having evaluated the circulation Γ, the velocity induced at the point P by the sheet vortices may be written as a superposition, on each blade, of each integral:

$$V_{ia}(P) = \frac{1}{4\pi}\sum_{p=1}^{B}\int_{\xi_0}^{1}\left[\Gamma(\xi)\int\frac{\tau_p \times r_p}{{r_p}^3}\right]d\xi \tag{42}$$

Where $\boldsymbol{\tau_P}$ is the unit vector parallel to the direction of the sheet vortex filament. Therefore, the velocity V_P, induced by the free vortices at point P, may be written in the following form.

$$V_{il}(P) = \frac{1}{4\pi}\int_{R_0}^{R}\frac{d\Gamma(\xi)}{d\xi}G(P,\xi)d\xi \tag{43}$$

The influence coefficients G(P, ξ) is expressed in the following equation.

$$G(P,\xi) = -\int\sum_{p=1}^{B}\frac{\tau_p \times r_p}{{r_p}^3}dl \tag{44}$$

As regards the far-wake regions, the influence of an elementary ring vortex C on the induced velocity is given by the following integral expression.

$$\int\frac{dl \times r}{r^3} \tag{45}$$

Which is solved numerically; the intensity assigned to the vortices of the far-wake is that of the last vortices of the near-wake.

1.2.5.2 Wing-propeller model and coupling

The performance is calculated for a propeller with a given number of blades with specified dimensional and design characteristics as the geometric twist, β, the diameters, R and R_0, the free stream velocity, V_∞ and the rotational speed, Ω. The present work takes into account the strength of the three-dimensional induction of the wing and its interaction with the propeller in terms of the variations of wing circulation, lift and induced drag coefficients and, finally, the wing quasi steady distributions of the chordwise pressure coefficients. The location of the centre of lift along the wingspan is also calculated to provide the pitching moment characteristics of the aircraft. The convergence criterion for the wing loads is that the difference in loads is negligible if they are less than 1.5%, as related to the altered propeller upstream conditions. Based on the available literature concerning numerical results and experimental data, the aerodynamic characteristics of the blade airfoil section can be introduced into the numerical process. For the tractor configuration, in order to avoid the approximation of the classical Prandtl horseshoe vertical model for the wing, the theory due to Pistolesi-Weissinger, in which the bound vortex is placed on the wing quarter-chord line and the tangency condition to the surface is enforced at the three-quarter chord line, is used here. By assuming a rectangular wing geometry as input, with the hypotheses of quasi steady and inviscid flow and negligible effects of vortex rollup, and

regarding the wing and its wake to be coplanar, an integral-differential equation containing the circulation, with its relative boundary conditions $\Gamma = 0$ at wing tips, is obtained.

The system of wing wake vortices is assumed to be adequately represented by a set of free vortices lying in the wing plane, parallel to the freestream and trailing downstream from the three-quarter chord line. This set of vortices may be seen as free when their geometry is considered as determined by using the self-induced wake velocity. The bound vortex circulation $\Gamma_w(s)$ varies along the non-dimensional wingspan s and is of such a magnitude that its own induced velocity added to that given by the trailing vortices results in the flow velocity being tangent to the wing three-quarter chord line. This method was previously applied to a complex but isolated plane wing geometry and it is here described for an unswept rectangular wing immersed in a propeller flow field. By integrating along the lifting line and by collecting the two above-mentioned contributions, one obtains the induced velocity. By imposing the Pistolesi-Weissinger condition between induced velocity and angle of attack, and by normalizing the induced velocity and geometry parameters with V_∞ and the wingspan y_b, respectively, the following integro-differential equation is obtained:

$$2\alpha_0(s) = \frac{1}{\pi}\int_{-1}^{1} \frac{d\Gamma_w}{dt}\frac{dt}{s-t} + \frac{1}{\pi}\int_{-1}^{1} T(s,t)\Gamma_{w(t)}dt \;\; for -1 \le s \le 1 \tag{46}$$

Where $T(s, t)$ is given by the following equation.

$$T(s,t) = \frac{2}{\sqrt{c^2 + 4(s-t)^2}\left[1 + \sqrt{c^2 + 4(s-t)^2}\right]} \tag{47}$$

Where c is the non-dimensional (constant) wing chord, and the parameter s is the spanwise coordinate along the lifting line. The tip boundary condition for the circulation is $\Gamma(-1) = \Gamma(1) = 0$. Suitable mathematical procedures applied to the past equation lead to a numerical solution for the circulation, which can be expressed with the following equation.

$$\Gamma_{w(t)} = (1-t^2)^{1/2}\sum_{j=1}^{N} \omega_j \frac{U_N(t)}{(t-t_j)U'_N(t)} \tag{48}$$

Where ω_j are a set of unknown coefficients and $U_N(t)$ (N =1, 2 ...) are the Chebyshev polynomials of the second kind, and t_j their zeroes. Through the following relationships one obtains the collocation points s_k and t_j.

$$\begin{cases} s_k = \cos\left(k\dfrac{\pi}{n+1}\right) \\ t_j = \cos\left(j\dfrac{\pi}{n+1}\right) \end{cases} \tag{49}$$

Meanwhile, the wing induced drag coefficient is computed in the following form.

$$C_{Di} = \frac{1}{c_0}\int_{-1}^{1}(w_{i0} + \Delta w_i + w_p)(\Gamma_{w0} + \Delta\Gamma_w)\, ds \tag{50}$$

The parameter w_{io} is the induction from the isolated wing wake (related to Γ_{wo}), Δ_{wi} is the additional induction resulting from the modification of the wing wake induced by the propeller wake (related to $\Delta\Gamma_w$). The parameter w_p is the downwash component at the wing induced by the propeller may be numerically processed thanks to the linearity of the quarter of the opposite of the Hilbert term.

$$w_{i0} = -\frac{1}{4}\sum_{j=1}^{N} a_{kj}\xi_j \tag{51}$$

Starting from the past equation, the induced drag coefficient can be decomposed as in the following equations.

$$\begin{cases} C_{Di} = C_{Di0} + (\Delta C_{Di})_p + (\Delta C_{Di})_w + (\Delta C_{Di})_{pw} \\ C_{Di0} = \frac{1}{c}\int_{-1}^{1}(w_{i0})(\Gamma_{w0})\, ds \\ (\Delta C_{Di})_p = -\frac{1}{c}\int_{-1}^{1}(w_p)(\Gamma_{w0} + \Delta\Gamma_w)\, ds \\ (\Delta C_{Di})_w = -\frac{1}{c}\int_{-1}^{1}(w_{i0} + \Delta w_i)(\Gamma_{w0} + \Delta\Gamma_w)\, ds + \frac{1}{c}\int_{-1}^{1}(w_{i0})(\Gamma_{w0})ds \\ (\Delta C_{Di})_{pw} = -\frac{1}{c}\int_{-1}^{1} w_p \Delta\Gamma_w\, ds \end{cases} \tag{52}$$

1.3 Model Comparison

In order to test the accuracy of the models described above, the lift augmentation predicted by the methods are compared to several experiments and other higher-order computational modelling tools in this section. Marretta's hybrid numerical technique is discarded in this phase because the hybrid FWA-BEM approach is considered too complex for early-phase design studies and it is not indicated for the DEP system. Since Reynard de Vries' approach follows the derivation of Patterson's approach about the lift coefficient, this model is neglected in this section because it gives the same results of Patterson's approach. Patterson's approach is compared to the theories presented by Jameson and Smelt and Davies [8].

1.3.1 LEAPTech wing Test

The LEAPTech wing test rig is closest to the configurations of interest for this master thesis since it uses many, smaller diameter high-lift props. Experimental data are unavailable in Patterson's dissertation

[8], but comparisons will be established with the results obtained from two separate CFD programs that are Fully Unstructured Navier-Stokes (FUN3D) and Simulation of Turbulent flow in Arbitrary Regions - Computational Continuum Mechanics (STAR-CCM+). The FUN3D results were performed at NASA Langley Research Center, while the STAR-CCM+ results were obtained from Joby Aviation.

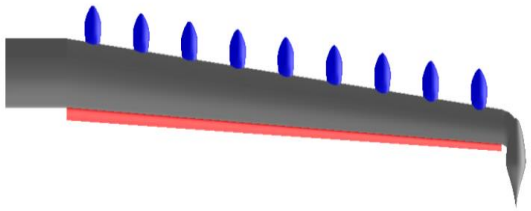

Figure 1.8: Top view of a semi span of the LEAPTech wing [8].

In Figure 1.8, the high-lift propeller nacelles are shown in blue; the flap in its extended position is shown in red; and the main wing is gray. The LEAPTech wing has an area of approximately 55 ft², a span of 31 ft, and a mean chord length of approximately 1.72 ft. The wing is provided with full-span fowler flaps, whose airfoil sections have a zero-lift angle of attack of approximately -24°. The wing is twisted with the root set at a positive 5° incidence angle relative to the body centerline axis and the tip at a positive incidence (the wing has 4° of washout). The wing is unswept and untapered from the centerline out to 1.85 ft where the chord length is 2.29 ft. Then there is a 10° leading edge sweep and the chord decrees to 1.15 ft at a spanwise location of 15.1 ft. The propellers are 1.465 ft in diameter and produce approximately 41 lb of thrust each. Each of the eighteen props is placed 0.65 ft ahead of the wing leading edge at its centerline. The inner-most nacelle is placed 2.65 ft from the wing centerline and the outer-most nacelle is placed at a spanwise location of 14.37 ft. All nacelles are evenly spaced along the span and are placed at a zero degree incidence relative to the vehicle longitudinal axis. The average change in axial velocity produced by the propellers is calculated here with momentum theory.

For comparison purposes, only low angles of attack are considered here. Since the models presented in this chapter are incapable of predicting behaviour after stall, low angle of attack data where the lift curve is approximately linear provides the best test of the model. Generally, the presence of high-lift propellers will delay stall to higher angles of attack, which will increase the lift more than predicted by the above models. Therefore, if the model is sufficiently accurate in the linear regime of the lift curve, it becomes a conservative estimate of the true lift multipliers that high-lift propeller systems can practically provide.

Additionally, the comparisons here are made based on the lift multiplier K_L obtained from the unblown condition to the blown condition. The lift multiplier is defined as the ratio of the lift generated by a flat plate in slipstream, $C_{l,}$ and the lift produced by flat plate in the absence of the slipstream, $C_{l\infty}$.

$$K_L = \frac{C_l}{C_{l\infty}} \tag{53}$$

This approach eliminates any differences in the unblown C_L predictions that may occur between the baseline lift predictions, which here are taken as the FUN3D and STAR-CCM+ CFD results. Furthermore, the K_L for each of the three theories is unchanged regardless of the original unblown C_L estimate.

Before comparisons to the theories presented by Jameson and Smelt and Davies can be made it should be noted that there are two manners in which their models can be applied to aircraft with multiple, adjacent propellers. Both of these theories requires that the aspect ratio of the wing in the slipstream be specified. This aspect ratio may be calculated for each individual propeller, which is termed here the "individual" calculation, or by assuming that all the propellers combine to provide a wide slipstream, which is termed a "grouped" calculation. Both theories seem to imply that the grouped method is the appropriate selection, but it is somewhat unclear. Therefore, both methods are employed here in comparison to the LEAPTech wing to evaluate which method is most appropriate.

Additionally, there are multiple ways of employing the Patterson's model. Each propeller can be considered individually as described above taking the mean chord length behind the propeller for calculation of β parameter; this is termed a "detailed" approach. Alternatively, since each propeller has the same design, calculations for a single propeller located at a fictitious wing station with an average wing twist (2.5°) and an average chord length (1.72 ft) can be performed and the results applied over all 18 propellers. This alternate approach is termed "simple". Both these approaches are shown below. A comparison of the lift multiplier values predicted by the three theories and two CFD programs is shown in Figure 1.9.

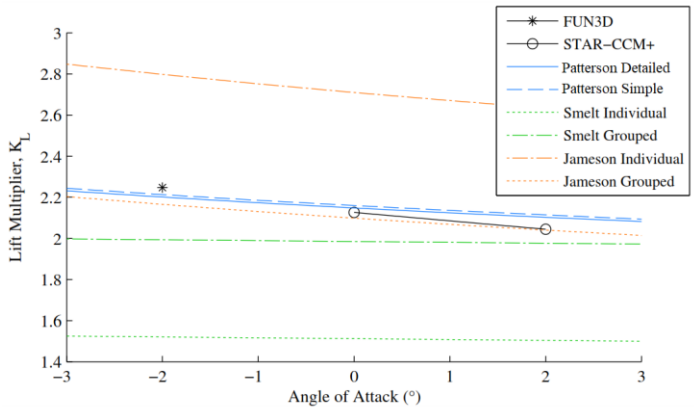

Figure 1.9: Comparison of the theories to CFD predictions for the LEAPTech configuration [8].

This factor shows only the lift carried by the wing and ignores any contribution of the propeller thrust to effective lift. Patterson's model results are shown in the blue solid and dashed lines located near the middle of the figure. The Smelt and Davies' model results are shown with the green lines. The dot-dashed line near the centre of the figure shows the results of the grouped implementation, and the dotted green line at the bottom of the figure represents the individual implementation. Predictions of the lift multiplier from Jameson's model are shown in orange with the dotted line at the centre of the figure representing the grouped calculation and the dot-dashed line at the top of the figure showing the results of the individual calculation. It should be noted that only a single point from FUN3D is shown

because the unblown airfoil is clearly stalled at angles of attack greater than -2° and no data points exist for lower angles of attack. It is unclear if the airfoil is stalled at -2°; if it is, then the K_L shown in the figure is higher than would be expected. Similarly, there are only two data points shown for the STAR-CCM+ results because no lower angles of attack are run and stall is predicted on the unblown wing at higher angles of attack. The results indicate that the grouped implementation of both the Jameson and Smelt and Davies models is most appropriate. The individual implementation of the Jameson model greatly over-predicts the lift multiplier while the individual implementation of the Smelt and Davies model greatly under-predicts the K_L. These same trends have been observed in other cases; consequently, in the following discussion and all other comparison cases presented in this chapter, only the grouped implementations will be discussed any further. The results from the simple and detailed variants of the theory presented in this chapter are virtually identical. This implies that for early-phase design studies the impacts of differing propeller installation angles and wing taper can effectively be ignored so long as there are not large changes between these values along the wingspan and a single high-lift propeller design and airfoil are used. (If a portion of the high-lift prop system is blowing a flapped portion of the wing while other props blown unflapped wing sections, then utilizing the simple variant of the new method is not likely to be as accurate). Both the Patterson' approach and Jameson's approach show decreases in K_L with increasing angle of attack while the Smelt and Davies' approach predicts results that are virtually constant with angle of attack. The STAR-CCM+ results indicate that there should be a slight decrease in K_L with increasing angle of attack, which implies that the Patterson's model and the Jameson's model are superior to the Smelt and Davies' model. Furthermore, the Smelt and Davies' model predicts lift multipliers noticeably lower than the CFD results indicate. The slope of Jameson's model appears to match the STAR-CCM+ results more closely than the Patterson' model. Both Jameson's model and Patterson's model presented in this chapter under-predict the FUN3D results. However, Jameson's model is both slightly low compared to the STAR-CCM+ results while the Patterson's model predicts slightly higher lift multipliers than STAR-CCM+.

Ultimately, the results indicate that either Jameson's theory or Patterson' theory presented in this chapter are superior to the theory of Smelt and Davies for this type of configuration. However, the results from this comparison are insufficient to state definitively whether Patterson's model presented here or Jameson's model is most appropriate. Both appear to give answers of sufficient accuracy for early-phase design.

1.3.2 Kunh and Draper Experiments

Kuhn and Draper's experiments [8] represent a good test case for the comparison. These experiments tested a wing with NACA 0015 airfoil sections with a propeller upstream. The tests are performed at various freestream velocities from zero up to 82 ft/sec (just under 25.2 m/s). These velocities are slightly slower than the primary use case for models described above, and models are incapable of providing results for the cases with zero freestream velocity. For the comparison, cases where the freestream velocity is 22.1, 17.5 and 13.4 m/s are considered here. The model of Patterson as well as the models of Jameson and Smelt and Davies are also compared to the data. The airfoil is symmetric in this test case

and the propeller is installed with its rotational axis in line with the chord. Kuhn and Draper remark that the lift increase agrees best with Smelt and Davies' theory when the assumption is made that the circulation around the wing is unchanged by the presence of the slipstream. This is precisely what Patterson's model predicts would occur for the propeller installation studied in these experiments. Comparisons of the lift increase observed in the experiments and that predicted by Patterson's theory, Jameson's theory, and the theory of Smelt and Davies are shown in Figure 1.10.

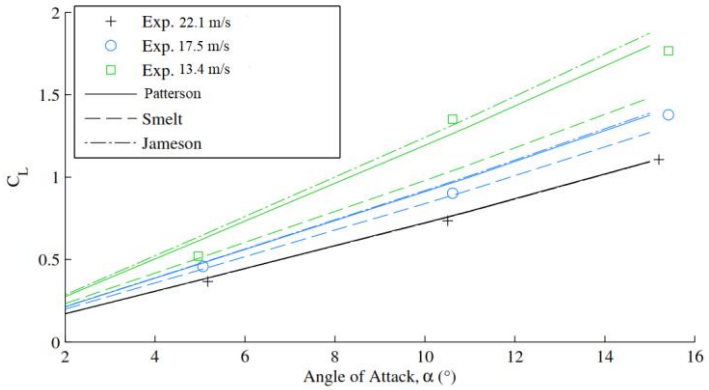

Figure 1.10: Comparison of the experimental data of Kuhn and Draper to Patterson's theory, Jameson's theory and Smelt and Davies' theory [8].

The experimental data is shown with the marker types indicated in the legend and the predictions of all three theories have the line types denoted in the legend. The lowest C_L values are observed for a freestream velocity of 22.1 m/s and are shown in black. The blue lines and markers correspond to the 17.5 m/s runs, and green is used to denote the 13.4 m/s cases. As can be seen in figure, Patterson's model predicts the lift increases reasonably well. All three models predict virtually identical lift increases for the lowest thrust/highest freestream velocity case. Although the Smelt and Davies' model predicts the moderate thrust case more accurately than the other two models, it vastly under-predicts the lift increase for higher angles of attack at the highest thrust level. Patterson's model slightly over-predicts the lift augmentation at the medium thrust case, but follows the data closely at the higher thrust setting. Jameson's model is generally close to the present theory's prediction, but begins to predict more lift at higher thrust settings.

It should be noted that the results presented above from Kuhn and Draper are obtained through digitizing the figures located in the paper and transforming the data provided to the lift coefficient. In addition to experimental error sources, there are likely small errors in the location of the experimental points for these reasons.

1.3.3 Gentry Experiments

To ascertain how well models predict increases in lift with varying propeller installation angles, experiments of Gentry [8] are compared to models predictions. In their experiments, Gentry studies a

turboprop placed 12 inches upstream and 5 inches below the chord line of a semispan wing of 20 inch chord and varies the inclination angle of the nacelle relative to the wing. The wing is equipped with full-span, double-slotted flaps that are deployed 60°. The highly loaded, 12 inch diameter propeller is operated at two different rotational speeds: 11,000 RPM and 14,000 RPM.

In order to estimate the slipstream velocity aft of the propeller that is required for comparison to the theories, the propeller thrust coefficient versus advance ratio curves are taken from an earlier paper by Gentry. Based on the stated dynamic pressure and freestream velocity in their later experiments, the thrust of the propeller at the two stated RPM conditions is determined. Finally, the average induced axial velocity is estimated from momentum theory taking into account the reduced disk area from the propeller hub. The results of the experiments and the predictions of the three theories are shown in the following figures, with the first figure corresponding to the 11,000 RPM propeller operating conditions and the second figure showing results from 14,000 RPM setting.

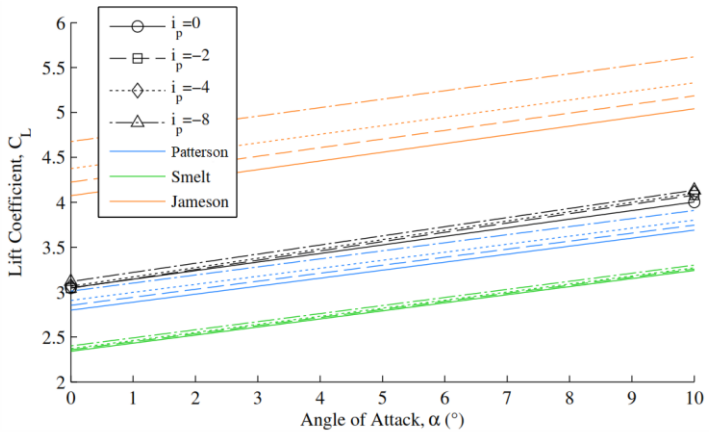

Figure 1.11: Comparison of the experimental data of Gentry with a propeller RPM of 11,000 to Patterson's theory, Jameson's theory and Smelt and Davies' theory [8].

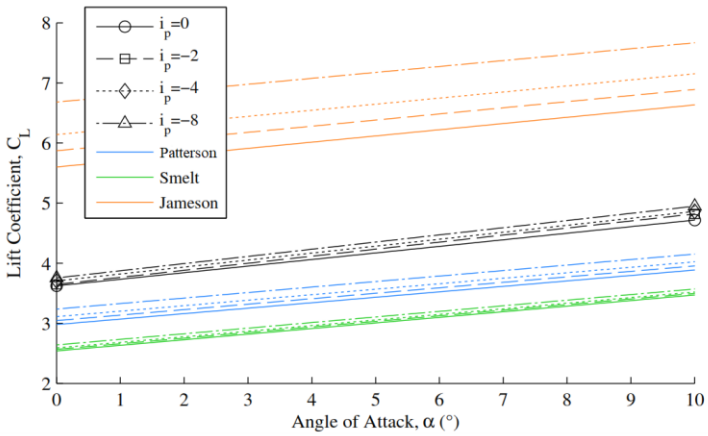

Figure 1.12: Comparison of the experimental data of Gentry with a propeller RPM of 14,000 to Patterson's theory, Jameson's theory and Smelt and Davies' theory [8].

These figures show the lift coefficient versus angle of attack for four separate nacelle inclination angles: 0°, -2°, -4° and -8°, where here i_p is measured relative to the wing chord line. Each line in the figures corresponds to one of these inclination angles with 0° being solid, -2° being dashed, -4° being dotted and -8° being dot-dashed. The experimental data is shown in black with markers denoting the actual data points. Only two angles of attack from the experiment are shown because the unblown wing experienced stall at higher angles of attack and only positive lift is of interest in the comparisons. The blue lines closest to the experimental data result from Patterson's model. The green lines near the bottom of the figure are the predictions of the Smelt and Davies' model and the orange lines at the top of the figure result from Jameson's model.

Here, the Jameson's model greatly over-predicts the lift augmentation, Smelt and Davies' model greatly under-predicts the lift, and Patterson's model slightly under-predicts the lift. Although none of the models performs exceptionally well, Patterson's model is most accurate as it is at most 8% different from the experiment in the 11,000 RPM case but 18% different in the 14,000 RPM case. Jameson's model is 56% different from experiment at worst for the 11,000 RPM runs and over 91% different for the 14,000 RPM case. Smelt and Davies' model is 23% low for the 11,000 RPM case and approximately 30% different at 14,000 RPM.

The large over-prediction by Jameson's model is similar to the over-prediction that is seen in LEAPTech's experiment when using the detailed implementation. Here, only a single propeller exists, so there is no difference between the simple and detailed implementations. This seems to indicate that Jameson's model is not appropriate if only single propellers are used. Such a conclusion is logical because the method is developed assuming the wing is fully immersed in a single, wide slipstream. Similarly, the model of Smelt and Davies is developed assuming lightly loaded propellers, so it is also not surprising that it does not provide satisfactory results for this case. It is assumed that one of the primary reasons Patterson's theory under-predicts the lift is due to the beneficial interaction of the propeller slipstream with the flap, which works to delay stall over the flap. This effect is not modelled. Additionally, the increase in lift in the experiments observed in going from a nacelle inclination angle of -4° to -8° is less than the lift increase predicted by Patterson's theory. One potential reason for this decreased lift lies in how externally blown flaps generate additional lift. In addition to delaying stall over the upper surface, these flaps seek to direct a large portion of the slipstream downward, which will generate a reaction lift force. With larger negative nacelle angles, the direction of the slipstream is initially directed upward at a greater angle than would typically occur. If this angle is too great (the local angle of attack on the flap is too high), the effectiveness of the flap in turning the flow can be reduced (the flap may experience beyond its stall angle of attack).

However, Patterson's model also may simply be too sensitive to changes in the propeller installation angle particularly for cases where the propeller centre is offset from the wing chord line. Since the OVERFLOW simulations from which the model for β is derived did not include a vertical propeller offset or offset of the slipstream direction from freestream, Patterson's model is being applied outside of its region of greatest accuracy. Consequently, caution should be exercised if Patterson's theory is applied to problems with propellers offset too far from the wing or at large nacelle incidence angles relative to the wing chord.

1.4 Summary of Reviewed Models

Jameson's, Smelt and Davies', and Patterson's simple models presented in this section were compared to multiple experimental results. The method of Smelt and Davies consistently under-predicts the lift augmentation from propeller blowing. Smelt and Davies's model is developed assuming lightly loaded propellers, so it is also not surprising that it greatly under-predicts the lift.

Jameson's model predicts the lift generated well in certain situations but deviates greatly in other experiments. Jameson's model is not appropriate if only single propellers are used, and the model is likely most accurate in the case of full-span blowing (the method is developed assuming the wing is fully immersed in a single, wide slipstream). Jameson's model will provide the most accurate results for configurations where larger portions of the wing are blown.

Patterson's model generally shows good agreement with experiments though it under-predicts the lift in cases with large flap deflections. Patterson's approach slightly under-predicts the lift due to the beneficial interaction of the propeller slipstream with the flap, which is not modelled. One potential reason for this decreased lift lies in how externally blown flaps generate additional lift. For these reasons, the best approach considered during problem description's phase is Patterson's model (which also implies Reynard de Vries' model).

Chapter 2 – Development and Validation of DEP Model

The purpose of this chapter is to illustrate the DEP model implemented and its improvements for the computation of aerodynamic coefficients. Successively, the validation phase is developed including the analysis of the new model through a comparison with experimental results and CFD results in different situations and for various types of aircraft. The DEP model is tested for the case of the NASA X-57 demonstrator [1] and for the LEAPTech wing [2]. The DEP model is also tested with Sinnige's experimental data [13], to check whether the model is accurate for other propeller configurations.

2.1 Description of DEP Model implemented

After the results illustrated in the comparison of the previous chapter, Patterson's model is considered more accurate than Jameson's model and Smelt and Davies' model. Since Reynard de Vries' model follows the derivation of Patterson's model for the lift coefficient and illustrates a possible computation of the drag coefficient inspired by Biber's investigation [6], we select this approach as reference model and we apply some modification to improve the final result:

1. The twist angle relative to the wing horizontal frame is made explicit and α_{twist} becomes an input for the model implemented.
2. The transition from second dimension to third dimension is executed with Patterson's theory (the geometrical spanwise separation of Reynard de Vries' model is neglected) and the number of propellers N and wingspan b are the only two additional input data for this passage of the model implemented.

The new model represents the propellers as actuator disks and the wing as a flat plate, incorporating Patterson's semi-empirical correction for finite slipstream height. The model includes several assumptions worth highlighting:

a. The velocity increase at the actuator disk is computed assuming uniform axial inflow.
b. Variations in lift due to swirl are neglected (actuator disk assumption).
c. The flow over the wing is attached.
d. The effect of each propeller on the adjacent ones is neglected.
e. The effect of the propeller on the wing is limited to the interval defined by the contracted diameter's slipstream of the single propeller.
f. Within this spanwise interval, the effect on the wing is considered uniform in spanwise direction.
g. The wing is supposed to be fully immersed in the slipstream, that is, half of the slipstream flows under the wing and half over the wing.
h. The stall behaviour of the wing is not taken into account.
i. Propellers are not located near the wing root or tip.

The simplicity and sensitivity of the model to top-level design parameters make it suitable for the conceptual sizing phase. It is now possible to show the input data and the output data of the model implemented with Tables 2.1 and 2.2.

Input data	Names	Units
T_C	Non-dimensional thrust coefficient of single propeller	—
D	Propeller diameter	m
x_C	Axial propeller position as function of chord	—
b	Wing span	m
c	Wing chord	m
AR	Wing aspect ratio	—
$C_{L\,u}$	Unblown wing lift coefficient	—
M	Mach number	—
$\Lambda_{c/2}$	Half-chord wing sweep angle	deg
φ	Geometric angle relative to wing vertical frame	deg
α_{twist}	Twist angle relative to wing horizontal frame	deg
N	Number of propellers	—

Table 2.1: Input data of the implemented DEP model.

Output data	Names	Units
ΔC_l	Sectional lift coefficient increase due to DP	—
ΔC_L	Lift coefficient increase due to DP	—
ΔC_D	Drag coefficient increase due to DP	—

Table 2.2: Output data of the implemented DEP model.

The first step is to compute the axial induction factor at the propeller disk a_P as a function of the propeller thrust coefficient, given by the following equation relative to the actuator disk theory.

$$a_P = \frac{V_P - V}{V} = \frac{1}{2}\left(\sqrt{1 + \frac{8\,T_c}{\pi}} - 1\right) \tag{54}$$

Where $V_P - V$ is the velocity increase at the propeller disk. Due to contraction, the slipstream velocity impinging on the wing is higher than at the propeller disk. In order to evaluate the velocity induced by the propellers at the wing leading edge, it is necessary to express the axial position of the propeller as a fraction of its radius, remember that the axial position of propeller as function of chord x_C is positive if the propeller is ahead of the leading edge.

$$\frac{x}{R} = \frac{x_C}{(R/c)} \tag{55}$$

It is now possible to compute the contraction ratio of the slipstream at the wing leading edge with the following equation derived from momentum theory principles.

$$\frac{R_w}{R} = \sqrt{\frac{1 + a_P}{1 + a_P\left(1 + \frac{\frac{x}{R}}{\sqrt{\left(\frac{x}{R}\right)^2 + 1}}\right)}} \tag{56}$$

From conservation of mass in incompressible flow the axial induction factor at wing leading edge can be derived.

$$a_w = \frac{a_P + 1}{\left(\frac{R_w}{R}\right)^2} - 1 \tag{57}$$

In order to compute the finite-slipstream correction factor β, a surrogate model is developed in Patterson's dissertation [8] as a function of three design parameters:

1. The ratio of the disk radius to the chord of the airfoil (R/c).
2. The velocity of the contracted slipstream far downstream of the disk.
3. The distance upstream of the leading edge the disk is placed.

For the model developed, the vertical height of the disk and the angle of the disk relative to the freestream are kept constant. To make data obtained from simulations useful in a computational design environment, the surrogate model is fit to the data. To fit the surrogate model, four separate fourth-order polynomials in the form of the following equation are fit to the data in order to obtain β. The resulting values of the coefficient row vectors are given in the next equations and these thirty numbers define the surrogate model.

$$\begin{cases} K_0 = [0.378269\ 0.748135\ -0.179986\ -0.056464\ -0.146746\ -0.015255] \\ K_1 = [3.071020 - 1.769885\ 0.436595\ 0.148643\ -0.9889332\ 0.197940] \\ K_2 = [-2.827730\ 2.054064\ -0.467410\ -0.277325\ 0.698981\ -0.008226] \\ K_3 = [0.997936\ -0.916118\ 0.199829\ 0.157810\ -0.143368\ -0.057385] \\ K_4 = [-0.127645\ 0.135543\ -0.028919\ -0.026546\ 0.010470\ 0.012221] \end{cases} \tag{58}$$

The final surrogate model to determine β can be represented in a single equation.

$$\begin{cases} \beta = K_0 X + K_1 X\left(\frac{R}{c}\right) + K_2 X\left(\frac{R}{c}\right)^2 + K_3 X\left(\frac{R}{c}\right)^3 + K_4 X\left(\frac{R}{c}\right)^4 \\ X = \left[1 \quad x_C \quad (x_C)^2 \quad (x_C)(2a_p + 1) \quad (2a_p + 1) \quad (2a_p + 1)^2\right]^T \end{cases} \tag{59}$$

From Patterson's theory it is imposed β equal to 1 as an effective upper limit.

Following the derivation of Patterson and German [7,8] and modifying their equation considering a flat plate $C_{l_u} = 2\pi\sin(\alpha)$, one can compute the sectional lift coefficient increase.

$$\Delta C_l = 2\pi\left[\left(\sin\alpha - a_w\beta\sin i_p\right)\sqrt{(a_w\beta)^2 + 2a_w\beta\cos\left(\alpha + i_p\right) + 1} - \sin\alpha\right] \tag{60}$$

Where α is the geometric angle of attack of the wing and β is a finite slipstream correction factor. Since in the sizing process the angle of attack of the wing is unknown, it has to be estimated using the three dimensional lift coefficient. For this, the expression presented by Roskam [15] can be used to determine the geometric angle of attack of the wing α.

$$\alpha = \left(\frac{C_{L\,u}}{2\pi AR}\right)\left[2 + \sqrt{AR^2(1-M^2)\left(1 + \frac{\tan^2\Lambda_{c/2}}{1-M^2}\right) + 4}\right] \tag{61}$$

In the above equation M is the freestream Mach number and $\Lambda_{c/2}$ the wing half-chord sweep angle.
The angle between the propeller axis and the wing chord i_p, can be computed with the following equation.

$$i_p = \varphi - \alpha - \alpha_{twist} \tag{62}$$

Following Patterson's extension to three dimensions, the percentage lift increase of the wing section and the percentage of the span in the propeller slipstream of section are combined with all other sections to give the net effect on the entire wing.

$$\Delta C_L = \sum_{i=1}^{N}(\Delta C_l)_i\left(\frac{b_{blown}}{b}\right)_i \tag{63}$$

The estimate of the slipstream contraction can be made from momentum theory principles and is shown in the following equation, where D_s is the contracted diameter, D is the propeller diameter, the parameter a_p is the axial induction factor, and the ratio x/R is the non-dimensional the axial position of the propeller as a fraction of its radius.

$$b_{blown} = D_s = D\sqrt{\frac{1+a_p}{1 + a_p\left(1 + \frac{\frac{x}{R}}{\sqrt{\left(\frac{x}{R}\right)^2 + 1}}\right)}} \tag{64}$$

In order to evaluate the impact of the propeller on wing drag, several contributions have to be analysed. Firstly, the increase in zero-lift drag is related to the increase in friction drag on the wing surface due to

increased dynamic pressure in the slipstream. This contribution can be calculated using the following equation.

$$\Delta C_{D0} = \sum_{i=1}^{N} a_w^2 c_f \cdot \left(\frac{b_{blown}}{b}\right)_i = N\, a_w^2 c_f \cdot \left(\frac{b_{blown}}{b}\right) \tag{65}$$

Where c_f is the sectional skin friction coefficient, for which a typical value of 0.009 can be used. Since at this stage of the design process not enough information is available to obtain a meaningful estimation of the increase in wetted area due to pylons and nacelles, their contribution to ΔC_{D0} is neglected. The increase in lift-induced drag can be attributed to an increase in C_L on one hand, and to a change in the Oswald factor on the other. The former can be estimated by assuming a parabolic polar.

$$\Delta C_{Di} = \frac{\Delta C_L^2 + 2C_{Lu}\,\Delta C_L}{\pi\, AR\, e} \tag{66}$$

The aero-propulsive model is evaluated with an Oswald factor e of 0.8 that leads to a nearly perfect agreement between the predicted drag coefficient values. The total increase in drag coefficient is given by the summation of the two terms that are the drag coefficient due to friction and dynamic pressure ΔC_{D0} and the drag coefficient induced by the lift force ΔC_{Di}.

$$\Delta C_D = \Delta C_{D0} + \Delta C_{Di} \tag{67}$$

From now on, we refer to this model implemented as the DEP model.

2.1.1 Experiment I – NASA X-57 Maxwell aircraft

In order to validate the DEP model, the case of NASA X-57 Maxwell electric aircraft for the first experiment is considered. The NASA X-57 Maxwell is an experimental aircraft being developed by NASA, intended to demonstrate technology to reduce fuel use, emissions, and noise. Modified from a Tecnam P2006T, the X-57 is an aircraft with 14 electric motors driving propellers mounted on the wing leading edges. All 14 electric motors are used during take-off and landing, with the only outer two used during cruise. The additional airflow over the wings created by the additional motors generates greater lift, allowing for a narrower wing. The aircraft seats two. It has a maximum range of 160 km and a maximum flight time of approximately one hour. Distributed propulsion increases the number and decreases the size of airplane engines. Electric motors are substantially smaller and lighter than jet engines of equivalent power. This allows them to be placed in different, more favourable locations. In this case, the engines are mounted above and they are distributed along the wings rather than suspended below them.
The propellers are mounted above the wing. They increase the air flow over the wing at lower speeds, increasing its lift. The increased lift allows it to operate on shorter runways. Such a wing could be only

a third of the width of the wing it replaces, saving weight and fuel costs. Typical light aircraft wings are relatively large to prevent the craft from stalling (which happens at low airspeeds, when the wing cannot provide sufficient lift).

In the first experiment [1], a computational study of the wing for the distributed electric propulsion X-57 Maxwell airplane configuration at take-off and landing conditions is completed. Two unstructured-mesh, Navier-Stokes computational fluid dynamics methods, FUN3D and Unstructured Software System (USM3D), are used to predict the wing performance. The traditional and effective lift coefficients for the blown and unblown high-lift wing at a freestream velocity of 29.837 m/s are computed with CFD methods. The unblown $C_{L\,u\,MAX}$ of the high-lift wing is 2.439. The blown high-lift wing, with the DEP system operating at 164.4 hp (13.7 hp/prop), achieves an effective $C_{L\,MAX}$ of 4.202 at $\alpha = 12°$. The traditional, maximum lift coefficient is 3.89 at $\alpha = 12°$, without the addition of the propeller vectors contributing to lift. At $\alpha = 10°$, the blown wing $C_{L\,blown}$ is 4.15 and the unblown wing $C_{L\,unblown}$ is 2.4, a lift augmentation of 1.7.

For the DEP model, it is possible to highlight the input data used in the first experiment with Table 2.3.

Input data	Numeric values	Units
T_C	0.611	—
D	0.57912	m
x_C	0.31	—
b	9.6	m
c	0.645	m
AR	15	—
$C_{L\,u}$	[1.7 – 2.5]	—
M	0.0878	—
$\Lambda_{c/2}$	1.9	deg
φ	0	deg
α_{twist}	0	deg
N	12	—

Table 2.3: Input data for 1st Experiment X-57 Maxwell aircraft with DEP model.

With these input data, it is possible to obtain the figure 2.1 that describes the behaviour of the aerodynamic coefficients with respect to a significant range of values for the angle of attack.

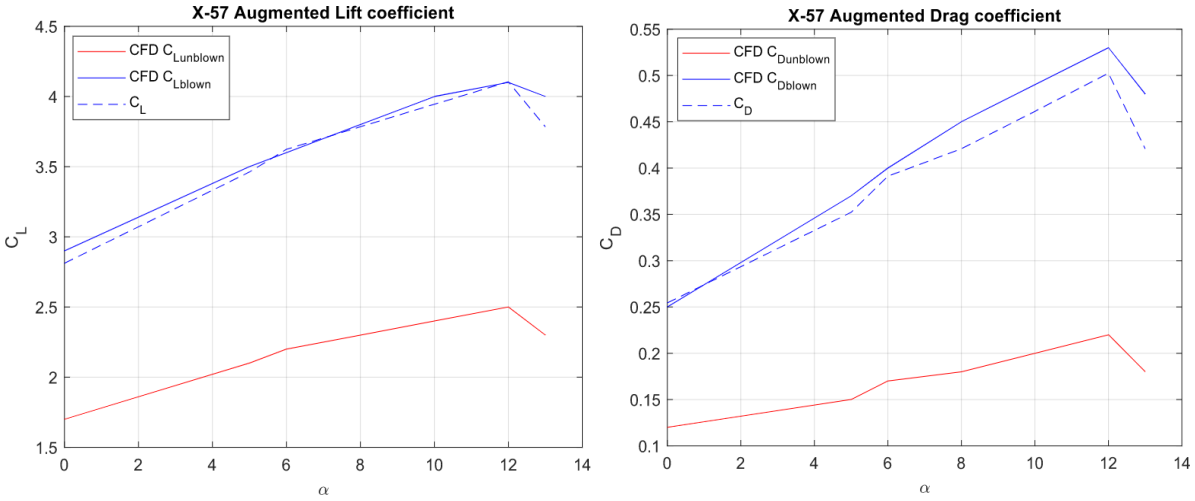

Figure 2.1: Aerodynamic coefficients respect to angle of attack for 1st Experiment X-57 Maxwell aircraft with DEP system.

In Figure 2.1, the left graph illustrates the increase in lift coefficient over the range of angle of attack from the unblown wing (red curve), to the blown wing (blue curve), computed with CFD methods. The blown wing computed with the DEP model (dashed blue curve) follows the real blown wing's path (blue curve) with excellent approximation. The right graph illustrates the drag coefficient over the range of angle of attack from the unblown wing (red curve), to the blown wing (blue curve), computed with CFD methods. The blown wing computed with the DEP model (dashed blue curve) slightly under-predict the real blown wing's path (blue curve).

2.1.2 Experiment II – LEAPTech wing

In order to validate the DEP model, it is considered the computational analysis of LEAPTech wing [2] for the second experiment. The Leading Edge Asynchronous Propeller Technology (LEAPTech) project is a NASA project developing an experimental electric aircraft technology involving many small electric motors driving individual small propellers distributed along the edge of each aircraft wing. To optimize performance, each motor can be operated independently at different speeds, decreasing reliance on fossil fuels, improving aircraft performance and ride quality, and reducing aircraft noise. The configuration used in this experiment is the LEAPTech high-lift wing with a 40° flap deflection and DEP system that is tested on the Hybrid-Electric Integrated Systems Testbed (HEIST) truck. The wing consisted of the National Aeronautics and Space Administration General Aviation Airfoil (NASA GAW-1) airfoil with a full span 30% chord flap and 18 propellers mounted on electric motors in nacelles upstream of the wing leading edge. The tip nacelles on the test article do not include the electric cruise motors that would be present to power the cruise propellers in a real airplane application. The LEAPTech wing has 4° twist and $\alpha = 0°$ is defined when the root section incidence is 5°. At the $\alpha = 0°$ inclination, all of the high-lift motor nacelles are at 0° incidence to the freestream flow.

In the second experiment [2], a computational study of a distributed electric propulsion LEAPTech wing is completed using FUN3D. Two lift-augmentation power conditions are compared with the power-off configuration on the high-lift wing (40° flap) at a 73 mph freestream flow and for a range of angles of attack from -5° to 14°. In this experiment the datum are M = 0.098, angles of attack from -5° to 14° and Re = 1,069,038 (1.07 million). The 73 mph speed at NASA Armstrong, corresponds to a 32.63 m/s equivalent airspeed (EAS) stall speed at sea level and is close to the maximum possible speed of the HEIST truck. A comparison of lift, drag and pitching moment coefficients between unblown, take-off power, and landing power for the high-lift wing with corotating propellers at 73 mph is computed with CFD methods. The maximum lift coefficient unblown is $C_{L\,\text{unblown}}$ = 2.318 at α = 1°. The maximum lift coefficients of $C_{L\,\text{MAX}}$ is 5.252 at take-off power (257.4 hp). The blowing lift augmentation does come with an increase in drag from C_D = 0.3209 to C_D = 1.0443 at α = 4°, for example.
For the DEP model, it is possible to highlight the input data used in the second experiment with Table 2.4.

Input data	Numeric values	Units
T_C	0.9	—
D	0.446	m
x_C	0.4	—
b	9.44	m
c	0.524	m
AR	17.4	—
$C_{L\,u}$	[1.9 – 2.35]	—
M	0.098	—
$\Lambda_{c/2}$	10	deg
φ	0	deg
α_{twist}	2.5	deg
N	18	—

Table 2.4: Input data for 2nd Experiment LEAPTech wing with DEP model.

With these input data, it is possible to obtain Figure 2.2, which describes the behaviour of the aerodynamic coefficients with respect to a significant range of values for the angle of attack.

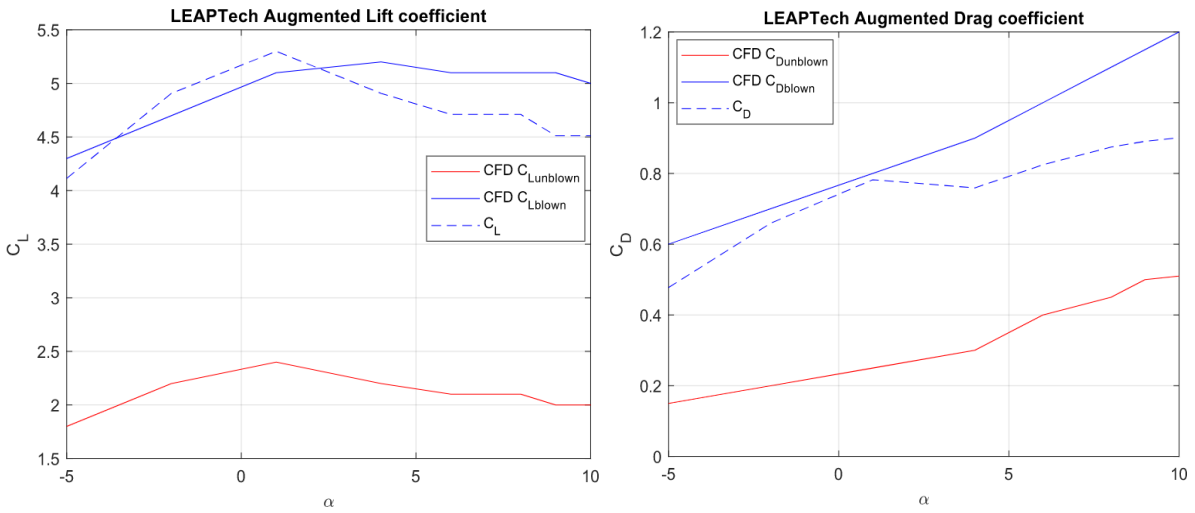

Figure 2.2: Aerodynamic coefficients respect to angle of attack for 2nd Experiment LEAPTech wing with DEP system.

In Figure 2.2, the left graph illustrates the increase in lift coefficient over the range of angle of attack from the unblown wing (red curve), to the blown wing (blue curve), computed with CFD methods. The blown wing computed with the DEP model (dashed blue curve) follows the real blown wing's path (blue curve) with discrete approximation. The right graph illustrates the drag coefficient over the range of angle of attack from the unblown wing (red curve), to the blown wing (blue curve), computed with CFD methods. The blown wing computed with the DEP model (dashed blue curve) slightly under-predict the real blown wing's path (blue curve) with discrete approximation.

2.1.3 Experiment III – NACA 64_2A015 airfoil in wind tunnel

In order to validate the DEP model, for the third experiment the Sinnige's aerodynamic analysis [13] in wind tunnel for NACA 64A015 airfoil implemented with the propeller mounted on the inboard part of the wing of the propeller–wing (conventional configuration) is considered. These experiments studied a single tractor propeller mounted on a low-aspect-ratio wing. The wing airfoil was cambered, and the performance is evaluated at low lift coefficients. The nacelle was connected to a straight, untapered wing with a chord length of 0.240 m, a symmetric NACA 64_2A015 profile, and an integrated 25% chord plain flap with a flap gap of 1 mm. This low aspect-ratio wing with a high ratio of propeller diameter to wingspan was chosen to obtain a relatively strong interaction between the propeller slipstream and the wing, which aided in the interpretation of the aerodynamic interaction mechanisms. The experiments were performed in the Low-Turbulence Tunnel at Delft University of Technology. This low-speed closed-return wind tunnel features a closed-wall test section with a cross section of 1.80 × 1.25 m.

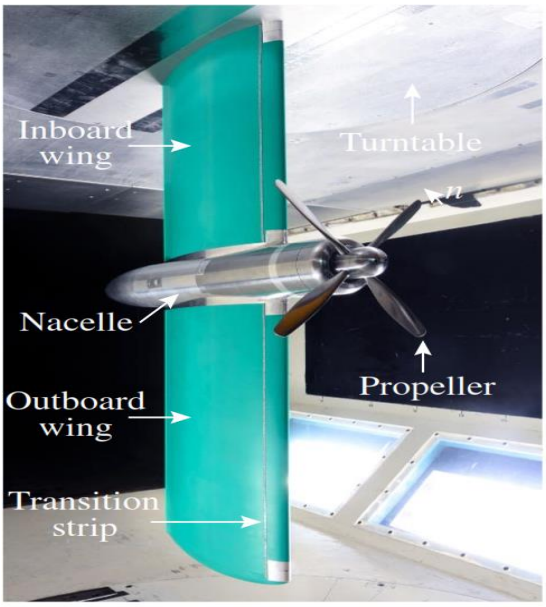

Figure 2.3: Conventional configuration for 3rd Experiment installed in wind tunnel [13].

The propeller has a diameter of 0.237 m and its four blades are set to a blade pitch angle of 23.9° at 75% of the radius (with the pitch angle defined relative to the local chord line). Compared to modern designs, the propeller has a low blade count, a low solidity, and no sweep. Still, its slipstream introduced all the relevant aerodynamic phenomena to the flowfield that affect the propeller–wing interaction.
The conventional configuration of the third experiment [13] has a rounded tip and a semispan of 0.748 m (AR=6.2), leading to a ratio of propeller diameter to wing semispan of 0.32, a typical value according to the twin-engine propeller-aircraft. As a result, the propeller axis is positioned at y/(b/2) = 0.444, which is somewhat more outboard than the typical value of y/(b/2) =0.30. This is considered acceptable for the present experiment, because the spanwise loading gradient on the inboard part of the wing is relatively small. Therefore, the sensitivity of the propeller–wing interaction effects to the spanwise location of the propeller is small as well on this part of the wing. The majority of the measurements discussed in this paper are taken at a freestream velocity of 40 m/s. This velocity provides the best compromise between the achievable Reynolds number and the operating range of the propeller, which is constrained by the output power of the electric motor. The propeller operates with thrust settings corresponding to advance ratios J of 0.7 and the associated thrust coefficients C_T is equal to 0.123.
For the DEP model, it is possible to highlight the input data used in the second experiment with Table 2.5.

Input data	Numeric values	Units
T_C	0.251	–
D	0.237	m
x_C	0.43	–
b	0.748	m
c	0.240	m
AR	6.2	–
$C_{L\,u}$	[0 – 0.95]	–
M	0.12	–
$\Lambda_{c/2}$	0	deg
φ	0	deg
α_{twist}	0	deg
N	1	–

Table 2.5: Input data for 3rd Experiment NACA 642A015 airfoil with DEP model.

With these input data, it is possible to obtain Figure 2.4, which describes the behaviour of the lift coefficient with respect to a range of angle of attack values.

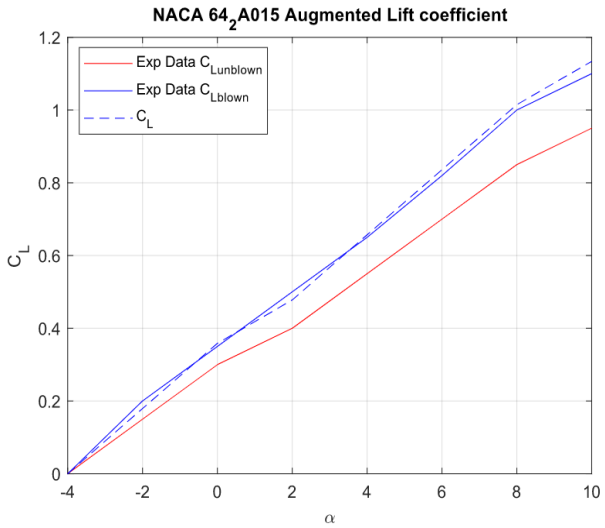

Figure 2.4: Aerodynamic coefficient respect to angle of attack for 3rd Experiment NACA 642A015 airfoil.

Figure 2.4 illustrates the increase in lift coefficient over the range of angle of attack from the unblown wing (red curve), to the blown wing (blue curve), computed with experimental analysis. The blown wing computed with the DEP model (dashed blue curve) follows the real blown wing's path (blue curve) with excellent approximation.

2.2 Validation Summary

After these three experiments, it is now possible to summarize the results and discuss the validation phase of the DEP model implemented. In the first two cases, the DEP model was compared to CFD results, while in the third case the DEP model was compared to experimental results.

In the first experiment [1], relative to the NASA X-57 Maxwell aircraft, the lift coefficient C_L was estimated with excellent approximation and the drag coefficient C_D was slightly under-predicted; in this case, the trend of aerodynamic coefficients was estimated with great precision even if the curve tends to slightly under-predict the aerodynamic coefficients at higher angle of attack.

In the second experiment [2], relative to the LEAPTech wing HEIST experiment, the lift coefficient C_L was estimated with discrete approximation and the drag coefficient C_D was slightly under-predicted; in this case, the trend of aerodynamic coefficients gave good results even if it does not match perfectly with CFD results.

In the third experiment [13], relative to the NACA 64_2015 airfoil in wind tunnel, the lift coefficient C_L was estimated with excellent approximation; in this case, the trend of aerodynamic coefficient was estimated with great precision even if the curve tended to slightly over-predict the lift coefficient at higher angle of attack.

In conclusion, DEP model generally shows good agreement with CFD results and experimental data both for aircraft with DEP system and for conventional aircraft made with few propellers. Following this validation phase, it is possible to considered the DEP model as a valid tool to estimate aerodynamic coefficients in an early phase of design of high-lift propeller systems.

Chapter 3 – Performance Sizing for DEP Aircraft

The purpose of this chapter is to describe an innovative performance-based sizing procedure for propeller-driven aircraft with the DEP system. For each aircraft performance requirement, a new formulation, conveniently accomodating propeller-driven aircraft with DEP system, is defined and a graphical illustration is provided. This allows assessing the standard performance requirement and the new performance requirement that considers the presence of the DEP system. The changes in the effects of the requirement with the increase of the number of distributed propellers N is considered. The new sizing approach is validated for the case of NASA X-57 Maxwell aircraft, highlighting strengths and weaknesses of DEP in relation to performance-based aircraft sizing.

3.1 Sizing Matrix Plot for Propeller-Driven aircraft

Referring to propeller-driven aircraft, two fundamental parameters determined during the preliminary design phase are the wing reference area S and engine power P_b. These two parameters will govern the aircraft size and the manufacturing cost, as well as the complexity of calculations. The design technique will be referred to as Sizing Matrix Plot (SMP) technique, and is sometimes cited also as the matching plot or matching chart, due to its graphical nature. This process determines the size of the two above-mentioned fundamental features of the aircraft, as ratios with respect to the aircraft maximum take-off weight W_{TO}. This phase tends to employ the outcomes of a calculation procedure where the parameters determined are not necessarily final in the first application and will be altered in subsequent phases in the aircraft design loop. In addition, in this phase, several design parameters are essential and will directly influence the entire preliminary design phase. Therefore, outmost care must be taken to insure the accuracy of the results of the preliminary sizing phase.
The construction of the SMP is solely dependent upon the aircraft performance requirements and employs elements of flight mechanics theory. Hence, the technique consists in an analytical approach.
The typical performance requirements utilized to size a civil aircraft in this phase are the following:

1. Stall speed V_S.
2. Take-off run S_{TO}.
3. Maximum cruise speed $V_{CR\ MAX}$.
4. Rate of climb ROC.
5. Climb gradient CGR.
6. Ceiling h_C.
7. Landing distance S_L.

In this section, two new parameters appear in almost all equations. Therefore, it is necessary to define them first, using the definitions found on M. H. Sandraey's book [26]:

a. Wing loading: the ratio between aircraft take-off weight and wing area is referred to as wing loading and represented by W_{TO}/S. This parameter indicates how much load is held by a unit area of the wing.

b. Power loading: the ratio between aircraft take-off weight and engine power is referred to as power loading (or weight-to-power ratio) and is represented by W_{TO}/P_b. This parameter indicates how heavy the aircraft is with respect to engine power. This term is associated with propeller-driven aircraft (turboprop or piston engines) only, as for jet-driven aircraft the thrust-to-weight ratio is preferred.

In order to construct the SMP, it is necessary to derive an equation for each aircraft performance requirement, generating a family of functions, as shown is the following equation, where the function subscripts refer to the numbered items in the requirement list previously detailed:

$$\begin{cases} \left(\frac{W_{TO}}{P_b}\right) = f_1\left(\frac{W_{TO}}{S}, V_S\right) \\ \left(\frac{W_{TO}}{P_b}\right) = f_2\left(\frac{W_{TO}}{S}, S_{TO}\right) \\ \left(\frac{W_{TO}}{P_b}\right) = f_3\left(\frac{W_{TO}}{S}, V_{CR\ MAX}\right) \\ \left(\frac{W_{TO}}{P_b}\right) = f_4\left(\frac{W_{TO}}{S}, ROC\right) \\ \left(\frac{W_{TO}}{P_b}\right) = f_5\left(\frac{W_{TO}}{S}, CGR\right) \\ \left(\frac{W_{TO}}{P_b}\right) = f_6\left(\frac{W_{TO}}{S}, h_C\right) \\ \left(\frac{W_{TO}}{P_b}\right) = f_7\left(\frac{W_{TO}}{S}, S_L\right) \end{cases} \tag{68}$$

The above equations are graphically shown in a plot where the vertical axis is power loading W_{TO}/P_b and the horizontal axis is wing loading W_{TO}/S. Generally speaking, the region matching the requirement lies below of the corresponding curve in such plot (or to the left in the case of a vertical line). The resulting curves intersect, producing a partition of the plane in several regions. The overall feasibility region is the one in which all aircraft performance requirements are met. In order to understand the development of an acceptable region, an example of SMP diagram is shown in Figure 3.1. The blue-shaded area corresponds to the feasibility region, as it lies below all the curves representing.

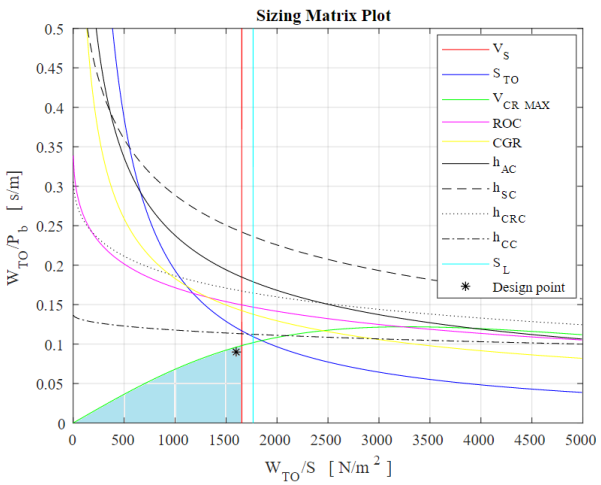

Figure 3.1: Example of Sizing Matrix Plot for preliminary sizing of an airplane.

As explained in reference [29], the SMP is employed to determine the optimum selection that correspond to the design point, represented with black asterisk in Figure 3.1. The design point on the plot is typically chosen as one that yields the smallest engine in terms of power (i.e. the lowest cost), while complying with stalling speed requirements. From the design point, it is possible to obtain the corresponding wing loading W_{TO}/S and corresponding power loading W_{TO}/P_b. If the performance requirements are met with some margins, the design point may lie in the feasibility region, not necessarily exactly on one or more specific curves. In the following sections, the derivations of equations for each performance requirement are carried out using mathematical and practical methods.

3.2 Aerodynamic coefficients

All the equations derived for the SMP involve the aircraft aerodynamic coefficients, so that expressing their variations as functions of the wing loading W_{TO}/S and the power loading W_{TO}/P_b is clearly a priority.

Before the analysis of the equations contained in the implemented DEP model, it is necessary to introduce some parameters which will be used in the next steps. The effective wingspan b_e is expressed as the difference between the wing span b and the fuselage width b_f,

$$b_e = b - b_f \tag{69}$$

The geometric parameter ζ takes into consideration the position of the propellers along the DP array: if the propeller is located near the tip, ζ will be equal to ½; otherwise, ζ will be equal to one.

The geometric parameter ξ represents the span wise separation between each propeller along the DP array. In the preliminary sizing process, the propeller diameter D can be expressed as a function of the effective wingspan and the two geometric parameters previously mentioned, as seen below:

$$D = \frac{1}{1+\xi}\frac{b_e}{N + 2(\zeta - 1)} \tag{70}$$

Figure 3.2 shows the geometry parameters as defined above.

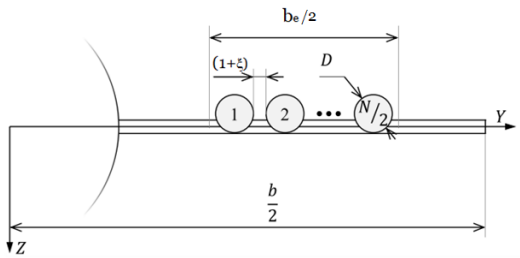

Figure 3.2: Frontal view of the DEP model, indicating the geometrical parameters [6].

The geometric parameter δ is the ratio between the propeller diameter D and the wing span b. Following this approach, δ can be expressed as a function of the number of propellers for the DEP system, the effective wingspan and the two geometric parameters, as

$$\delta = \frac{D}{b} = \frac{1}{1+\xi}\left(\frac{b_e}{b}\right)\frac{1}{N+2(\zeta-1)} \tag{71}$$

For the sake of simplicity, it is possible to consider the case in which ζ is equal to one and ξ is equal to zero for all propellers along the wingspan. In this case,

$$\delta = \frac{D}{b} = \left(\frac{b_e}{b}\right)\frac{1}{N} = \delta\left(N, \frac{b_e}{b}\right) \tag{72}$$

In order to illustrate this simplification, the computation of the geometric parameter δ is performed for the NASA X-57 Maxwell aircraft, as presented in Table 3.1.

Input data	Numeric values	Units
b	9.6	m
b_f	1.22	m
b_e	8.38	m
N	12	—
D	0.579	m
b_e/b	0.873	—
ξ	0	—
ζ	1	—

Table 3.1: Input data for the computation of parameter δ with DEP model.

With these input data, it is possible to obtain an approximated value of δ = 0.072 which is very close to the real value δ_{real} = 0.06 of the NASA X-57 Maxwell. This highlights that the simplified procedure of Equation 72 is acceptable for the present situation. From now on, the ratio between the effective wingspan and the total wingspan b_e/b will be considered constant with respect to the increase of the number of propellers N along the DP array.

Starting from the implemented DEP model, the first step is to express the non-dimensional thrust coefficient of single propeller T_c as a function of thrust as

$$T_c = \frac{T_{DP}}{N\rho V^2 D^2} = \frac{T\,\chi}{N\rho V^2 D^2} = \frac{\chi}{N\rho V^2}\frac{T}{W_{TO}}\frac{W_{TO}}{S}\frac{S}{D^2} \tag{72}$$

and therefore of power as

$$T_c = \frac{\chi \eta_P}{N\rho V^3}\frac{P_b}{W_{TO}}\frac{W_{TO}}{S}\frac{b^2}{AR\,D^2} = \frac{\chi \eta_P}{N\rho V^3}\left(\frac{W_{TO}}{P_b}\right)^{-1}\left(\frac{W_{TO}}{S}\right)\frac{1}{AR\,\delta^2} \tag{73}$$

The new parameters introduced in the above equations are the thrust of the DP system T_{DP} and the parameter χ that is the ratio between the thrust of the DP system and the total thrust of the aircraft. Following the previous approach, T_c can be evaluated as a function of the two variables of the SMP, the number of propellers along the DP array and the two geometric parameters:

$$T_c = \frac{\chi \eta_P}{N\rho V^3}\left(\frac{W_{TO}}{P_b}\right)^{-1}\left(\frac{W_{TO}}{S}\right)\frac{1}{AR}\frac{(1+\xi)^2(N+2(\zeta-1))^2}{(b_e/b)^2} = T_c\left(\frac{W_{TO}}{S},\frac{W_{TO}}{P_b},N,\xi,\zeta\right) \tag{74}$$

The simple procedure gives an expression of T_c as function of only three variables for all propellers along the DP array. This expression drastically reduces the complexity of the equation:

$$T_c = \frac{\chi \eta_P}{\rho V^3}\left(\frac{W_{TO}}{P_b}\right)^{-1}\left(\frac{W_{TO}}{S}\right)\frac{N}{AR\,(b_e/b)^2} = T_c\left(\frac{W_{TO}}{S},\frac{W_{TO}}{P_b},N\right) \tag{75}$$

From now on, the dependence on geometric parameters shall be discarded, keeping only the dependence on wing loading, power loading and number of propellers.
The second step is to compute the axial induction factor at the propeller disk a_P as a function of the three variables previously mentioned:

$$a_P = \frac{V_P - V}{V} = \frac{1}{2}\left(\sqrt{1+\frac{8\,T_c}{\pi}} - 1\right) \tag{76}$$

$$a_P = \frac{1}{2}\left(\sqrt{1+\frac{8}{\pi}\left[\frac{\chi \eta_P}{N\rho V^3}\left(\frac{W_{TO}}{P_b}\right)^{-1}\left(\frac{W_{TO}}{S}\right)\frac{1}{AR}\frac{(1+\xi)^2\left(N+2(\zeta-1)\right)^2}{(b_e/b)^2}\right]} - 1\right) \tag{77}$$

$$a_P = a_P\left(\frac{W_{TO}}{S},\frac{W_{TO}}{P_b},N\right) \tag{78}$$

Following the theory elaborated for the DEP model, the axial induction factor at wing leading edge a_w can be expressed as a function of the two variables of the SMP and the number of propellers N along the DP array:

$$a_w = \frac{a_P+1}{\left(\frac{R_W}{R}\right)^2} - 1 = 1 + a_P\left(1+\frac{\frac{x}{R}}{\sqrt{\left(\frac{x}{R}\right)^2+1}}\right) - 1 = a_P\left(1+\frac{\frac{x}{R}}{\sqrt{\left(\frac{x}{R}\right)^2+1}}\right) \tag{79}$$

$$a_w = \frac{1}{2}\left(\sqrt{1+\frac{8}{\pi}\left[\frac{\chi\,\eta_P}{N\rho V^3}\left(\frac{W_{TO}}{P_b}\right)^{-1}\left(\frac{W_{TO}}{S}\right)\frac{1}{AR}\frac{(1+\xi)^2\left(N+2(\zeta-1)\right)^2}{(b_e/b)^2}\right]}-1\right)\left(1+\frac{\frac{x}{R}}{\sqrt{\left(\frac{x}{R}\right)^2+1}}\right) \tag{80}$$

$$a_w = a_w\left(\frac{W_{TO}}{S}, \frac{W_{TO}}{P_b}, N\right) \tag{81}$$

In order to compute the finite-slipstream correction factor β, a surrogate model is developed in Patterson's dissertation [8] as a function of three design parameters:

1. The ratio of the disk radius to the chord of the airfoil (R/c).
2. The velocity of the contracted slipstream far downstream of the disk.
3. The distance upstream of the leading edge the disk is placed.

For the model developed, the vertical height of the disk and the angle of the disk relative to the freestream are kept constant. To make data obtained from simulations useful in a computational design environment, the surrogate model is fit to the data. To fit the surrogate model, four separate fourth-order polynomials in the form of the following equation are fit to the data in order to obtain the factor β. The resulting values of the coefficient row vectors are given in the next equations and these thirty numbers define the surrogate model:

$$\begin{cases} K_0 = [0.378269\ 0.748135\ -0.179986\ -0.056464\ -0.146746\ -0.015255] \\ K_1 = [3.071020 - 1.769885\ 0.436595\ 0.148643\ -0.9889332\ 0.197940] \\ K_2 = [-2.827730\ 2.054064\ -0.467410\ -0.277325\ 0.698981\ -0.008226] \\ K_3 = [0.997936\ -0.916118\ 0.199829\ 0.157810\ -0.143368\ -0.057385] \\ K_4 = [-0.127645\ 0.135543\ -0.028919\ -0.026546\ 0.010470\ 0.012221] \end{cases} \tag{82}$$

The final surrogate model to determine β can be represented in a single equation, where it is highlighted the dependence by the engine thrust from the axial induction factor at propeller disk a_P:

$$\begin{cases} \beta = K_0 X + K_1 X\left(\frac{R}{c}\right) + K_2 X\left(\frac{R}{c}\right)^2 + K_3 X\left(\frac{R}{c}\right)^3 + K_4 X\left(\frac{R}{c}\right)^4 \\ X = \left[1 \quad x_C \quad (x_C)^2 \quad (x_C)(2a_p+1) \quad (2a_p+1) \quad (2a_p+1)^2\right]^T \end{cases} \tag{83}$$

According to Patterson's theory, $\beta = 1$ is imposed as an effective upper limit. The sectional lift coefficient increase in the DEP model implemented depends by the axial induction factor at wing leading edge a_w and by the finite-slipstream correction factor β. This implies that it is possible to express the sectional lift coefficient as function of the two variables of the SMP and the number of propellers N:

$$\Delta C_l = 2\pi\left[(\sin\alpha - a_w\beta\sin i_p)\sqrt{a_w^2\beta^2 + 2a_w\beta\cos(\alpha+i_p)+1} - \sin\alpha\right] \tag{84}$$

$$\Delta C_l = \Delta C_l\left(\frac{W_{TO}}{S}, \frac{W_{TO}}{P_b}, N\right) \tag{85}$$

where the parameter α is the geometric angle of attack of the wing and i_P is the angle between the propeller axis and the wing chord. Since in the sizing process the angle of attack of the wing is unknown, this has to be estimated using the three-dimensional lift coefficient. For this, the expression presented by Roskam [15] can be used to determine α as

$$\alpha = \left(\frac{C_{L\,u}}{2\pi AR}\right)\left[2 + \sqrt{AR^2(1-M^2)\left(1 + \frac{tan^2(\Lambda_{c/2})}{1-M^2}\right) + 4}\right] \tag{87}$$

In the above equation M is the freestream Mach number and $\Lambda_{c/2}$ the wing half-chord sweep angle. The angle between the propeller axis and the wing chord i_p, can be computed with the following equation:

$$i_p = \varphi - \alpha - \alpha_{twist} \tag{88}$$

Following Patterson's extension to three dimensions [8], the percentage lift increase of the wing section and the percentage of the span in the propeller slipstream of section are combined with all other sections to give the net effect on the entire wing. This term can be manipulated for the preliminary design phase in order to be function of the two variables of the SMP:

$$\Delta C_L = \sum_{i=1}^{N} (\Delta C_l)_i \left(\frac{b_{blown}}{b}\right)_i = N \Delta C_l \left(\frac{W_{TO}}{S}, \frac{W_{TO}}{P_b}, N\right)\left(\frac{b_{blown}}{b}\right) \tag{89}$$

$$\Delta C_L = N \Delta C_l \left(\frac{W_{TO}}{S}, \frac{W_{TO}}{P_b}, N\right)\left(\frac{D}{b}\right)\sqrt{\frac{1 + a_P\left(\frac{W_{TO}}{S}, \frac{W_{TO}}{P_b}, N\right)}{1 + a_P\left(\frac{W_{TO}}{S}, \frac{W_{TO}}{P_b}, N\right)\left(1 + \frac{\frac{x}{R}}{\sqrt{\left(\frac{x}{R}\right)^2 + 1}}\right)}} \tag{90}$$

$$\Delta C_L = \left(\frac{b_e}{b}\right) \Delta C_l \left(\frac{W_{TO}}{S}, \frac{W_{TO}}{P_b}, N\right)\sqrt{\frac{1 + a_P\left(\frac{W_{TO}}{S}, \frac{W_{TO}}{P_b}, N\right)}{1 + a_P\left(\frac{W_{TO}}{S}, \frac{W_{TO}}{P_b}, N\right)\left(1 + \frac{\frac{x}{R}}{\sqrt{\left(\frac{x}{R}\right)^2 + 1}}\right)}} \tag{91}$$

$$\Delta C_L = \Delta C_L \left(\frac{W_{TO}}{S}, \frac{W_{TO}}{P_b}, N\right) \tag{92}$$

In order to illustrate the behaviour of the lift coefficient increased due to the DEP respect to the increase of number of propellers N considered along the wingspan, Figure 3.3 shows this result for the stall configuration of the NASA X-57 Maxwell aircraft with the DEP model implemented.

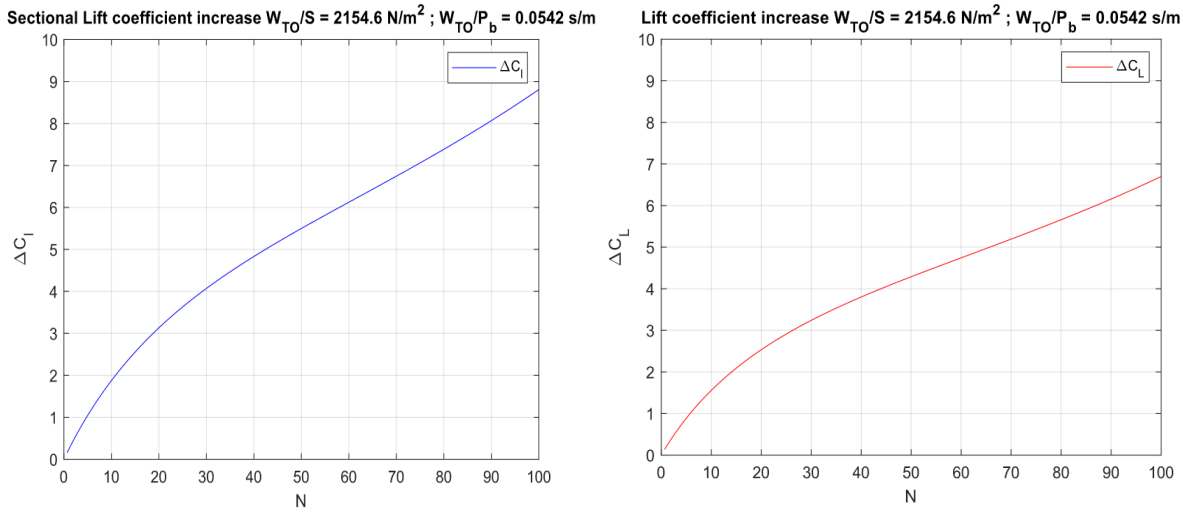

Figure 3.3: Increase in lift coefficient respect to the number of propellers considered with DEP system in stall configuration.

Next, expressing the increase of drag coefficient as function of the wing loading W_{TO}/S, the power loading W_{TO}/P_b and the number of propellers N for the DEP system is in order. Firstly, the increase in zero-lift drag is related to the increase in friction drag on the wing surface due to increased dynamic pressure in the slipstream. This contribution can be manipulated using the DEP approach as

$$\Delta C_{D0} = \sum_{i=1}^{N} a_w^2 c_f \cdot \left(\frac{b_{blown}}{b}\right)_i = N\, a_w^2 c_f \cdot \left(\frac{b_{blown}}{b}\right) \tag{93}$$

$$\Delta C_{D0} = N\, a_w^2 c_f \left(\frac{D}{b}\right) \sqrt{\frac{1 + a_P\left(\frac{W_{TO}}{S}, \frac{W_{TO}}{P_b}, N\right)}{1 + a_P\left(\frac{W_{TO}}{S}, \frac{W_{TO}}{P_b}, N\right)\left(1 + \frac{\frac{x}{R}}{\sqrt{\left(\frac{x}{R}\right)^2 + 1}}\right)}} \tag{94}$$

$$\Delta C_{D0} = \left(\frac{b_e}{b}\right) a_w^2\left(\frac{W_{TO}}{S}, \frac{W_{TO}}{P_b}, N\right) c_f \sqrt{\frac{1 + a_P\left(\frac{W_{TO}}{S}, \frac{W_{TO}}{P_b}, N\right)}{1 + a_P\left(\frac{W_{TO}}{S}, \frac{W_{TO}}{P_b}, N\right)\left(1 + \frac{\frac{x}{R}}{\sqrt{\left(\frac{x}{R}\right)^2 + 1}}\right)}} \tag{95}$$

$$\Delta C_{D0} = \Delta C_{D0}\left(\frac{W_{TO}}{S}, \frac{W_{TO}}{P_b}, N\right) \tag{96}$$

Referring to the DEP model, the increase in lift-induced drag can be attributed to an increase in C_L on one hand, and to a change in the Oswald factor on the other. The former can be estimated by assuming a parabolic polar, so that:

$$\Delta C_{Di} = \frac{\Delta C_L^2\left(\frac{W_{TO}}{S}, \frac{W_{TO}}{P_b}, N\right) + 2C_{Lu}\,\Delta C_L\left(\frac{W_{TO}}{S}, \frac{W_{TO}}{P_b}, N\right)}{\pi\, AR\, e} = \Delta C_{Di}\left(\frac{W_{TO}}{S}, \frac{W_{TO}}{P_b}, N\right) \tag{97}$$

The parameter C_{Lu} represents the isolated lift coefficient relative to an unblown wing without the presence of the DEP system. The total increase in drag coefficient is given by the summation of the two terms that are the drag coefficient due to friction and dynamic pressure ΔC_{D0} and the drag coefficient induced by the lift force ΔC_{Di}:

$$\Delta C_D = \Delta C_{D0}\left(\frac{W_{TO}}{S}, \frac{W_{TO}}{P_b}, N\right) + \Delta C_{Di}\left(\frac{W_{TO}}{S}, \frac{W_{TO}}{P_b}, N\right) = \Delta C_D\left(\frac{W_{TO}}{S}, \frac{W_{TO}}{P_b}, N\right) \tag{98}$$

In order to illustrate the behaviour of the drag coefficient increased due to the DEP respect to the increase of number of propellers N considered, Figure 3.4 shows this result for the stall configuration of the NASA X-57 Maxwell aircraft with the implemented DEP model.

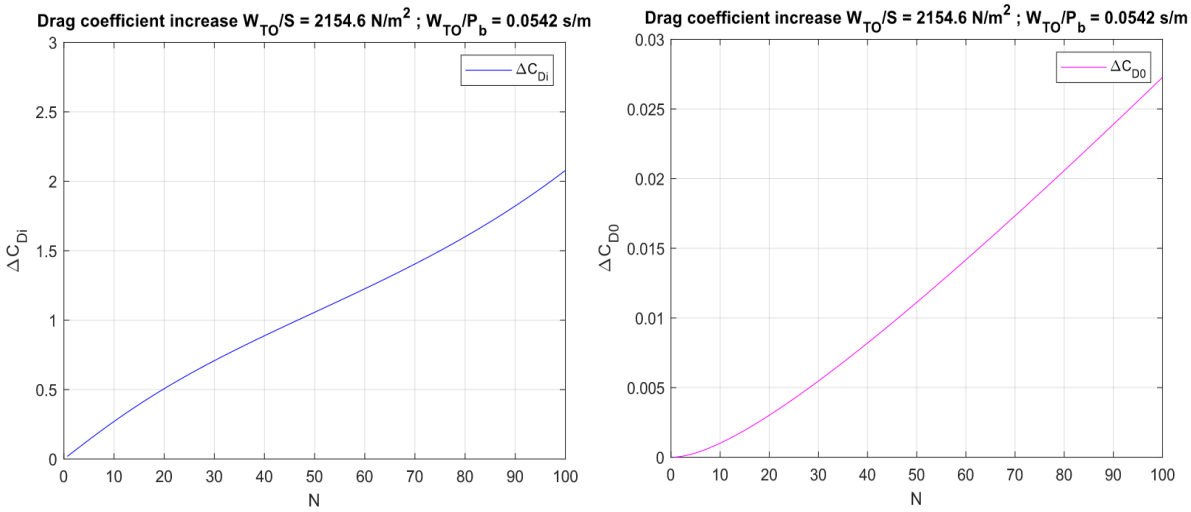

Figure 3.4: Increase in drag coefficient respect to the number of propellers considered for DEP system in stall configuration.

Finally, we can express all aerodynamic coefficients as function of wing loading W_{TO}/S and power loading W_{TO}/P_b, in order to correctly represent each performance requirement as a family of functions that generate the SMP:

$$\begin{cases} C_L = C_{L\,u} + \Delta C_L\left(\frac{W_{TO}}{S}, \frac{W_{TO}}{P_b}, N\right) \\ C_D = C_{D\,u} + \Delta C_D\left(\frac{W_{TO}}{S}, \frac{W_{TO}}{P_b}, N\right) \end{cases} \tag{99}$$

$$C_D = C_{D0\,u} + C_{Di\,u} + \Delta C_{D0}\left(\frac{W_{TO}}{S}, \frac{W_{TO}}{P_b}, N\right) + \Delta C_{Di}\left(\frac{W_{TO}}{S}, \frac{W_{TO}}{P_b}, N\right) \tag{100}$$

Parameters $C_{D\,u}$, $C_{Do\,u}$ and $C_{Di\,u}$ represents the isolated drag coefficients relative to an unblown wing without the presence of the DEP system. The delta lift coefficients are expressed as function of the wing loading, the power loading and the number of propellers for DEP. We remark that they also depend on the geometric characteristic of the considered aircraft and on aircraft speed. The choice of avoiding ther explicit reference to these dependencies is made to make the equations clearer and to highlight the link with the most important parameters of the SMP.

3.3 Aircraft Performance Requirements

In the following parts, the family of functions representing each of the aircraft performance requirements is derived for the case with the implemented DEP model, in order to determine the possible improvements that can be achieved with the DEP system. All the equations are computed starting from the actual performance requirements for the case without the DEP system, also called conventional case. These equations are modified in a way to consider the effect of the DEP system with the help of the implemented model.

3.3.1 Stall speed

The stall speed requirement is a limit to the minimum allowable operating speed. In general, a low stall speed is desirable, since this results in a safer aircraft.
This requirement for electric aircraft with DEP model is evaluated following the description presented in Roskam [28].. The altitude must be chosen to be at sea level, since it provides the highest air density, which results in the lowest stall speed.
The equation is developed in the conventional case from the vertical equilibrium equation, dividing both sides by the wing surface:

$$\left(\frac{W_{TO}}{S}\right) - \frac{1}{2}\rho_0 V_S^2\, C_{L\,MAX} = 0 \tag{101}$$

In order to adapt the stall speed requirement with the DEP model implemented, it is possible to express the lift coefficient as the summation of the lift coefficient with unblown wing and the delta lift coefficient derived in the above section as function of the two variables of the SMP:

$$\left(\frac{W_{TO}}{S}\right) - \frac{1}{2}\rho_0 V_S^2 \left[C_{L\,u\,MAX} + \Delta C_{L\,MAX}\left(\frac{W_{TO}}{S}, \frac{W_{TO}}{P_b}, N\right)\right] = 0 \tag{102}$$

The delta lift coefficient represents the increase of the lift coefficient with the DEP model implemented. This equation provides the first graph in the SMP with DEP model, represented with the blue solid line in Figure 3.5 (left) and compared to the constraint relative to the conventional case represented with

red solid line. In the Figure 3.5 (right), it is possible to see the behaviour of the stall speed requirement with the increase of the number of propellers *N* along the DP array.

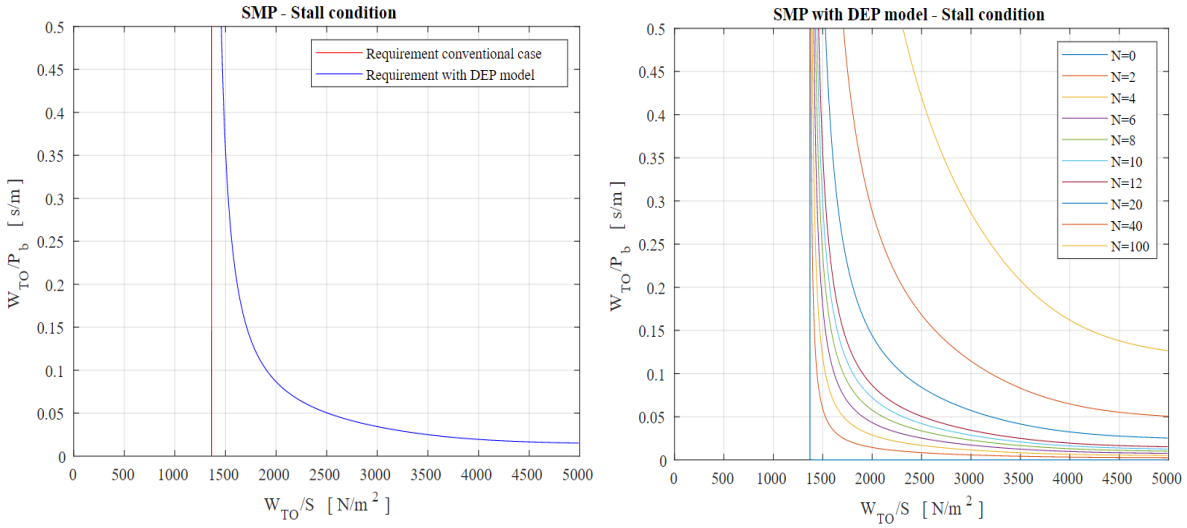

Figure 3.5: Stall speed contribution in constructing the SMP with DEP model.

The stall speed requirement tends to increase the acceptable region for the determination of the design point with the increase of the number of propellers *N* used for the DEP, generating a great advantage in the development of the preliminary design phase. In the conventional case, the wing sizing based on stall speed requirement is represented as the variations of wing loading versus stall speed. As can be seen from the above left figure, the power loading W_{TO}/P_b does not contribute to wing loading in this case. In other words, the wing loading to satisfy the stall speed requirements is not a function of power loading in the conventional case while the stall speed equation depends also by the power loading in the case with DEP model. Therefore, it is possible to see that the graph of power loading versus wing loading is a vertical line in the conventional case while it becomes a hyperbolic curve in the case with DEP model. Making a comparison between the conventional case and the SMP with DEP model, the stall speed requirement derived with DEP model fits perfectly with the vertical line of the conventional unblown case when it is considered *N* equal to zero (without DEP system), confirming the accuracy of the procedure.
Any stall speed lower than the value specified by the mission requirements is acceptable. Therefore, the left side of the graph is an acceptable region and on the right side, the stall requirements is not met.

3.3.2 Take-off run

The take-off run is another significant factor in aircraft performance and it is employed in constructing the SMP to determine wing area and engine power. The take-off requirements are frequently spelled out in terms of minimum ground run requirements, since every airport has a limited runway. The take-off run S_{TO} is defined as the distance between the take-off starting point to the location of a standard

obstacle that the aircraft must clear. The aircraft is required to clear an imaginary obstacle at the end of the airborne section, so the take-off run includes a ground section S_{TOG} plus an airborne section (Figure 3.6).

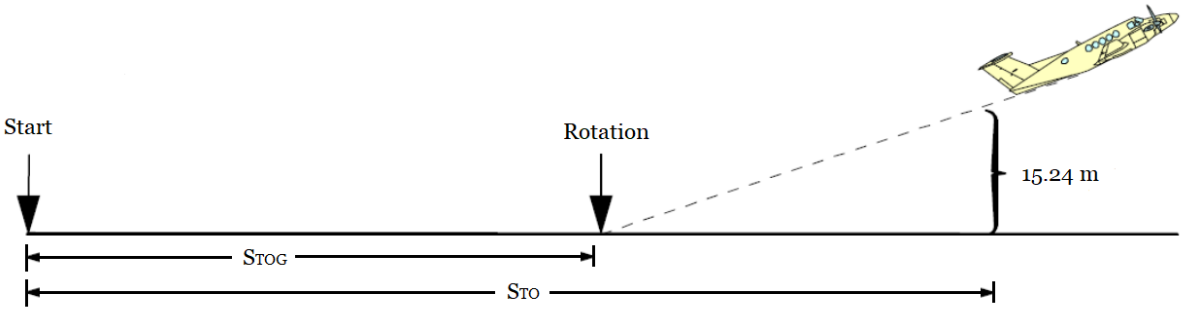

Figure 3.6: The definition of take-off run.

The obstacle height is determined by airworthiness standards. For aircraft certificated with CS Part 23, referred to multi-engine aircraft with a Maximum Take-Off Weight (MTOW) of less than 2722 kg, the obstacle height is 15.24 m (50 ft) and the standard requirement for a preliminary design phase is presented in Roskam [28] in the conventional case. The take-off run S_{TO} is related to the Take-Off Parameter CS Part 23 (TOP_{23}); this parameter is obtained experimentally for a range of single and twin engines certified airplanes related to the CS Part 23:

$$S_{TO} = 8.134\, TOP_{23} + 0.0149 TOP_{23}^2 \tag{103}$$

The take-off requirement is obtained starting from the principle of work-energy and expressing the take-off speed as a function of the wing loading and the lift coefficient in take-off configuration:

$$\left(\frac{W_{TO}}{P_b}\right) = \frac{TOP_{23}\left(\frac{\rho_{TO}}{\rho_0}\right) C_{L\,\mathrm{MAX}\,TO}}{\left(\frac{W_{TO}}{S}\right)} \tag{104}$$

For aircraft certified with CS Part 25, the obstacle height is 10.67 m (35 ft) and the standard requirement for a preliminary design phase is presented in Roskam [28] in the conventional case. The take-off run S_{TO} is correlated to the Take-Off Parameter CS Part 25 (TOP_{25}); this parameter is obtained experimentally for a range of two-, three- and four-engine certified airplanes related to CS Part 25.

$$S_{TO} = \frac{TOP_{25}}{4.189} \tag{105}$$

The take-off requirement is obtained starting from the principle of work-energy and expressing the take-off speed as a function of the wing loading and the lift coefficient in take-off configuration:

$$\left(\frac{W_{TO}}{P_b}\right) = 0.0167 \frac{TOP_{25}\left(\frac{\rho_{TO}}{\rho_0}\right) C_{L\,MAX\,TO}}{\left(\frac{W_{TO}}{S}\right)} \tag{106}$$

Since there are not historical regression data between the take-off parameter and the take-off run for electric aircraft with DEP system, Roskam's expression of the take-off requirement is not usable in this case. It is possible to evaluate this requirement for electric aircraft with DEP model following the description presented in Sadraey [26, 31]. The take-off operation is considered as an accelerating motion, so the aircraft speed is not constant. The aircraft speed varies quickly from zero to rotation speed and then to take-off speed. The take-off speed is normally slightly greater than the stall speed ($1.1V_S$ to 1.3 V_S). Based on Newton's second law, the summation of all forces generates the change in aircraft momentum during the ground section:

$$T - D - F_f = m_{TO}a \tag{107}$$

In the above equation the acceleration a has a positive value, the parameter m_{TO} represents the aircraft mass in take-off configuration, the force F_f is the friction force, the parameter T is the engine thrust and D is the aircraft drag. All forces during ground section can be expressed with the following equations,

$$\begin{cases} F_f = \mu\,(W_{TO} - L_{TO}) = \mu\left(W_{TO} - \frac{1}{2}\rho_0 V^2 S C_{L\,TO}\right) \\ D = \frac{1}{2}\rho_0 V^2 S C_{D\,TO} \end{cases} \tag{108}$$

The friction force is proportional to the normal component, which is the algebraic sum of the aircraft weight and aerodynamic lift. The coefficient μ is static rolling friction coefficient and it is considered the standard value of μ for dry concrete/asphalt surface. Aerodynamic coefficients $C_{L\,TO}$ and $C_{D\,TO}$ are referred to take-off ground configuration. The instantaneous acceleration during ground section can be expressed in this way as

$$a = \frac{T - D - F_f}{m_{TO}} \tag{109}$$

Defining the velocity as the rate of change of displacement with time, the ground section S_{TOG} can be determined integrating the ratio between the velocity and the acceleration during ground phase as

$$S_{TOG} = \int_0^{V_R} \frac{V}{a} dV = \int_0^{V_R} \frac{m_{TO}V}{T - D - F_f} dV \tag{110}$$

Considering the complete expressions of the drag force and the friction force, the dependence from velocity can be highlighted in the integral with the following procedure:

$$S_{TOG} = \int_0^{V_R} \frac{m_{TO} V}{T - \mu W_{TO} - \frac{1}{2}\rho_0 V^2 S(C_{D\,TO} - \mu C_{L\,TO})} dV = \int_0^{V_R} \frac{V}{A + BV^2} dV \tag{111}$$

This integration can be directly solved using a mathematical approach, after splitting terms in two parameters *A* and *B*, with the following solution:

$$\begin{cases} S_{TOG} = \dfrac{1}{2B} \ln\left(\dfrac{A + BV_R^2}{A}\right) \\ A = \dfrac{T}{m_{TO}} - \mu\, g \\ B = -\dfrac{1}{2}\dfrac{\rho_0 S}{m_{TO}}(C_{D\,TO} - \mu C_{L\,TO}) \end{cases} \tag{112}$$

When *A* and *B* are substituted in the complete expression, we have the new formula for the ground section in take-off:

$$S_{TOG} = \frac{\left(\frac{W_{TO}}{S}\right)}{g\rho_0 (C_{D\,TO} - \mu C_{L\,TO})} \ln\left[\frac{\frac{T}{W_{TO}} - \mu}{\frac{T}{W_{TO}} - \mu - \frac{1}{2}\rho_0 \left(\frac{S}{W_{TO}}\right) V_R^2 (C_{D\,TO} - \mu C_{L\,TO})}\right] \tag{113}$$

The parameter $C_{L\,R}$ is the aircraft lift coefficient at take-off rotation, related to the rotation speed V_R and it is obtained from the vertical equilibrium equation,

$$C_{L\,R} = \frac{2\left(\frac{W_{TO}}{S}\right)}{\rho_0 V_R^2} \tag{114}$$

The expression of the take-off run can be derived from ground section using Roskam's assumption, replacing the compact expression of the aircraft lift coefficient at take-off rotation and considering the expression of engine thrust for propeller-driven aircraft:

$$S_{TO} = 1.65\, S_{TOG} = \frac{1.65\left(\frac{W_{TO}}{S}\right)}{g\,\rho_0\ (C_{D\,TO} - \mu C_{L\,TO})} \ln\left[\frac{\frac{\eta_P}{V_{TO}}\left(\frac{P_b}{W_{TO}}\right) - \mu}{\frac{\eta_P}{V_{TO}}\left(\frac{P_b}{W_{TO}}\right) - \mu - g\rho_0 \frac{(C_{D\,TO} - \mu C_{L\,TO})}{C_{L\,R}}}\right] \tag{115}$$

From this expression of the take-off run it is possible to derive the take-off requirement with the wing loading and the power loading as variables of the SMP as

$$\left(\frac{W_{TO}}{P_b}\right)\frac{V_{TO}}{\eta_P} - \frac{1 - \exp\left(0.6\,\rho_{TO} g\,(C_{D\,TO} - \mu C_{L\,TO}) S_{TO}\left(\frac{W_{TO}}{S}\right)^{-1}\right)}{\mu - \left(\mu + \frac{(C_{D\,TO} - \mu C_{L\,TO})}{C_{L\,R}}\right)\left[\exp\left(0.6\,\rho_{TO} g\,(C_{D\,TO} - \mu C_{L\,TO}) S_{TO}\left(\frac{W_{TO}}{S}\right)^{-1}\right)\right]} = 0 \tag{116}$$

In order to use the same procedure for the case with DEP system, it is important to remark that aerodynamic coefficients increased due to the DEP are functions of the aircraft speed, so that the previous integral cannot be solved with the same mathematical approach seen before. However, given the complexity of the resulting integral and the limited dependence on speed of the delta terms, we chose to neglect the dependence of the aerodynamic coefficients from the aircraft speed, solving the integral with the same mathematical approach. In light of these considerations, it is possible to use the Sadraey's take-off requirement with the aerodynamic coefficients as the summation of the aerodynamic coefficients with unblown wing and the delta coefficients derived in the above section as function of the two variables of the SMP:

$$\left(\frac{W_{TO}}{P_b}\right)\frac{V_{TO}}{\eta_P} - \frac{1-\exp\left(0.6\,\rho_{TO} g\,(C_{D\,TO}{}^{*}-\mu C_{L\,TO}{}^{*})S_{TO}\left(\frac{W_{TO}}{S}\right)^{-1}\right)}{\mu-\left(\mu+\frac{(C_{D\,TO}{}^{*}-\mu C_{L\,TO}{}^{*})}{C_{L\,R}{}^{*}}\right)\left[\exp\left(0.6\,\rho_{TO} g\,(C_{D\,TO}{}^{*}-\mu C_{L\,TO}{}^{*})S_{TO}\left(\frac{W_{TO}}{S}\right)^{-1}\right)\right]} = 0 \tag{117}$$

$$\begin{cases} C_{L\,TO}{}^{*} = C_{L\,u\,TO} + \Delta C_{L\,TO}\left(\dfrac{W_{TO}}{S}, \dfrac{W_{TO}}{P_b}, N\right) \\ C_{D\,TO}{}^{*} = C_{D\,u\,TO} + \Delta C_{D\,TO}\left(\dfrac{W_{TO}}{S}, \dfrac{W_{TO}}{P_b}, N\right) \\ C_{L\,R}{}^{*} = C_{L\,u\,R} + \Delta C_{L\,R}\left(\dfrac{W_{TO}}{S}, \dfrac{W_{TO}}{P_b}, N\right) \end{cases} \tag{118}$$

The delta coefficients also depends on take-off speed, which is expressed as function of the wing loading and the unblown lift coefficient with the vertical equilibrium equation in the referred configuration. This equation provides the second graph in the SMP with DEP model, represented with the blue solid line in Figure 3.7 (left) and compared to the constraint relative to the conventional case represented with red solid line. In Figure 3.7 (right), it is possible to see the behaviour of the take-off requirement with the increase of the number of propellers *N* along the DP array.

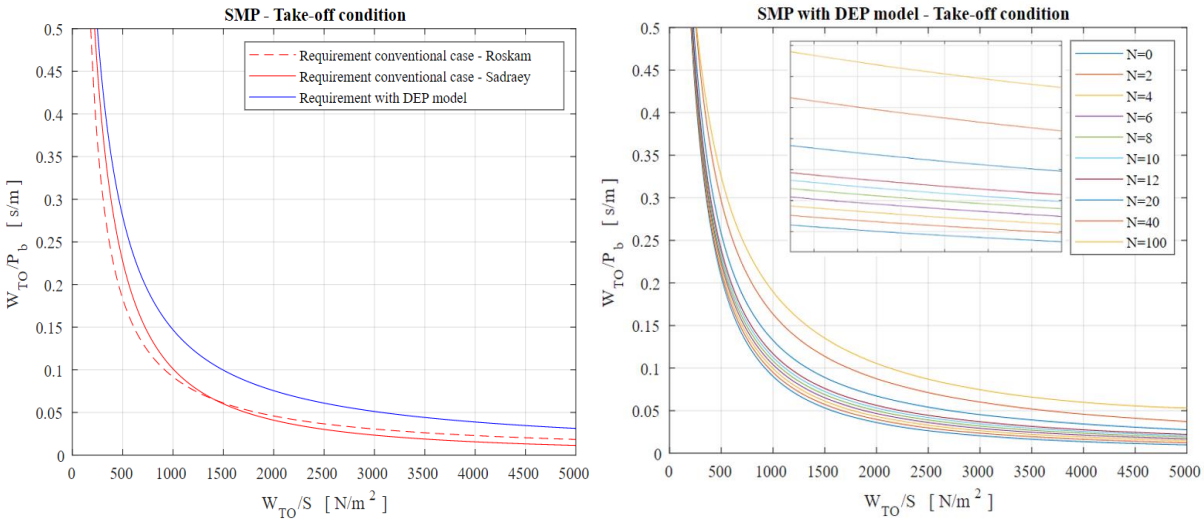

Figure 3.7: Take-off run contribution in constructing the SMP with DEP model.

The take-off requirement with Roskam's formulation is also shown; it has a trend similar to the one found in Sadraey's formulation for high values of wing loading and it tends to be less restrictive for small values of the wing loading. The plot on the right shows that take-off run requirement tends to increase the acceptable region for the determination of the design point with the increase of the number of propellers *N* used for the DEP, generating a great advantage for the selection of the design point. In the conventional case, the wing sizing based on take-off run requirement is represented as the variations of power loading versus wing loading. Comparing the conventional case and the SMP with DEP model it is possible to see that both the constraints have a hyperbolic behaviour with similar shape and slope. The take-off run requirement derived with DEP model fits perfectly with the hyperbolic curve of the conventional unblown case when it is considered *N* equal to zero (without DEP system), confirming the accuracy of the procedure.
As the take-off run S_{TO} is increased, the magnitude of the exponential term will increase. As the value of S_{TO} is increased, the value of power loading W_{TO}/P_b will go up. Since any value of S_{TO} greater than the specified take-off run is not satisfying the take-off run requirement, the region above the graph is not acceptable.

3.3.3 Maximum cruise speed

Another very important performance requirement is the maximum speed. This requirement for electric aircraft with DEP model is evaluated following the description presented in Sadraey [26] for FAR Part 23, referred to a propeller-driven aircraft which is flying with the maximum constant speed at a specified altitude. The aircraft is in longitudinal trim, hence the maximum available engine power must be equal to the maximum required power, which is thrust multiplied by maximum speed. The maximum cruise speed equation is developed in [26] for the conventional case, starting from the vertical equilibrium and the horizontal equilibrium in trim configuration, in order to express the dependence from the wing loading and the power loading:

$$\left(\frac{W_{TO}}{S}\right)\left(\frac{\rho_{CR}}{\rho}\right)-\left(\frac{W_{TO}}{P_b}\right)\frac{1}{2}\rho_{CR}\frac{V_{CR\,MAX}^3}{\eta_P}C_{D0\,CR}-\left(\frac{W_{TO}}{S}\right)^2\left(\frac{W_{TO}}{P_b}\right)\frac{2}{\rho_{CR}V_{CR\,MAX}\,\pi\,AR\,e\,\eta_P}=0 \qquad (119)$$

If, instead of the maximum cruise speed $V_{CR\,\mathrm{MAX}}$, the cruising speed V_{CR} is given as design requirement, it may be assumed that the maximum cruise speed is 20-30% greater than the cruise speed ($1.2V_{CR}$). In order to adapt the maximum cruise speed requirement with the DEP model implemented, the first step is to repeat the horizontal equilibrium equation in trim configuration with a different expression of the drag coefficient due to the DEP model:

$$\left(\frac{W_{TO}}{S}\right)\left(\frac{W_{TO}}{P_b}\right)^{-1}\left(\frac{\rho_{CR}}{\rho}\right)\frac{\eta_P}{V_{CR\,MAX}}=\frac{1}{2}\rho_{CR}V_{CR\,MAX}^2C_{D\,CR} \qquad (120)$$

It is possible to express the aerodynamic coefficients as the summation of the aerodynamic coefficients with unblown wing and the delta coefficients derived in the above section as function of the two variables of the SMP, including the trim vertical balance for cruise configuration:

$$\begin{cases} C_{L\,CR} = C_{L\,u\,CR} + \Delta C_{L\,CR}\left(\frac{W_{TO}}{S}, \frac{W_{TO}}{P_b}, N\right) = \frac{\left(\frac{W_{TO}}{S}\right)}{\frac{1}{2}\rho_{CR} V_{CR\,MAX}^2} \\ C_{D\,CR} = C_{D\,u\,CR} + \Delta C_{D\,CR}\left(\frac{W_{TO}}{S}, \frac{W_{TO}}{P_b}, N\right) \end{cases} \tag{121}$$

After some manipulations, it is possible to express the dependence of the drag coefficient in cruise configuration from the the unblown aerodynamic coefficient and the delta terms:

$$C_{D\,CR} = C_{D0\,u\,CR} + \frac{(C_{L\,u\,CR})^2}{\pi\, AR\, e} + \Delta C_{D0\,CR}\left(\frac{W_{TO}}{S}, \frac{W_{TO}}{P_b}, N\right) + \Delta C_{Di\,CR}\left(\frac{W_{TO}}{S}, \frac{W_{TO}}{P_b}, N\right) \tag{122}$$

Furthermore, it is possible to introduce the complete expression of the drag coefficient induced by the lift force due to the DEP model as

$$\Delta C_{Di\,CR} = \frac{\Delta C_{L\,CR}^2\left(\frac{W_{TO}}{S}, \frac{W_{TO}}{P_b}, N\right) + 2 C_{L\,u\,CR}\,\Delta C_{L\,CR}\left(\frac{W_{TO}}{S}, \frac{W_{TO}}{P_b}, N\right)}{\pi\, AR\, e} \tag{123}$$

In this way, the complete expression of the drag coefficient in cruise configuration can be summarized in the following equation:

$$\begin{cases} C_{D\,CR} = C_{D0\,u\,CR} + \frac{(C_{L\,CR})^2}{\pi\, AR\, e} + \Delta C_{D0\,CR}\left(\frac{W_{TO}}{S}, \frac{W_{TO}}{P_b}, N\right) \\ C_{L\,CR} = C_{L\,u\,CR} + \Delta C_{L\,CR}\left(\frac{W_{TO}}{S}, \frac{W_{TO}}{P_b}, N\right) = \frac{\left(\frac{W_{TO}}{S}\right)}{\frac{1}{2}\rho_{CR} V_{CR\,MAX}^2} \end{cases} \tag{124}$$

After the complete expression of the aerodynamic coefficients in cruise configuration, it is possible to return to the horizontal equilibrium equation in trim configuration, including the effect of the implemented DEP model:

$$\left(\frac{W_{TO}}{S}\right)\left(\frac{\rho_{CR}}{\rho}\right) - \left(\frac{W_{TO}}{P_b}\right)\frac{1}{2}\rho_{CR}\frac{V_{CR\,MAX}^3}{\eta_P}(C_{D\,CR}) = 0 \tag{125}$$

$$\left(\frac{W_{TO}}{S}\right)\left(\frac{\rho_{CR}}{\rho}\right) - \left(\frac{W_{TO}}{P_b}\right)\frac{1}{2}\rho_{CR}\frac{V_{CR\,MAX}^3}{\eta_P}\left(C_{D0\,u\,CR} + \frac{4\left(\frac{W_{TO}}{S}\right)^2}{\pi AR\, e \rho_{CR}{}^2 V_{CR\,MAX}^4} + \Delta C_{D\,0\,CR}\left(\frac{W_{TO}}{S}, \frac{W_{TO}}{P_b}, N\right)\right) = 0 \tag{126}$$

$$\left(\frac{W_{TO}}{S}\right)\left(\frac{\rho_{CR}}{\rho}\right) - \left(\frac{W_{TO}}{P_b}\right)\frac{1}{2}\rho_{CR}\frac{V_{CR\,MAX}^3}{\eta_P}C_{D0\,CR}{}^* - \left(\frac{W_{TO}}{S}\right)^2\left(\frac{W_{TO}}{P_b}\right)\frac{2}{\rho_{CR}V_{CR\,MAX}\,\pi\,AR\,e\,\eta_P} = 0 \qquad (127)$$

Where the parameter $C_{D0\,u\,CR}$* represents the total aircraft drag coefficient due to friction and dynamic pressure in cruise configuration, computed with the DEP model as

$$C_{D0\,CR}{}^* = C_{D0\,u\,CR} + \Delta C_{D0\,CR}\left(\frac{W_{TO}}{S}, \frac{W_{TO}}{P_b}, N\right) \qquad (128)$$

Equation 128 provides the third graph in the SMP, represented with the blue solid line in Figure 3.8 (left) and compared to the constraint relative to the conventional case represented with red solid line. In Figure 3.8 (right), it is possible to see the behaviour of the maximum cruise speed requirement with the increase of the number of propellers *N* along the DP array.

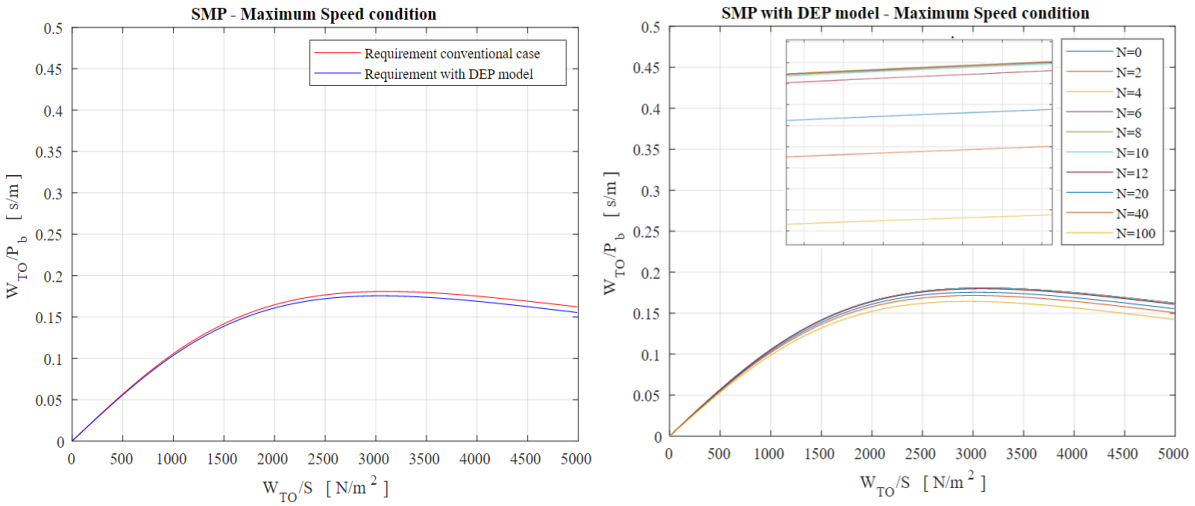

Figure 3.8: Maximum cruise speed contribution in constructing the SMP with DEP model.

The maximum cruise speed requirement tends to decrease slightly the acceptable region for the determination of the design point with the increase of the number of propellers *N* used for the DEP, generating a small penalty in the selection of the design point.

In the conventional case, the wing sizing based on maximum cruise speed requirement is represented as the variations of power loading versus wing loading. The maximum cruise speed requirement derived with DEP model fits perfectly with the hyperbolic curve of the conventional case when it is considered *N* equal to zero (without DEP system), confirming the accuracy of the procedure.

In order to determine the acceptable region, it is necessary to find what side of the above graphs is satisfying the maximum speed requirement. As the value of $V_{CR\,MAX}$ is increased, the value of power loading is decreased. Since any value of $V_{CR\,MAX}$ greater than the specified maximum speed is satisfying the maximum speed requirement, so the region below the graph is acceptable.

3.3.4 Rate of climb

The rate of climb is defined as the aircraft speed along the vertical axis or the vertical component of the aircraft airspeed. Hence, the ROC is about how fast an aircraft gains height. The standard requirement for a preliminary design phase is presented in Roskam [28] in the conventional case. This equation is valid both for aircraft certificated with CS Part 23 and for aircraft certificated with CS Part 25 in the case of propeller-drive aircraft. The recommended minimum ROC is of 1.524 m/s with All Engines Operative (AEO).
The rate of climb equation is developed starting from the basic equation for climb equilibrium referred to propeller-driven aircraft:

$$\begin{cases} \eta_P \left(\frac{P_b}{W_{TO}}\right) = ROC + V_1 \left(\frac{C_{L\,1}}{C_{D\,1}}\right) \\ ROC = V_1 \sin(\gamma) \end{cases} \tag{129}$$

The velocity V_1 is the climb speed, the angle γ is the flight path angle and the aerodynamic coefficients $C_{L\,1}$ and $C_{D\,1}$ are the aerodynamic coefficients in climb configuration. It is possible to express the climb speed and the aerodynamic coefficients in the maximum ROC condition with the following equations:

$$\begin{cases} V_1|_{ROC\ MAX} = \sqrt{\dfrac{2\left(\frac{W_{TO}}{S}\right)}{\rho_1 \sqrt{\frac{3C_{D0\,1}}{K}}}} \\ C_{L\,1}|_{ROC\ MAX} = \sqrt{\dfrac{3C_{D0\,1}}{K}} \\ C_{D\,1}|_{ROC\ MAX} = 4\,C_{D0\,1} \end{cases} \tag{130}$$

The parameter K is the induced drag factor. After the substitution of the new terms in the basic equation for climb equilibrium, it is possible to obtain the rate of climb requirement for propeller-driven aircraft in the conventional case, highlighting the dependence from the wing loading and the power loading:

$$\left(\frac{W_{TO}}{P_b}\right) - \frac{\eta_P}{ROC + \dfrac{\left(\frac{W_{TO}}{S}\right)^{\frac{1}{2}}}{\left(\frac{\rho_1}{\rho_0}\right)^{\frac{1}{2}} \dfrac{(AR\,e)^{\frac{3}{4}}}{(C_{D0\,1})^{\frac{1}{4}}}} \left[\frac{4\sqrt{2}}{(3\pi)^{\frac{3}{4}}(\rho_0)^{\frac{1}{2}}}\right]} = 0 \tag{131}$$

It is possible to assemble the constant terms in the above equation in order to express the rate of climb requirement in a clearer expression as

$$\left(\frac{W_{TO}}{P_b}\right) - \frac{\eta_P}{ROC + \frac{\left(\frac{W_{TO}}{S}\right)^{\frac{1}{2}}}{\left(\frac{\rho_1}{\rho_0}\right)^{\frac{1}{2}} \frac{(AR\ e)^{\frac{3}{4}}}{(C_{D0\ 1})^{\frac{1}{4}}}} 0.95017} = 0 \tag{132}$$

Since the ROC is in the denominator, as the value of ROC is increased, the value of power loading W_{TO}/P_b will drop. For this reason, the rate of climb equation is evaluated at ROC_{MAX} in order to have a more restrictive rate of climb constraint.

In order to adapt the rate of climb requirement with the DEP model implemented, it is possible to express the climb speed and the aerodynamic coefficients in climb configuration as the summation of the aerodynamic coefficients with unblown wing and the delta coefficients derived in the above section as function of the two variables of the SMP:

$$\begin{cases} V_1|_{ROC\ MAX} = \sqrt{\dfrac{2\left(\frac{W_{TO}}{S}\right)}{\rho_1 \sqrt{\dfrac{3\left(C_{D0\,u\,1} + \Delta C_{D0\,1}\left(\frac{W_{TO}}{S}, \frac{W_{TO}}{P_b}, N\right)\right)}{K}}}} \\ C_{L\,1}|_{ROC\ MAX} = \sqrt{\dfrac{3\left(C_{D0\,u\,1} + \Delta C_{D0\,1}\left(\frac{W_{TO}}{S}, \frac{W_{TO}}{P_b}, N\right)\right)}{K}} \\ C_{D\,1}|_{ROC\ MAX} = 4\left(C_{D0\,u\,1} + \Delta C_{D0\,1}\left(\frac{W_{TO}}{S}, \frac{W_{TO}}{P_b}, N\right)\right) \end{cases} \tag{133}$$

The term $C_{D0\,u1}$ represents the aircraft drag coefficient due to friction and dynamic pressure in climb configuration in the unblown wing case. The complete rate of climb requirement for aircraft with DEP system can be expressed for a preliminary sizing phase with the following equation:

$$\left(\frac{W_{TO}}{P_b}\right) - \frac{\eta_P}{ROC + \frac{\left(\frac{W_{TO}}{S}\right)^{\frac{1}{2}}}{\left(\frac{\rho_1}{\rho_0}\right)^{\frac{1}{2}} \frac{(AR\ e)^{\frac{3}{4}}}{\left(C_{D0\,u\,1} + \Delta C_{D0\,1}\left(\frac{W_{TO}}{S}, \frac{W_{TO}}{P_b}, N\right)\right)^{\frac{1}{4}}}} 0.95017} = 0 \tag{134}$$

The delta coefficient depends on the climb speed, which is expressed as a function of the wing loading and the drag coefficient due to friction and dynamic pressure in climb configuration. This requirement provides the fourth graph in the SMP with DEP model, represented with the blue solid line in Figure 3.9 (left) and compared to the conventional case represented with the red solid line. In Figure 3.9 (right), it is possible to see the behaviour of the rate of climb requirement with the increase of the number of propellers N along the DP array.

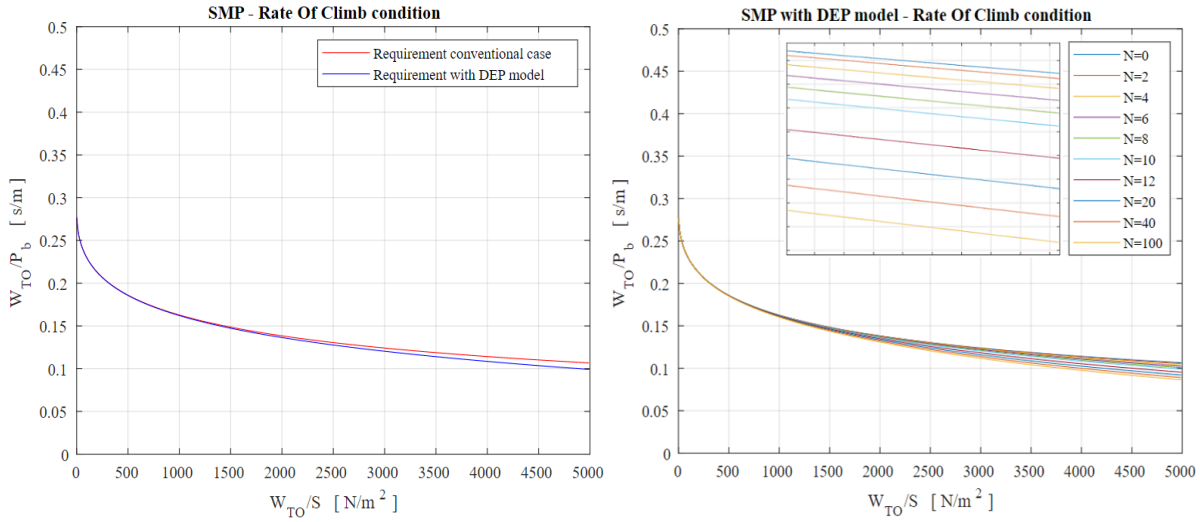

Figure 3.9: Rate of climb contribution in constructing the SMP with DEP model.

The rate of climb requirement tends to decrease slightly the acceptable region for the determination of the design point with the increase of the number of propellers *N* used for the DEP, generating a little penalty in the development of the acceptable region. In the conventional case, the wing sizing based on rate of climb requirement is represented as the variations of power loading versus wing loading.
In order to compare the conventional case and the SMP with DEP model, it is possible to see that both the constraints have a hyperbolic behaviour with similar shape and slope, even if the constraint with DEP model is slightly more restrictive for increasing values of power loading. In the right plot it is possible to see that the rate of climb requirement derived with DEP model fits perfectly with the hyperbolic curve of the conventional unblown case when it is considered *N* equal to zero (without DEP system), confirming the accuracy of the procedure.
We note that the ROC is in the denominator; hence, as the value of ROC is increased, the value of power loading will drop. Since any value of ROC greater than the specified ROC is satisfying the climb requirement, so the region below the graph is acceptable.

3.3.5 Climb Gradient

The climb gradient is defined as the ratio of the increase of altitude to horizontal air distance expressed as a percentage, therefore a still air distance. It represents the percentage of the rise over run that the considered aircraft is climbing at and it is symbolized with the acronym CGR. The standard requirement for a preliminary design phase is presented in Roskam [28] in the conventional case. This equation is valid both for aircraft certificated with CS Part 23 and for aircraft certificated with CS Part 25 in the case of propeller-drive aircraft.
The climb gradient equation is developed starting from the basic equation for climb equilibrium referred to propeller-driven aircraft:

$$\begin{cases} \eta_P \left(\frac{P_b}{W_{TO}}\right) = V_1 \left[\text{CGR} + \left(\frac{C_{L\,1}}{C_{D\,1}}\right)\right] \\ CGR = \sin(\gamma) \end{cases} \tag{135}$$

The velocity V_1 is the climb speed, the angle γ is the flight path angle and the aerodynamic coefficients $C_{L\,1}$ and $C_{D\,1}$ are the aerodynamic coefficients in climb configuration. It is possible to express the climb speed as function of the lift coefficient in climb configuration using the vertical equilibrium equation as

$$V_1 = \sqrt{\frac{2\left(\frac{W_{TO}}{S}\right)}{\rho_1 C_{L\,1}}} \tag{136}$$

After the substitution of this term in the basic equation for climb equilibrium, it is possible to obtain the climb gradient requirement for propeller-driven aircraft in the conventional case, highlighting the dependence from the wing loading and the power loading:

$$\left(\frac{W_{TO}}{P_b}\right) - \frac{\eta_P \left(\frac{\rho_1}{\rho_0}\right)^{\frac{1}{2}} (C_{L\,1})^{\frac{1}{2}}}{\left(\frac{W_{TO}}{S}\right)^{\frac{1}{2}} \left[\text{CGR} + \left(\frac{C_{D\,1}}{C_{L\,1}}\right)\right] \frac{\sqrt{2}}{(\rho_0)^{\frac{1}{2}}}} = 0 \tag{137}$$

It is possible to assemble the constant terms in the above equation in order to express the climb gradient requirement in a clearer expression as

$$\left(\frac{W_{TO}}{P_b}\right) - \frac{\eta_P \left(\frac{\rho_1}{\rho_0}\right)^{\frac{1}{2}} (C_{L\,1})^{\frac{1}{2}}}{\left(\frac{W_{TO}}{S}\right)^{\frac{1}{2}} \left[\text{CGR} + \left(\frac{C_{D\,1}}{C_{L\,1}}\right)\right] 1.2777} = 0 \tag{138}$$

Since the CGR is in the denominator, as the value of CGR is increased, the value of power loading W_{TO}/P_b will drop. For this reason, climb gradient equation is evaluated at maximum flight path angle in order to have a more restrictive climb gradient constraint.

In order to adapt the climb gradient requirement with the DEP model implemented, it is possible to express the climb speed and the aerodynamic coefficients in climb configuration as the summation of the aerodynamic coefficients with unblown wing and the delta coefficients derived in the above section as function of the two variables of the SMP:

$$\begin{cases} V_1 = \sqrt{\dfrac{2\left(\dfrac{W_{TO}}{S}\right)}{\rho_1 C_{L\,1}}} \\ C_{L\,1} = C_{L\,u\,1} + \Delta C_{L\,1}\left(\dfrac{W_{TO}}{S}, \dfrac{W_{TO}}{P_b}, N\right) \\ C_{D\,1} = C_{D0\,u\,1} + \dfrac{(C_{L\,u\,1})^2}{\pi\, AR\, e} + \Delta C_{D\,1}\left(\dfrac{W_{TO}}{S}, \dfrac{W_{TO}}{P_b}, N\right) \end{cases} \tag{139}$$

The complete climb gradient requirement for aircraft with DEP system is expressed for a preliminary sizing phase with the following equation:

$$\left(\frac{W_{TO}}{P_b}\right) - \frac{\eta_P \left(\dfrac{\rho_1}{\rho_0}\right)^{\frac{1}{2}} \left(C_{L\,u\,1} + \Delta C_{L\,1}\left(\dfrac{W_{TO}}{S}, \dfrac{W_{TO}}{P_b}, N\right)\right)^{\frac{1}{2}}}{\left(\dfrac{W_{TO}}{S}\right)^{\frac{1}{2}} \left[\mathrm{CGR} + \left(\dfrac{C_{D0\,u\,1} + \dfrac{(C_{L\,u\,1})^2}{\pi\, AR\, e} + \Delta C_{D\,1}\left(\dfrac{W_{TO}}{S}, \dfrac{W_{TO}}{P_b}, N\right)}{C_{L\,u\,1} + \Delta C_{L\,1}\left(\dfrac{W_{TO}}{S}, \dfrac{W_{TO}}{P_b}, N\right)}\right)\right] 1.2777} = 0 \tag{140}$$

The delta coefficient depends on the climb speed, which is expressed as the function of the wing loading and the lift coefficient in climb configuration. This requirement provides the fifth graph in the SMP with DEP model, represented with the blue solid line in Figure 3.10 (left) and compared to the conventional case represented with the red solid line. In Figure 3.10 (right), it is possible to see the behaviour of the climb gradient requirement with the increase of the number of propellers *N* along the DP array.

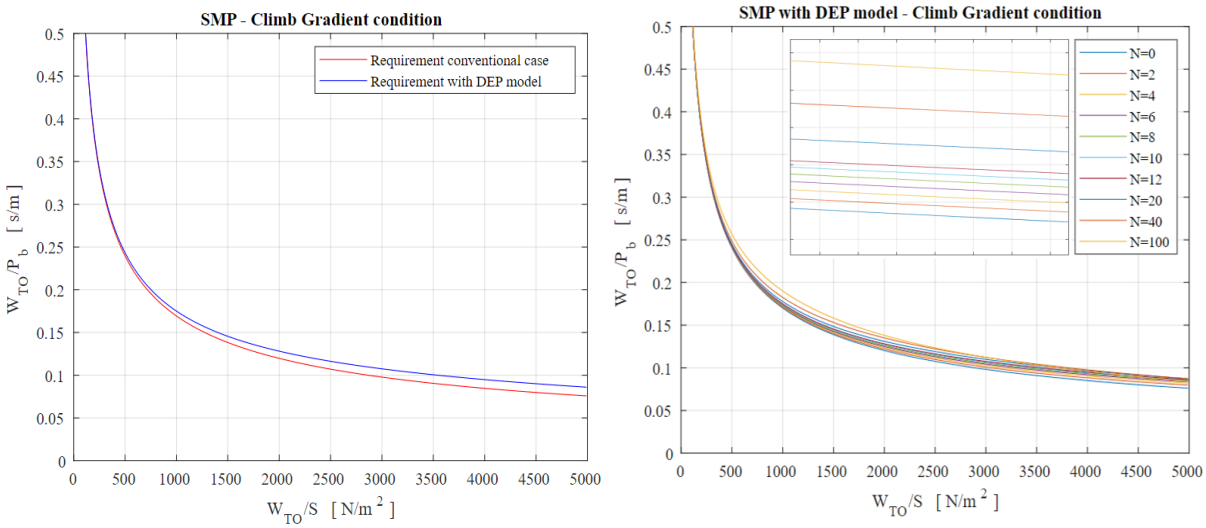

Figure 3.10: Rate of climb contribution in constructing the SMP with DEP model.

The climb gradient requirement tends to increase slightly the acceptable region for the determination of the design point with the increase of the number of propellers *N* used for the DEP, generating a little advantage in the development of the acceptable region. In the conventional case, the wing sizing based on climb gradient requirement is represented as the variations of power loading versus wing loading.

In order to compare the conventional case and the SMP with DEP model, it is possible to see that both the constraints have a hyperbolic behaviour with similar shape and slope, even if the constraint with DEP model is slightly less restrictive for increasing values of power loading. In the right plot it is possible to see that the climb gradient requirement derived with DEP model fits perfectly with the hyperbolic curve of the conventional unblown case when it is considered *N* equal to zero (without DEP system), confirming the accuracy of the procedure.
We note that the CGR is in the denominator; hence, as the value of CGR is increased, the value of power loading will drop. Since any value of CGR greater than the specified CGR is satisfying the climb requirement, so the region below the graph is acceptable.

3.3.6 Ceiling

Another performance requirement that influencing the wing and engine sizing is the ceiling. The ceiling is defined as the highest altitude that an aircraft can safely have a straight level flight. Another definition is the highest altitude that an aircraft can reach by its own engine and have sustained flight. For many aircraft, the ceiling is not a crucial requirement, but for others such as the reconnaissance aircraft SR-71 Black Bird, a ceiling of about 19,812 m is the most difficult performance requirement to meet. This design requirement made the designers design and invent a special engine for this mission.
In general, there are four definitions of ceiling:

1. Absolute ceiling h_{AC}. As the name implies, the absolute ceiling is the absolute maximum altitude that an aircraft can ever maintain level flight. In other terms, the absolute ceiling is the altitude at which the ROC_{AC} is zero.
2. Service ceiling $h_{SC.}$ The service ceiling is defined as the highest altitude at which the aircraft can climb with a ROC_{SC} of 0.5 m/s. The service ceiling is lower than the absolute ceiling.
3. Cruise ceiling h_{CRC}. The cruise ceiling is defined as the altitude at which the aircraft can climb with a ROC_{CRC} of 1.5 m/s. The cruise ceiling is lower than the service ceiling.
4. Combat ceiling h_{CC}. The combat ceiling is defined as the altitude at which a fighter can climb with a ROC_{CC} of 5 m/s. The combat ceiling is lower than the cruise ceiling. This ceiling is defined only for fighter aircraft.

The standard requirement for a preliminary design phase is presented in Roskam [28] in the conventional case. The equation is valid for both aircraft certificated with CS Part 23 and aircraft certificated with CS Part 25 in the case of propeller-drive aircraft. The rate of climb equation can also be applied to the ceiling altitude requirement, starting from the basic equation for climb equilibrium referred to propeller-driven aircraft:

$$\left(\frac{W_{TO}}{P_C}\right) - \frac{\eta_P}{ROC_C + \frac{\left(\frac{W_{TO}}{S}\right)^{\frac{1}{2}}}{\left(\frac{\rho_C}{\rho_0}\right)^{\frac{1}{2}} \frac{(AR\ e)^{\frac{3}{4}}}{(C_{D0\,1})^{\frac{1}{4}}}}\ 0.95017} = 0 \tag{141}$$

The parameter ROC_C is the ROC at ceiling, ρ_C is the air density at ceiling and P_C is the engine maximum thrust at ceiling. In contrast, the engine power is a function of altitude, or air density. The exact relationship depends upon the engine type, engine technology, engine installation, and airspeed. Following [26], at this moment of the design phase, when the aircraft is not completely designed, the following approximate relationship can be utilized:

$$P_C = P_b \left(\frac{\rho_C}{\rho_0}\right) \tag{142}$$

After the substitution of the new terms in the basic equation for climb equilibrium, it is possible to obtain the ceiling requirement for propeller-driven aircraft in the conventional case, highlighting the dependence from the wing loading and the power loading:

$$\left(\frac{W_{TO}}{P_b}\right) - \frac{\eta_P \left(\frac{\rho_C}{\rho_0}\right)}{ROC_C + \frac{\left(\frac{W_{TO}}{S}\right)^{\frac{1}{2}}}{\left(\frac{\rho_C}{\rho_0}\right)^{\frac{1}{2}} \frac{(AR\ e)^{\frac{3}{4}}}{(C_{D0\,1})^{\frac{1}{4}}}} 0.95017} = 0 \tag{143}$$

The ceiling requirement needs to be evaluated for all the first three types of ceiling in the preliminary design phase of all aircraft and it is necessary to consider also the combat ceiling requirement for fighter aircraft. Since the ROC is in the denominator, as the value of ROC is increased, the value of power loading W_{TO}/P_b will drop. The ceiling equation is evaluated at fixed values of ROC defined for the four different types of ceiling previously explained.

In order to adapt the ceiling requirement with the DEP model implemented, it is possible to express the climb speed and the aerodynamic coefficients in climb configuration as the summation of the aerodynamic coefficients with unblown wing and the delta coefficients derived in the above section as function of the two variables of the SMP. The complete ceiling requirement for aircraft with DEP system can be expressed for a preliminary sizing phase with the following equation:

$$\left(\frac{W_{TO}}{P_b}\right) - \frac{\eta_P \left(\frac{\rho_C}{\rho_0}\right)}{ROC_C + \frac{\left(\frac{W_{TO}}{S}\right)^{\frac{1}{2}}}{\left(\frac{\rho_C}{\rho_0}\right)^{\frac{1}{2}} \frac{(AR\ e)^{\frac{3}{4}}}{\left(C_{D0\,u\,1} + \Delta C_{D0\,1}\left(\frac{W_{TO}}{S}, \frac{W_{TO}}{P_b}, N\right)\right)^{\frac{1}{4}}}} 0.95017} = 0 \tag{144}$$

The delta coefficient also depends on the climb speed, which is expressed as function of the wing loading and the aerodynamic coefficient in climb configuration, as for the rate of climb requirement. This requirement provides the sixth graph in the SMP with DEP model, represented with the dotted line in

Figure 3.11 (left) and compared to the conventional case represented with the solid line. The requirement is showed for each of the four types of ceiling previously described, using the red colour for absolute ceiling, the blue colour for service ceiling, the green colour for cruise ceiling and the black colour for combat ceiling. In Figure 3.11 (right), it is possible to see the behaviour of the service ceiling requirement with the increase of the number of propellers *N* along the DP array.

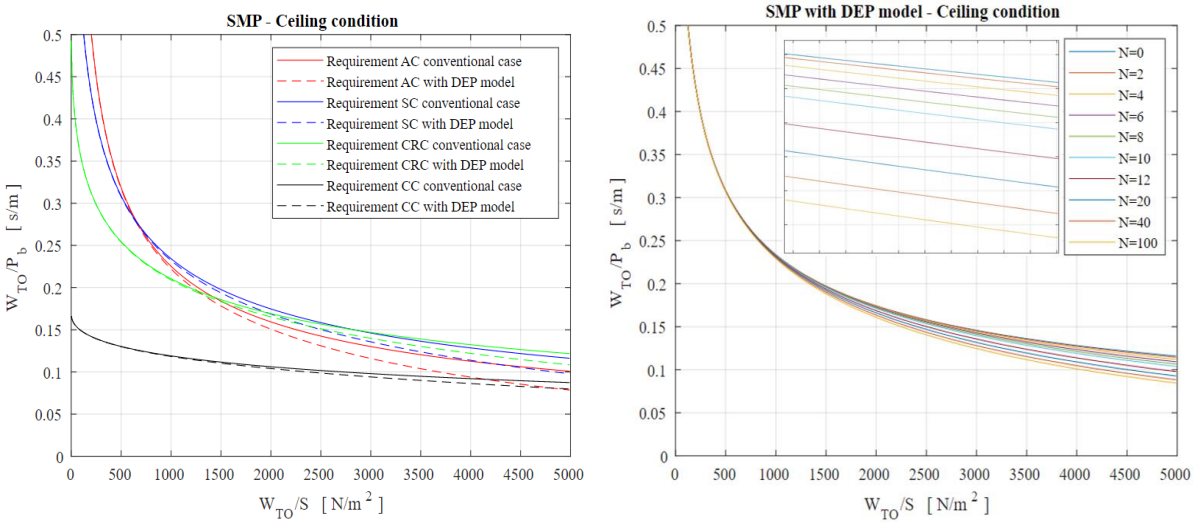

Figure 3.11: Rate of climb contribution in constructing the SMP with DEP model.

The ceiling requirement tends to decrease slightly the acceptable region for the determination of the design point with the increase of the number of propellers *N* used for the DEP, generating a little penalty in the development of the acceptable region. In the conventional case, the wing sizing based on ceiling requirement is represented as the variations of power loading versus wing loading. In order to compare the conventional case and the SMP with DEP model, it is possible to see that both the constraints have a hyperbolic behaviour with similar shape and slope, even if the constraint with DEP model is slightly more restrictive for increasing values of power loading. In the right plot it is possible to see that the service ceiling requirement derived with DEP model fits perfectly with the hyperbolic curve of the conventional unblown case when it is considered *N* equal to zero (without DEP system), confirming the accuracy of the procedure.
We note that the ROC is in the denominator; hence, as the value of ROC is increased, the value of power loading will drop. Since any value of ROC greater than the specified ROC is satisfying the climb requirement, the region below the graph is acceptable.

3.3.7 Landing Distance

The total landing distance S_L is the distance used in landing and braking to a complete stop after crossing the runway threshold at 15.24 m (50 ft). The landing distance requirement is a limit which depends on the landing weight, the approach speed, the deceleration method used, the flying qualities

of the airplane and the pilot technique. The landing ground run S_{LG} showed in Figure 3.12 is the length of runway available and suitable for the ground run of an airplane landing.

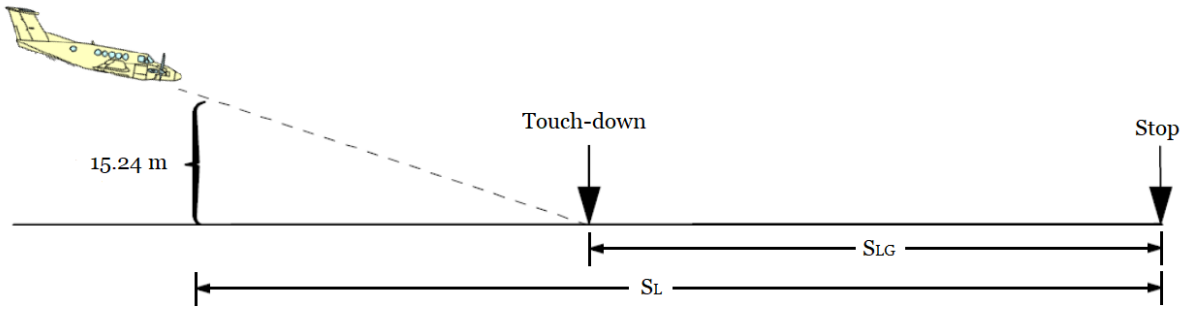

Figure 3.12: The definition of landing distance.

For aircraft certificated with CS Part 23 the obstacle height is 15.24 m (50 ft) and the standard requirement for a preliminary design phase is presented in Roskam [28] for the conventional case propeller-driven aircraft. The parameter θ represents the typical value for landing weight to take-off weight ratio.
Following [28], there is an empirical relation between the stall speed and the total landing distance, based on experimental data taken from airplanes certificated with CS Part 23:

$$V_S^2 = \frac{S_L}{0.59153} \tag{145}$$

The landing distance equation represents a limit to the minimum allowable speed in the landing configuration because the range of acceptable speed is between the stall speed and the maximum speed. This equation is developed from the vertical equilibrium equation, dividing both sides by the wing surface and considering the parameter k_W, which is the landing weight to take-off weight ratio:

$$\left(\frac{W_{TO}}{S}\right) k_W - \frac{1}{2}\rho\left(\frac{S_L}{0.59153}\right) C_{L\,MAX\,L} = 0 \tag{146}$$

For aircraft certificated with CS Part 25 the obstacle height is 15.24 m (50 ft) and the standard requirement for a preliminary design phase is presented in Roskam's "Airplane Design Part 1: Preliminary Sizing of Airplanes" [28] for conventional case propeller-driven aircraft. The landing field length is defined as the distance between the standard obstacle to the final stop point, divided by 0.6. Following the reference [28], there is an empirical relation between the stall speed and the total landing distance, based on experimental data taken from airplanes certificated with CS Part 25:

$$V_S^2 = \frac{S_L}{0.35036} \tag{147}$$

The landing distance equation represents a limit to the minimum allowable speed in landing configuration because the range of acceptable speed is between the stall speed and the maximum speed. This equation is developed from the vertical equilibrium equation, dividing both sides by the wing surface:

$$\left(\frac{W_{TO}}{S}\right) k_W - \frac{1}{2}\rho\left(\frac{S_L}{0.35036}\right) C_{L\,MAX\,L} = 0 \tag{148}$$

Since there are not historical regression data between the landing parameters and the landing stall speed for electric aircraft with DEP system, Roskam's expression of the landing distance requirement is useless in this case. It is possible to evaluate this requirement for electric aircraft with DEP model following the description presented in Sadraey's "Aircraft Performance - An engineering approach" [31]. Following this approach, five forces work in a ground roll: aircraft weight, lift force, drag force, brake force and friction force.
Based on Newton's second law, the summation of all forces generates a deceleration on the aircraft as follows,

$$-D - F_f - F_B = m_L a \tag{149}$$

In the above equation the acceleration a has a negative value (so, deceleration), the parameter m_L represents the aircraft mass in landing configuration, the force F_f is the friction force, the force F_B is the brake force and D is the aircraft drag. Since the Newton's second law is referred to the ground roll segment, forces act without the presence of the DEP system and the thrust is arrested during ground phase. All forces during landing can be expressed with the following equations:

$$\begin{cases} F_f = \mu\,(W_L - L_L) = \mu\left(W_L - \frac{1}{2}\rho_0 V^2 S C_{L\,u\,L}\right) \\ F_B = \mu_B\, W_L \\ D = \frac{1}{2}\rho_0 V^2 S C_{D\,u\,L} \end{cases} \tag{150}$$

The friction force is proportional to the normal component which is the algebraic sum of the aircraft weight and aerodynamic lift. The proportionality coefficient μ is static rolling friction coefficient and the parameter μ_B is the brake coefficient, with a typical value of 0.1-0.5 for deceleration. Aerodynamic coefficients $C_{L\,u\,L}$ and $C_{D\,u\,L}$ are referred to landing ground configuration without the presence of the DEP system (unblown wing) and the deceleration during ground roll section can be expressed in this way as

$$a = -\frac{D + F_f + F_B}{m_L} \tag{151}$$

Defining the velocity as the rate of change of displacement with time, the ground roll section S_{LG} can be determined integrating the ratio between the velocity and the deceleration during ground phase:

$$S_{LG} = \int_{V_L}^{0} \frac{V}{a} dV = \int_{V_L}^{0} -\frac{m_L V}{D + F_f + F_B} dV = \int_{0}^{V_L} \frac{m_L V}{D + F_f + F_B} dV \tag{152}$$

Considering the complete expressions of the drag force, the brake force and the friction force, the dependence from velocity can be highlighted in the integral with the following procedure:

$$S_{LG} = \int_{0}^{V_L} \frac{m_L V}{\mu\, W_L + \mu_B\, W_L + \frac{1}{2}\rho_0 V^2 S(C_{D\,u\,L} - \mu C_{L\,u\,L})} dV = \int_{0}^{V_L} \frac{V}{A + BV^2} dV \tag{153}$$

This integration can be directly solved using a mathematical approach, after splitting terms in two parameters A and B, with the following solution:

$$\begin{cases} S_{LG} = \dfrac{1}{2B} \ln\left(\dfrac{A + BV_L^2}{A}\right) \\ A = \mu\, g + \mu_B\, g \\ B = \dfrac{1}{2}\dfrac{\rho_0 S}{m_L}(C_{D\,u\,L} - \mu C_{L\,u\,L}) \end{cases} \tag{154}$$

When A and B are substituted in the complete expression, we have the new formula for the ground roll section:

$$S_{LG} = \frac{k_W \left(\frac{W_{TO}}{S}\right)}{g\rho_0 (C_{D\,u\,L} - \mu C_{L\,u\,L})} \ln\left[\frac{\mu + \mu_B + \frac{1}{2}\rho_0 \left(\frac{S}{W_L}\right) V_L^2 (C_{D\,u\,L} - \mu C_{L\,u\,L})}{\mu + \mu_B}\right] \tag{155}$$

The parameter k_W represents the landing weight to take-off weight ratio and the landing speed V_L can be expressed with the vertical equilibrium equation during airborne landing phase:

$$\begin{cases} V_L^2 = \left(\dfrac{W_L}{S}\right)\dfrac{2}{\rho_0 C_{L\,L}} \\ C_{L\,L} = C_{L\,u\,L} + + \Delta C_{L\,L}\left(\dfrac{W_{TO}}{S}, \dfrac{W_{TO}}{P_b}, N\right) \end{cases} \tag{156}$$

Where $C_{L\,L}$ is the aircraft lift coefficient during landing configuration and $\Delta C_{L\,L}$ is the lift increment due to the DEP system, computed with the DEP model implemented. The final expression of the ground roll section for aircraft with DEP system is obtained as

$$S_{LG} = \frac{k_W \left(\frac{W_{TO}}{S}\right)}{g\rho_0 (C_{D\,u\,L} - \mu C_{L\,u\,L})} \ln \left[\frac{\mu + \mu_B + \left(\frac{C_{D\,u\,L} - \mu C_{L\,u\,L}}{C_{L\,u\,L} + + \Delta C_{L\,L} \left(\frac{W_{TO}}{S}, \frac{W_{TO}}{P_b}, N \right)} \right)}{\mu + \mu_B} \right] \tag{157}$$

Considering Roskam's simplification during landing phase [28], the total landing distance S_L is related to the corresponding landing ground run S_{LG} and the landing distance requirement for aircraft with DEP system can be expressed for a preliminary design phase with the following equation:

$$S_L - \frac{1.938\, k_W \left(\frac{W_{TO}}{S}\right)}{g\rho_0 (C_{D\,u\,L} - \mu C_{L\,u\,L})} \ln \left[\frac{\mu + \mu_B + \left(\frac{C_{D\,u\,L} - \mu C_{L\,u\,L}}{C_{L\,u\,L} + + \Delta C_{L\,L} \left(\frac{W_{TO}}{S}, \frac{W_{TO}}{P_b}, N \right)} \right)}{\mu + \mu_B} \right] = 0 \tag{158}$$

The delta coefficient depends also by the landing speed, which is expressed as function of the wing loading and the lift coefficient in landing configuration with the vertical equilibrium equation. This requirement provides the seventh graph in the SMP with DEP model, represented with the blue solid line in Figure 3.13 (left) and compared to the conventional case represented with the red solid vertical line. In Figure 3.13 (right), it is possible to see the behaviour of the landing distance requirement with the increase of the number of propellers *N* along the DP array.

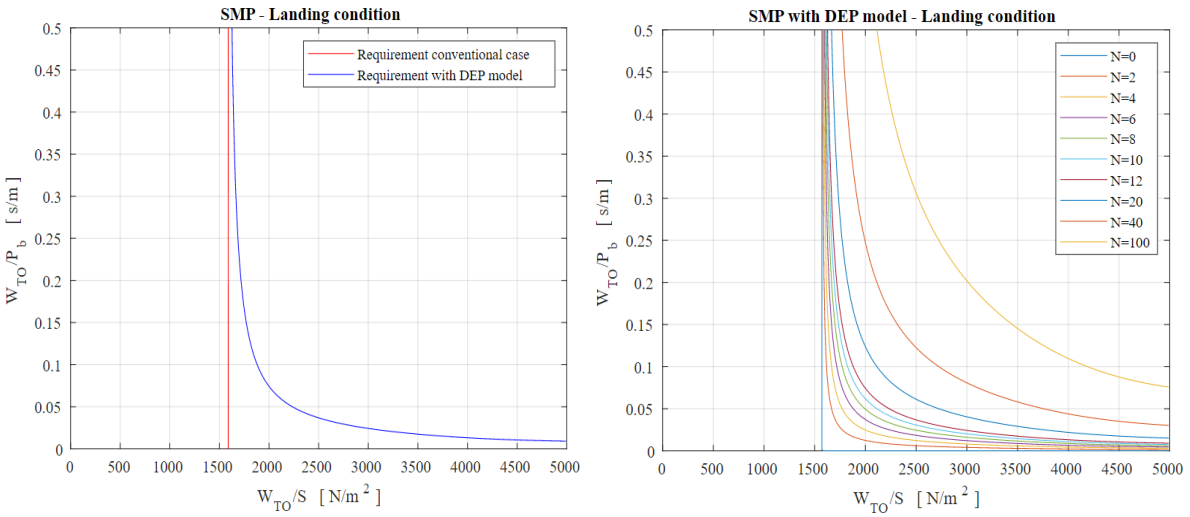

Figure 3.13: Landing distance contribution in constructing the SMP with DEP model.

The landing distance requirement tends to increase the acceptable region for the determination of the design point with the increase of the number of propellers N used for the DEP, generating a great advantage in the development of the preliminary design phase.
In the conventional case, the wing sizing based on landing distance requirement is represented as the variations of wing loading versus stall speed. As can be seen from the above figure, the power loading W_{TO}/P_b does not contribute to wing loading in this case. In other words, the wing loading to satisfy the landing distance requirements is not a function of power loading in the conventional case while the landing distance equation depends also by the power loading in the case with DEP model. Therefore, it is possible to see that the graph of power loading versus wing loading is a vertical line in the conventional case while it becomes a hyperbolic curve in the case with DEP model. Making a comparison between the conventional case and the SMP with DEP model, the landing distance requirement derived with DEP model fits perfectly with the vertical line of the conventional unblown case when considering N equal to zero (without DEP system), confirming the accuracy of the procedure.
From theory, any stall speed less than the stall speed computed with its relation to the total landing distance is acceptable. Therefore, the left side of graph is an acceptable region and on the right side, the landing distance requirements is not met.

3.4 Design Example: NASA X-57 Maxwell

The NASA X-57 Maxwell is the reference aircraft for the following analysis. This DEP airplane has a design point with a wing loading W_{TO}/S of 2154.6 N/m² and a power loading W_{TO}/P_b of 0.0542 s/m. Since this airplane is still under development, a flight test manual that contains all information for the wing and engine sizing si not available. Therefore, most of the needed data are taken from NASA's technical papers [1, 16, 17, 18, 19, 25, 27]. Some performance data are not published for the referred aircraft because of its recent development so they have been taken from the Tecnam P2006T technical papers [23, 24], considering the similarities between the two types of aircraft.
The SMP is developed with both the new preliminary design technique (with the DEP model) and the standard technique for propeller-driven aircraft, in order to validate the new formulation implemented. After the validation's phase, the SMP of the X-57 Maxwell aircraft is also showed without the DEP system. In this way, it is possible to highlight the improvement of distributed high-lift propellers in preliminary sizing phase. In table 3.2, it is possible to find all input data used for the implementation of the equation for each performance requirement. Numeric value followed by an asterisk indicates datum taken from Tecnam P2006T technical papers [23, 24].

Geometric Input Data		
Data symbols	Numeric values	Units
χ	0.5	–
N	12	–
AR	15	–
b_e/b	0.873	–
x/c	0.31	–
x/R	0.6905	–
$\Lambda_{c/2}$	1.9	deg
φ	0	deg
α_{twist}	0	deg
e	0.8	–
c_f	0.009	–

Table 3.2: Geometric input data for SMP referred to NASA X-57 Maxwell aircraft.

In Tables from 3.3 to 3.9 the input data for the analysis of aircraft performance requirements are grouped together, referred to the NASA X-57 Maxwell aircraft.

Stall Speed		
Data symbols	Numeric values	Units
h_s	0	m
V_s	29.83	m/s
η_P	0.7	–

Table 3.3: Stall speed data for SMP referred to NASA X-57 Maxwell aircraft.

Take-off Run		
Data symbols	Numeric values	Units
h_{TO}	0	m
η_P	0.7	–
S_{TOG}	301 *	m
S_{TO}	394 *	m
μ	0.04	–

Table 3.4: Take-off run data for SMP referred to NASA X-57 Maxwell aircraft.

Maximum Cruise Speed		
Data symbols	Numeric values	Units
h_{CR}	2438.4	m
V_{CR}	77.16	m/s
$V_{CR\,MAX}$	92.6	m/s
η_P	0.8	—

Table 3.5: Maximum cruise speed data for SMP referred to NASA X-57 Maxwell aircraft.

Rate Of Climb		
Data symbols	Numeric values	Units
h_1	1524	m
η_P	0.7	—
ROC_{MAX}	3.2	m/s
ROC	1.524	m/s

Table 3.6: Rate of climb data for SMP referred to NASA X-57 Maxwell aircraft.

Climb Gradient		
Data symbols	Numeric values	Units
h_1	1524	m
η_P	0.7	—
CGR	0.083	—

Table 3.7: Climb gradient data for SMP referred to NASA X-57 Maxwell aircraft.

Ceiling		
Data symbols	Numeric values	Units
h_{AC}	4267.2	m
h_{SC}	3000	m
h_{CRC}	2438.4	m
η_P	0.7	—
ROC_{AC}	0	m/s
ROC_{SC}	0.5	m/s
ROC_{CRC}	1.5	m/s

Table 3.8: Ceiling data for SMP referred to NASA X-57 Maxwell aircraft.

Landing Distance		
Data symbols	Numeric values	Units
h_{LND}	0	m
η_P	0.7	–
S_L	349 *	m
S_{LG}	231 *	m
μ	0.05	–
μ_B	0.3	–
k_W	1	–

Table 3.9: Landing distance data for SMP referred to NASA X-57 Maxwell aircraft.

For greater clarity, the conventional sizing matrix plot for the NASA X-57 Maxwell aircraft is showed. This diagram is obtained using Roskam's conventional performance requirements [28] relative to airplanes certificated with CS Part 23 expect for take-off run requirement and landing distance requirement. For these two requirements, the procedure implemented in Sadraey [31] is preferred to avoid historical regression data referred to twin-engine propeller aircraft. The final sizing matrix plot is presented in Figure 3.14.

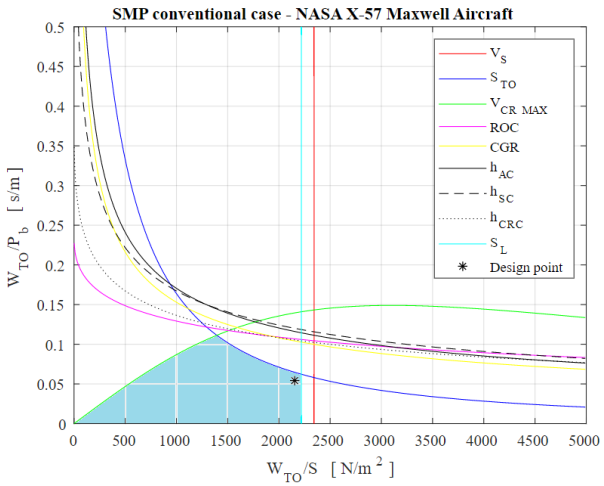

Figure 3.14: SMP with conventional case for NASA X-57 Maxwell aircraft.

During the initial phase of an aircraft project equipped with the DEP system, we are not able to compute exactly the effect of the high-lift propellers in terms of increase in aerodynamic coefficients. The sizing matrix plot can be obtained using the new performance requirements derived with the DEP model presented in order to predict the increase of aerodynamic coefficients during all the phases of mission profile. To understand the effectiveness of this procedure, Figure 3.15 presents the sizing matrix plot of the NASA X-57 Maxwell aircraft obtained with the sizing procedure for DEP aircraft.

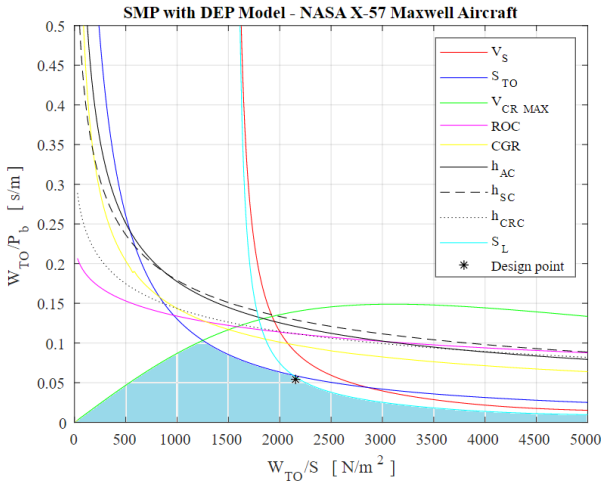

Figure 3.15: SMP with DEP model for NASA X-57 Maxwell aircraft.

Examining the SMP with DEP model and the standard SMP of referred aircraft it is interesting to notice how the feasibility region, painted in light blue in both figures, is estimated with the DEP model. The comparison attests the validity of the new procedure because the acceptable region is approximately the same and the design point of the NASA X-57 Maxwell is included in the new acceptable region. An interesting result of the SMP with new procedure for DEP system is the extension of the acceptable region to bigger values of wing loading related to small values of power loading. This extension is due to the change of the stall speed requirement and the landing distance requirement where the new expression of the lift coefficient is function of the power loading in both equations.

Considering the referred aircraft without the DEP system, the power is generated with only the cruise motors at the wingtip during all mission profile. The SMP can be obtained using conventional performance requirements [28] relative to airplanes certificated with CS Part 23. The aircraft analysed utilises the two wingtip electric motors for sustained flight and the wing is almost unblown because there are not twelve high-lift electric motors for DEP. For this reason, the sizing matrix plot is also named conventional unblown case and it is presented in Figure 3.16.

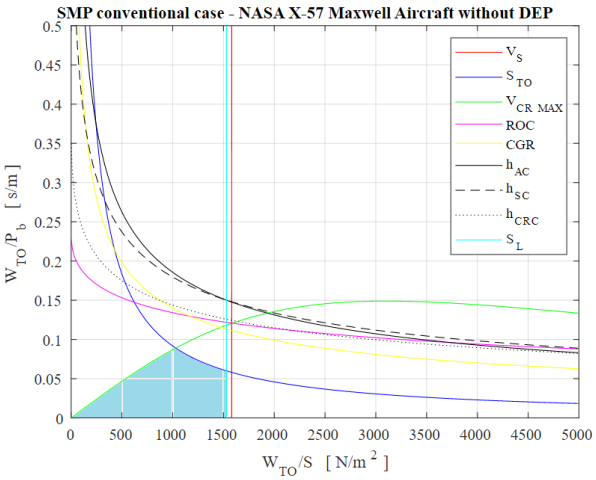

Figure 3.16: SMP in conventional case for NASA X-57 Maxwell aircraft without DEP system.

In order to confront the SMP of the X-57 Maxwell aircraft and the SMP of referred aircraft without the DEP system (unblown case), it is interesting to notice how the acceptable region, painted in light blue in all the figures, becomes bigger with the implementation of the DEP system. In this way, the SMP for DEP aircraft allows the selection of the design point with more flexibility and with a lower cost than the selection of the design point in the conventional unblown case. This result shows a great advantage that can be obtained with the implementation of the DEP system.

3.5 Summary of DEP Performance Sizing

The present chapter dealt with the necessity to establish a standard procedure for the preliminary sizing of electric aircraft with the DEP model implemented. Starting from the well-known design methods based on the analysis of the sizing matrix plot with the standard requirements of the mission profile, a new integrated procedure mixing the well-known constraints and the new parts derived from the DEP model was introduced for the specific case of electric powered aircraft with DEP system. The core of the sizing method is a new definition of the standard requirements for the SMP, in order to allow the study of the mission profile with the increase of the number of propellers along the DP array. The new procedure couples the results of the analysis of the sizing matrix plot with an increment due to the DEP system, yielding an integrated sizing procedure. In order to show a possible way to fully exploit the benefit of the proposed procedure, which is straightforward and computationally light, all requirements were evaluated also with the increase of number of propellers along the DP array. A complete preliminary sizing was illustrated for airplanes certificated in the weight category of the CS Part 23 and Part 25, showing both the advantages and disadvantages that could be investigated for different phases of the flight with the DEP system.

Both the new stall speed requirement, derived from reference [28], and the new take-off run requirement, derived from reference [26], confirmed a great advantage of the DEP system showing the increase of the acceptable region for the determination of the design point with the increase of the number of propellers N used for the DEP.

The new maximum cruise speed requirement, derived from reference [26], evinced a small penalty of the DEP system in cruise configuration showing the slight decrease of the acceptable region for the determination of the design point with the increase of the number of propellers N used for the DEP. This result is one of the reasons that led the high-lift propellers to fold smoothly onto the nacelle during the cruise configuration for this category of aircraft.

The new rate of climb requirement and new ceiling requirement, both derived from reference [28], also evinced a small penalty of the DEP system in climb configuration showing the slight decrease of the acceptable region for the determination of the design point with the increase of the number of propellers N used for the DEP.

The new climb gradient requirement, derived from reference [28], confirmed an advantage of the DEP system in climb configuration showing the slight increase of the acceptable region for the determination of the design point with the increase of the number of propellers N used for the DEP.

The new landing distance requirement, derived from reference [31], confirmed a great advantage of the DEP system in landing configuration showing the increase of the acceptable region for the determination of the design point with the increase of the number of propellers *N* used for the DEP.
The new technique for the wing area and engine sizing with DEP system is validated for the case of NASA X-57 Maxwell aircraft, showing the great affinity between the SMP with DEP model and the SMP in the conventional case. By comparing the SMP of the NASA X-57 Maxwell and the same aircraft without high-lift motors it was possible to show a glaring example of the great advantage obtained with the DEP.
The reasonable results obtained with such analyses tend to confirm the validity of DEP model implemented and the progress that can be achieved with the DEP in terms of thrust, power and weight saved.

Chapter 4 - Preliminary Sizing Applications

The purpose of this chapter is to illustrate the application of the proposed methodology to the preliminary sizing of propeller-driven aircraft, using the DEP model formalized in the previous chapters. The new sizing procedure for wing area and engine sizing has been integrated in a comprehensive aircraft preliminary sizing tool. The DEP preliminary sizing has been carried out for four different configuration variations of the NASA X-57 Maxwell aircraft, in order to study how the DEP influences the design of the vehicle and the complete mission profile.

4.1 Electric Aircraft Preliminary Sizing

The new sizing technique allows the determination of the wing loading and the power loading for DEP aircraft, which are two fundamental parameters for the valuation of the wing reference area and the engine power sizing. This new procedure has been implemented in the Matlab code named Hyperion (Hybrid Performance Simulation) program, a tool for electric aircraft preliminary sizing developed at the Department of the Aerospace Science and Technology, Politecnico di Milano [30]. Hyperion represents a novel methodology for the preliminary sizing of pure-electric and serial hybrid-electric airplanes; it is general and capable of dealing with propeller-driven airplanes of arbitrary configuration and size. The method takes into account the wider design space available to hybrid-electric aircraft compared to conventional ones.
The required input data are organized in five groups of values: aircraft data, drag estimation, required performance, hybrid and battery data, and simulation settings.

1. Aircraft: take-off and landing maximum lift coefficients, aspect ratio, Oswald efficiency factor, propeller efficiency, number of crew and passengers, number of engines.
2. Drag estimation: aircraft type, ΔC_{D0} due to flaps at take-off and landing gear, Oswald efficiency factor at take-off.
3. Performance: stall, cruise, descent and cruise speed, airport, loiter and cruise altitude, rate of climb and of descent, loiter time, take-off field length, target range.
4. Hybrid: propulsion type (all electric, hybrid-electric or conventional), type of generator, pressure/volume ratio (depending on the generator), generator power-to-weight ratio, alternator efficiency.
5. Battery: specific power and specific energy, minimum and maximum weight fraction.
6. Settings: measurement units for length, horizontal speed and vertical speed.

The program allows to compute the time evolution of all relevant quantities considered in flight simulation, referred to aircraft sizing and performance. The overall envelope is simulated by considering all the flight phases in chain, from take-off initialization to loiter end. The final covered distance is compared to requested range and a correction is provided. Hyperion is utilised to assess the sensitivity of key parameters such as battery performance, cruise speed and altitude, aircraft range

among others, on parameters such as take-off, battery and fuel mass, wing surface, motor power and energy degree of hybridization.
In the following subparagraphs, four different configurations of the NASA X-57 Maxwell aircraft are explained and the DEP preliminary design phase is developed. The payload mass is 209 kg for all configurations since all simulated aircraft have two seats and the final covered distance is fixed to a range of 106 km. Analysing the output data of the Hyperion program it is possible to make a comparison between the four different configurations, highlighting strengths and weaknesses of each of them during all phases of the flight.

4.2.1 Configuration 1 – NASA X-57 Mod-IV

The NASA X-57 Mod-IV represents the final configuration of the aircraft with the complete electric propulsion system [16]. This aircraft is part of the Scalable Convergent Electric Propulsion Technology Operations Research (SCEPTOR) program, which aims at designing, building and testing a demonstrator aircraft to display distributed electric propulsion technology. The NASA X-57 is a small experimental airplane, equipped with two cruise motors at the wingtip and twelve high-lift motors (DEP system) distributed along the wingspan. For the development of this aircraft, NASA has selected the Tecnam P2006T as the airframe on which to evaluate the potential of DEP, with the aim of developing safer, more energy-efficient, lower operating costs, and greener General Aviation aircraft. The large outboard propulsors (wingtip motors) are designed to be used in all flight regimes while the small inboard propulsors (high-lift motors) aimed to be used for lift augmentation, during slow speed areas such as take-off phase and landing phase. When the inboard propellers are not required, they fold in on themselves to reduce drag. The overall wing propulsive configuration is shown in Figure 4.1.

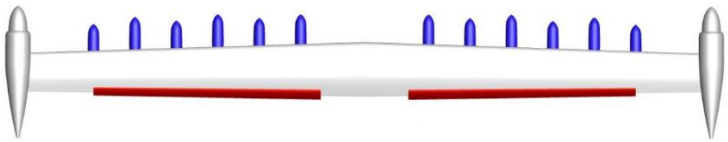

Figure 4.1: Top view of the NASA X-57 Mod-IV wingspan [1].

Table 4.1 summarizes all output data from Hyperion program relative to the first configuration, organized in four groups and compared to the exact value of the NASA X-57 in its final configuration.

X-57 Mod-IV Preliminary Sizing				
Data symbols	Estimated values	Exact values	Units	Percentage errors
W_{TO}/S	2125.8	2156.4	N/m²	1.4 %
W_{TO}/P_b	0.0547	0.0542	s/m	0.9 %
N_{HL}	12	12	—	—
N_T	2	2	—	—
Aerodynamics				
S	6.08	6.19	m²	1.7 %
b	9.55	9.6	m	0.5 %
Weight Breakdown				
MTOW	1318	1360	kg	3.0 %
M_a	654	688	kg	4.9 %
M_b	386	390	kg	1.1 %
M_{HLM}	26.33	28.08	kg	5.8 %
M_{TM}	43.17	44.4	kg	2.7 %
Powertrain				
MCP	236	246	kW	3.9 %
MCP_{HLM}	118	126	kW	6.2 %
MCP_{TM}	118	120	kW	1.5 %

Table 4.1: Output values for NASA X-57 Mod-IV.

Where the parameter N_{HL} represents the number of high-lift propellers and N_T the number of wingtip propellers. Referring to the weight breakdown, the parameter M_a non-propulsive airframe mass, M_b battery pack mass, M_{HLM} high-lift motors mass, M_{TM} wingtip motors mass. Referring to the powertrain, the parameter MCP represents the maximum continuous power, MCP_{HLM} is the MCP of high-lift motors and MCP_{TM} is the MCP of wingtip motors. The previous table shows good accordance with real values of NASA X-57 Maxwell aircraft, pointing out the good prediction of the DEP preliminary design phase for an early phase of design with Hyperion program.

The wing loading and the power loading are obtained with the new sizing technique for DEP aircraft and it is possible to execute a good estimation with a low percentage error respect to the real values. Figure 4.2 presents the SMP of the NASA X-57 Mod-IV simulated aircraft.

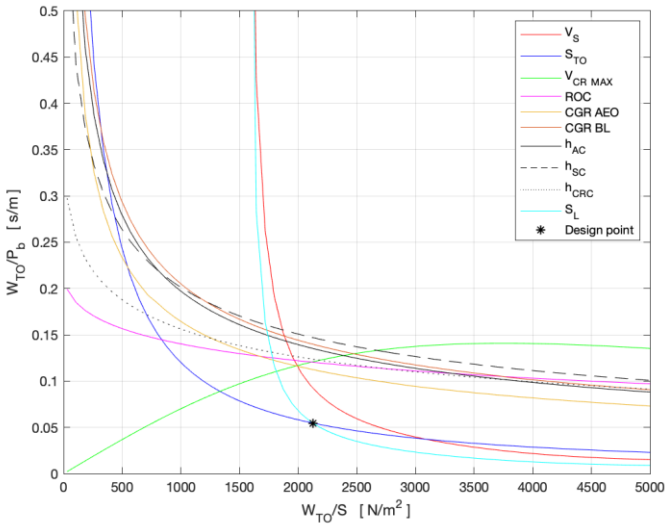

Figure 4.2: SMP with DEP model for NASA X-57 Mod-IV.

Starting from what we discussed in chapter 3, the SMP is implemented with the Climb Gradient Requirement with All Engines Operative (CGR AEO) and with the Climb Gradient Requirement for Balked Landing (CGR BL), referring to the certification CS Part 23. The Climb Gradient Requirement with One Engine Inoperative (CGR OEI) is not considered because there is not yet a certification establishing how to check this constraint in the case of large number of propellers (DEP case).
Figure 4.3 shows the evolution of the battery State Of Charge (SOC) and the evolution of the mission profile respect to the height reached in the different phases of the simulated flight.

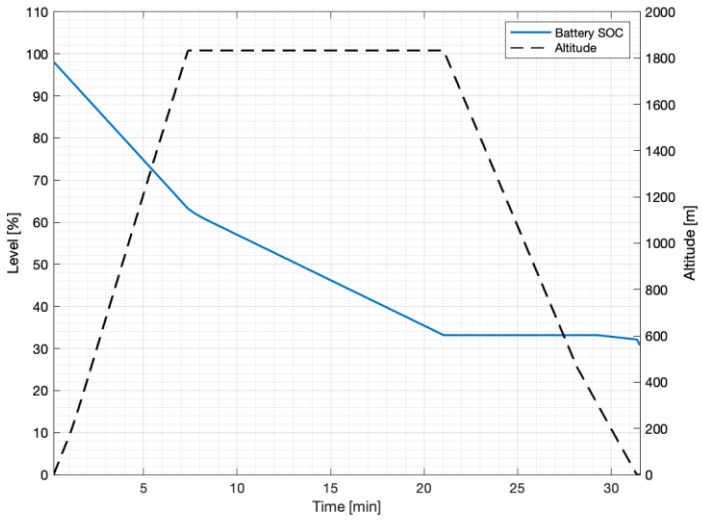

Figure 4.3: Variables evolution for NASA X-57 Mod-IV.

4.2.2 Configuration 2 – NASA X-57 Mod-IV DEP-AO

The NASA X-57 Mod-IV DEP Always On (DEP-AO) represents the same structural aircraft of the first configuration but with a different use of the DEP system. The NASA X-57 Mod-IV DEP-AO is equipped with two cruise motors at the wingtip and twelve high-lift motors (DEP system) distributed along the wingspan. In the second configuration, both the large outboard propellers (wingtip motors) and the small inboard propellers (high-lift motors) are designed to be used in all flight regimes; for this reason we have chosen to use the acronym DEP-AO. The application of the DEP preliminary design phase to the second configuration is developed to emphasize strengths and limitations of DEP for all phases of simulated mission profile. The overall wing propulsive configuration is shown in Figure 4.4.

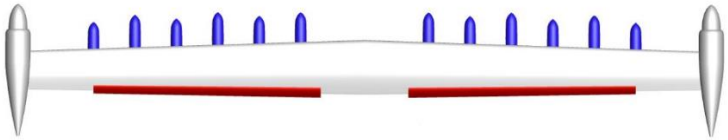

Figure 4.4: Top view of the NASA X-57 Mod-IV DEP-AO wingspan [1].

Table 4.2 summarizes all output data from Hyperion program relative to the second configuration, organized in four groups.

X-57 Mod-IV DEP-AO Preliminary Sizing		
Data symbols	Estimated values	Units
W_{TO}/S	2125.9	N/m²
W_{TO}/P_b	0.0547	s/m
N_{HL}	12	–
N_T	2	–
Aerodynamics		
S	6.08	m²
b	9.55	m
Weight Breakdown		
MTOW	1318	kg
M_a	654	kg
M_b	386	kg
M_{HLM}	26.33	kg
M_{TM}	43.17	kg
Powertrain		
MCP	236	kW
MCP_{HLM}	118	kW
MCP_{TM}	118	kW

Table 4.2: Output values for NASA X-57 Mod-IV DEP-AO.

The previous table shows the same results of the first configuration because the structure and the engine sizing of the aircraft are the same; some differences can be observed in figure 4.5, where the entire mission profile is influenced by the use of both different motors in all flight regimes.
Figure 4.5 presents the SMP of the NASA X-57 Mod-IV DEP-AO simulated aircraft.

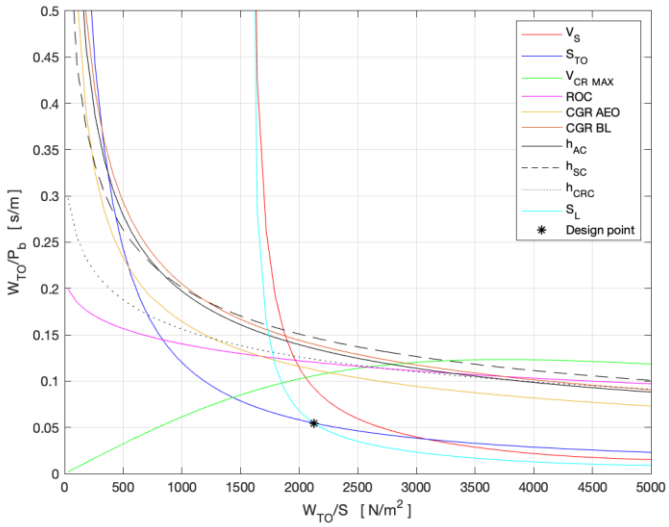

Figure 4.5: SMP with DEP model for NASA X-57 Mod-IV.

The wing loading and the power loading are obtained with the new sizing technique for DEP aircraft. It is possible to notice the same design point of the first configuration because it depends on the intersection of the take-off run requirement and the landing distance requirement. In both these flight phases, the DEP system is operative also in the first configuration and so the hyperbolic curves are the same. The most differences are highlighted in the other seven requirements, where the constraints change its behaviour as described in Chapter 3. Also, if performances decrease the acceptable region respect to the first configuration (now the maximum cruise speed requirement is more restrictive), they do not drastically change the selection of the design point.
Figure 4.6 shows the evolution of SOC and the evolution of the mission profile respect to the altitude reached in different phases of the simulated flight.

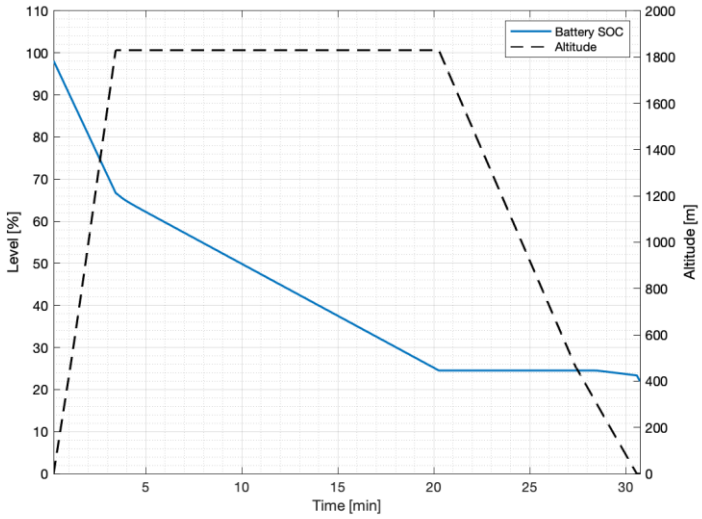

Figure 4.6: Variables evolution for NASA X-57 Mod-IV DEP-AO.

4.2.3 Configuration 3 – NASA X-57 LEAPTech wing

The NASA X-57 LEAPTech wing represents a variation of the NASA X-57 Mod-IV with the DEP system spread out along the entire wingspan. The third configuration is equipped with two cruise motors of the same dimensions and shaft power of the twelve high-lift motors distributed along the wingspan, composing a DEP system of fourteen electric motors. Both the wingtip motors and the inboard propellers are designed to be used in all flight regimes as well as the LEAPTech wing configuration. The overall wing propulsive configuration is shown in Figure 4.7.

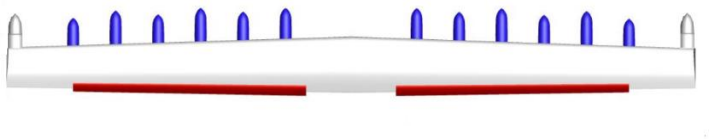

Figure 4.7: Top view of the NASA X-57 LEAPTech wingspan.

Table 4.3 summarizes all output data from Hyperion program relative to the third configuration, organized in four groups. In order to make an interesting comparison between all configurations, the parameters estimated are divided both for wingtip motors and high-lift motors, also if the dimension and the shaft power of the single motor is the same in this configuration.

X-57 LEAPTech wing Preliminary Sizing		
Data symbols	Estimated values	Units
W_{TO}/S	2598.5	N/m²
W_{TO}/P_b	0.0469	s/m
N_{HL}	12	—
N_C	2	—
Aerodynamics		
S	5.24	m²
b	8.87	m
Weight Breakdown		
MTOW	1389	kg
M_a	641	kg
M_b	475	kg
M_{HLM}	55.52	kg
M_{CM}	9.25	kg
Powertrain		
MCP	291	kW
MCP_{HLM}	249	kW
MCP_{CM}	42	kW

Table 4.3: Output values for NASA X-57 LEAPTech wing.

The wing loading and the power loading are obtained with the new sizing technique for DEP aircraft. The wing loading estimated in the first configuration is increased respect to the NASA X-57 Mod-IV since now the total power of the high-lift motors is increased and they automatically produce a bigger increment for the aerodynamic coefficient than the first configuration. The increase of the wing loading is followed by a slightly decrease of the power loading, due to the increment of the MCP for all motors along the wingspan. Figure 4.8 presents the SMP of the LEAPTech wing simulated aircraft.

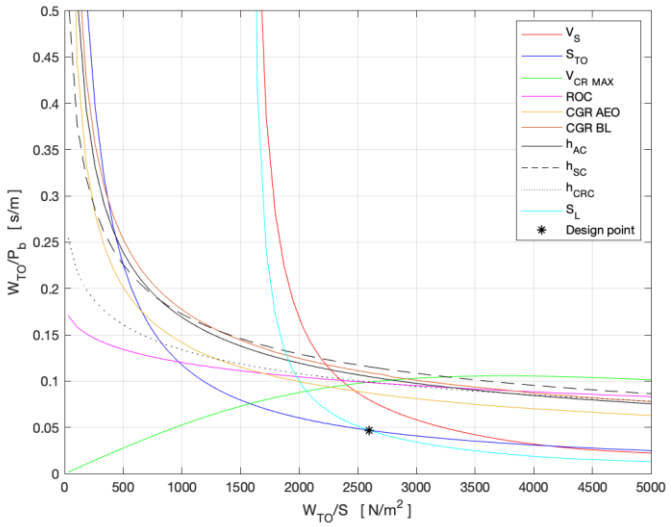

Figure 4.8: SMP with DEP model for NASA X-57 LEAPTech wing.

Figure 4.9 shows the evolution of SOC and the evolution of the mission profile respect to the altitude reached in different phases of the simulated flight.

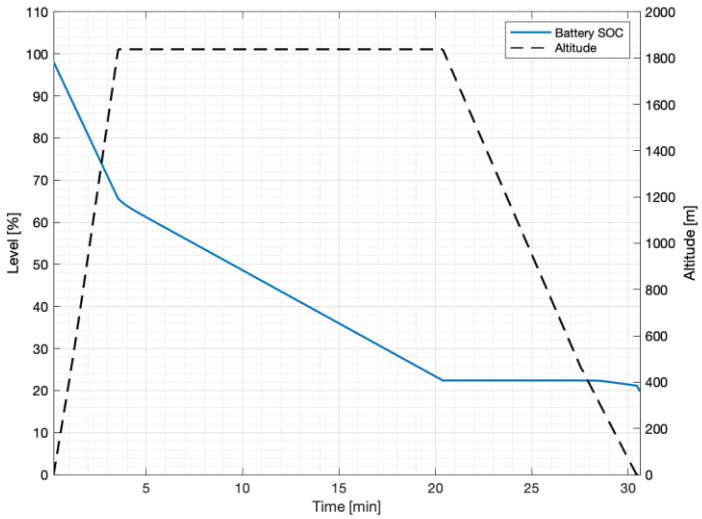

Figure 4.9: Variables evolution for NASA X-57 LEAPTech wing.

4.2.4 Configuration 4 – NASA X-57 Mod-II

The NASA X-57 Mod-II represents an intermediate configuration of the aircraft with all-electric propulsion system [16]. Since the NASA X-57 Mod-I corresponds to the original Tecnam P2006T aircraft; the NASA X-57 Mod-II replaces the original engine and propellers with an electric propulsion system and optimized propellers. The fourth configuration is equipped with two large motors in wing roots without any high-lift motors for DEP system, like the conventional electric aircraft. The large

inboard propellers (wing root motors) are designed to be used in all flight regimes. The overall wing propulsive configuration is shown in Figure 4.10.

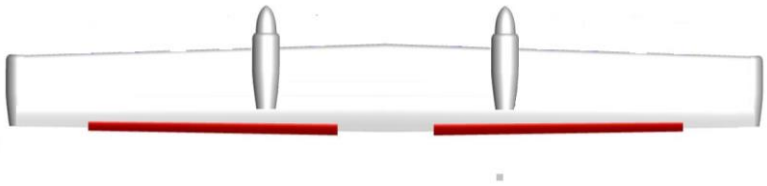

Figure 4.10: Top view of the NASA X-57 Mod-II wingspan.

Table 4.4 summarizes all output data from Hyperion program relative to the fourth configuration, organized in four groups.

X-57 Mod-II Preliminary Sizing		
Data symbols	Estimated values	Units
W_{TO}/S	789.8	N/m²
W_{TO}/P_b	0.075	s/m
N_{HL}	0	—
N_R	2	—
Aerodynamics		
S	18.51	m²
b	12.76	m
Weight Breakdown		
MTOW	1491	kg
M_a	749	kg
M_b	462	kg
M_{HLM}	0	kg
M_{RM}	71.22	kg
Powertrain		
MCP	195	kW
MCP_{HLM}	0	kW
MCP_{RM}	195	kW

Table 4.4: Output values for NASA X-57 Mod-II.

Where the parameter N_R represents the number of propellers at wing roots, M_{RM} is the wing root motors mass and MCP_{RM} is the MCP of motors at wing roots. The previous table shows the increment of the maximum take-off weight respect to the other three DEP configurations and the decrease of the total MCP required for the mission profile. The wing loading and the power loading are obtained with the conventional sizing technique for electric aircraft. The wing loading is decreased respect to the other three DEP configurations, while the power loading is slightly bigger than the NASA X-57 Mod-IV. Figure 4.11 presents the SMP of the NASA X-57 Mod-II simulated aircraft.

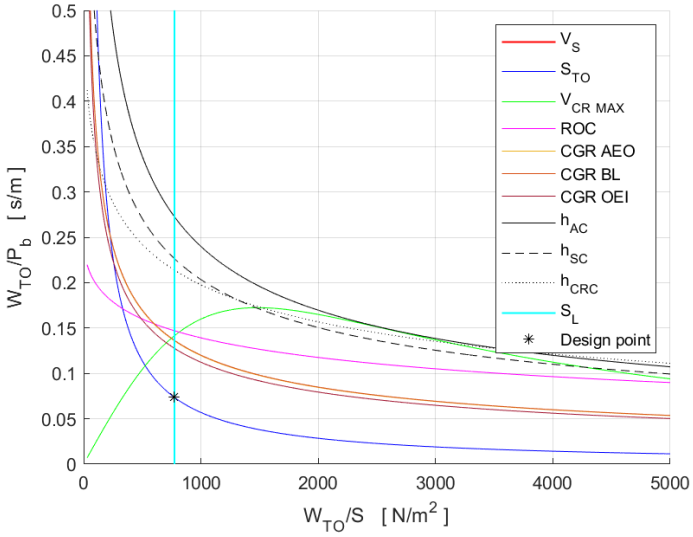

Figure 4.11: SMP with DEP model for NASA X-57 Mod-II.

With Respect to the other three configurations, CGR OEI is considered since the CS Part 23 establishes how to check this constraint in the case of conventional propeller-driven aircraft. Figure 4.12 shows the evolution of SOC and the evolution of the mission profile respect to the height reached in different phases of the simulated flight.

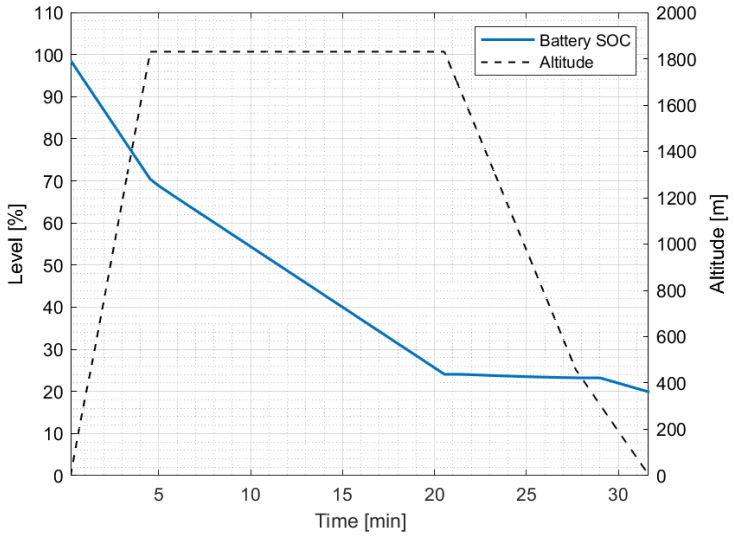

Figure 4.12: Variables evolution for NASA X-57 Mod-II.

4.3 Configuration Comparison

This section provides an extensive comparison between the four sized design configurations in order to understand strengths and weakness noticeable with DEP in a preliminary sizing phase.
Figure 4.13 shows the maximum take-off weight and the wing surface obtained with the Hyperion program.

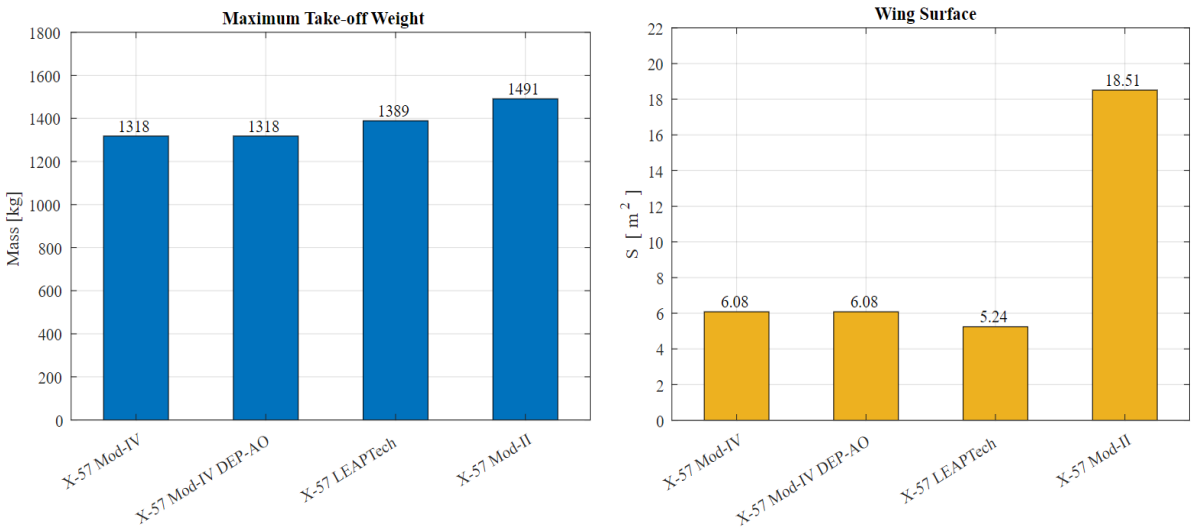

Figure 4.13: Comparison of maximum take-off weight and wing surface for different configurations.

The first two configurations have the same structural output values since they are both referred to the NASA X-57 Mod-IV. The fourth configuration has oversized MTOW and wing surface respect to the other configurations, which provides the first advantage of the DEP system. The third configuration presents a smaller wing surface than the other configurations but a bigger MTOW. This result is better explained in Figure 4.14 that provides a complete breakdown of the aircraft mass.

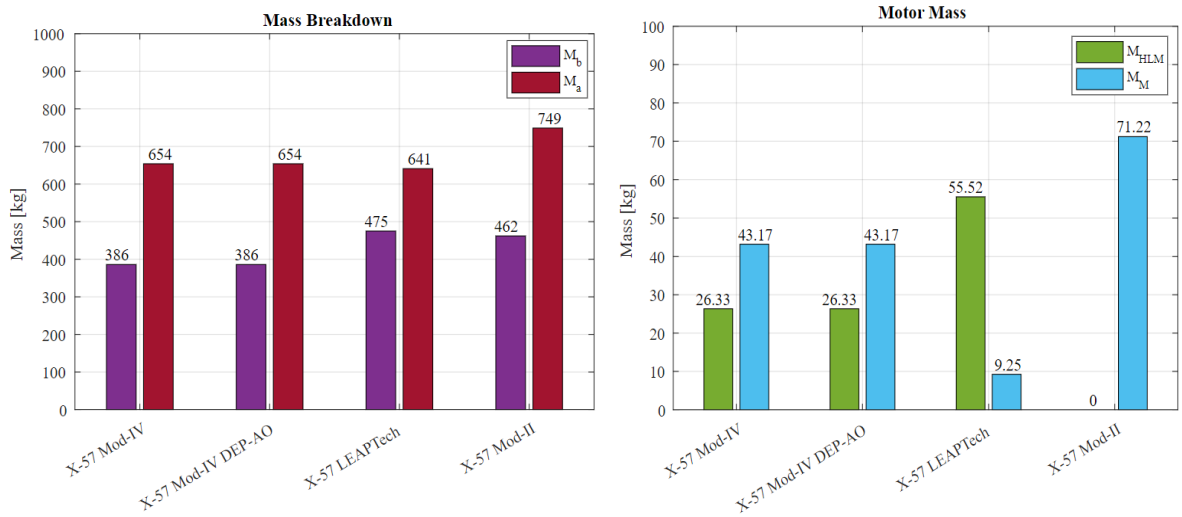

Figure 4.14: Comparison of mass breakdown for different configurations.

In the left plot, it is possible to see, with respect to the first two configurations, that in the third configuration M_a slight decreases, but instead M_b largely increases thus generating an increase also in the MTOW. The fourth configuration presents the biggest M_a and total motors mass, producing the biggest MTOW for this comparison. In the right plot the breakdown of the motor mass is showed, where the parameter M_M represents motors mass without considering high-lift motors (in the first three configurations, it represents the wingtip motors mass, while in the fourth configurations it represents the midwing motors mass). In the third configuration, it is interesting to notice how the high-lift motors

increase their mass since there are not two large motors available at wingtip and so they need to produce more power than in the first two configurations.
Figure 4.15 shows the powertrain of the four configurations, separately considering the effect of high-lift motors and the remaining engines.

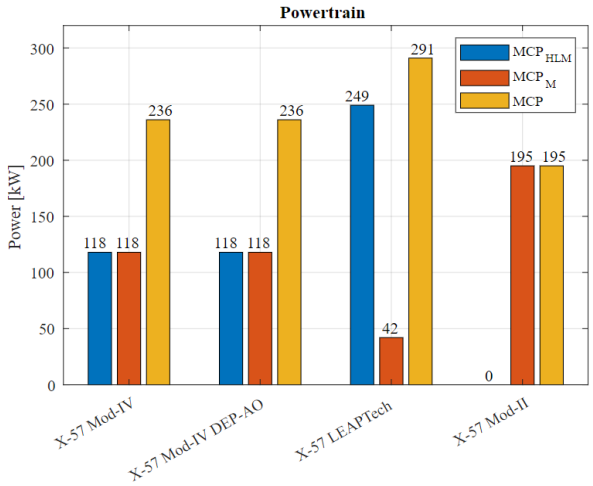

Figure 4.15: Comparison of powertrain for different configurations.

The first two configurations have a total MCP a lower than the third configuration, providing that the distribution of energy between high-lift motors and standard motors generates an advantage in term of total power required respect to a configuration with only high-lift motors. The fourth configuration has the lowest total MCP required as highlighted by the lowest power loading in this comparison.
Figure 4.16 shows the comparison of the SOC and the power management during all simulated flight for the four configurations.

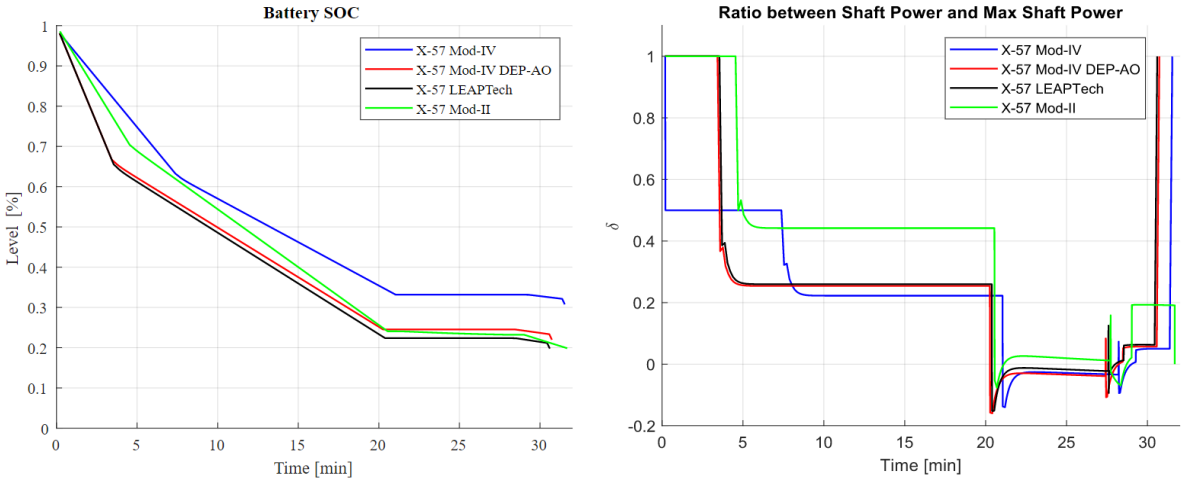

Figure 4.16: Comparison of variables evolution during simulated flight.

The parameter δ represents the ratio between shaft power and maximum shaft power and in the left plot its evolution during the mission profile is analysed. In order to make an interesting comparison, the variables considered are extrapolated from Figure 4.16 and they are summarized in Table 4.5.

Configuration	X-57 Mod-IV	X-57 Mod-IV DEP-AO	X-57 LEAPTech	X-57 Mod-II
SOC_{FINAL}	0.3074 %	0.2195 %	0.2 %	0.2 %
δ_{CR}	0.225	0.2543	0.2595	0.4419

Table 4.5: Comparison of variables during simulated flight.

By comparison, the final level of SOC in the first configuration is sensitively bigger than the other three configurations where this value is near the minimum fixed imposed by Hyperion program. Considering that all the configurations cover the same range, the use of DEP system only for take-off and landing phases gives an advantage in terms of battery saving. The parameter δ_{CR} indicated the ratio between the shaft power in cruise phase and the maximum shaft power, which is the phase of flight with longer duration. By comparing, even in this case the first configuration gives the best result since a lower value of δ_{CR} corresponds to an advantage in terms of energy management. The fourth configuration has the worst condition in terms of power management, highlighting the improvement that DEP can make in cruise phase.

Figures 4.17 and 4.18 show the behaviour of the total lift coefficient and the unblown lift coefficient during the simulated flight, in order to see how the DEP system changes the aerodynamic performances of the aircraft. To emphasize the effect of the high-lift motors, the unblown lift coefficient is also plotted with a dotted line. For the four configuration, only the total lift coefficient is presented since the DEP system is not utilised.

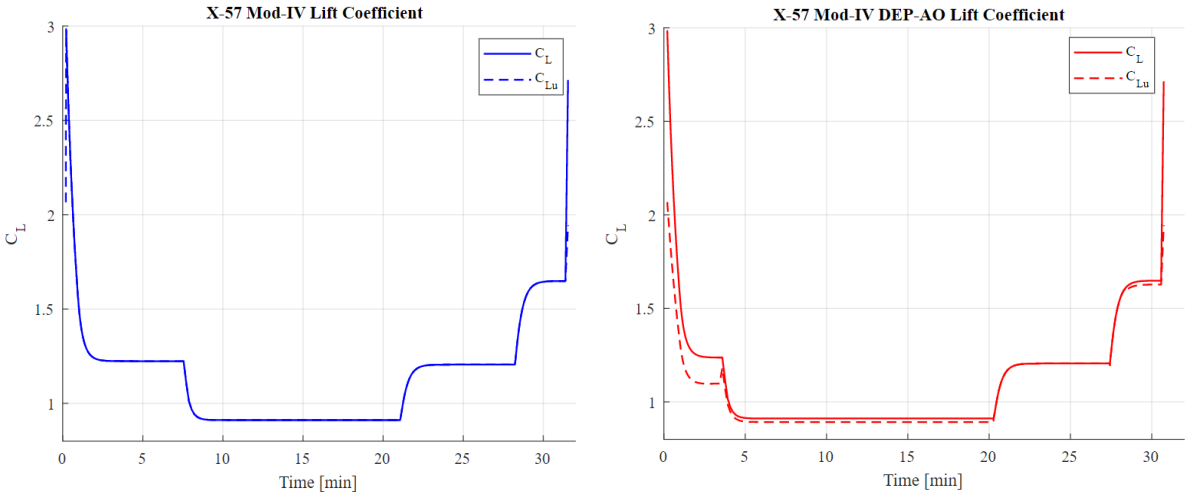

Figure 4.17: Evolution of lift coefficient during simulated flight for X-57 Mod-IV and X-57 Mod-IV DEP-AO.

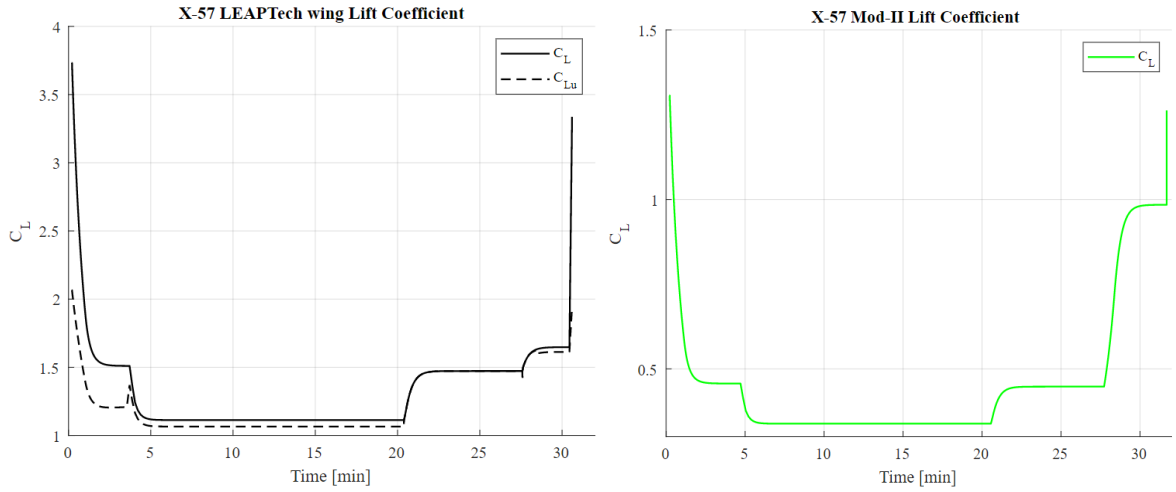

Figure 4.18: Evolution of lift coefficient during simulated flight for X-57 LEAPTech wing and X-57 Mod-II.

By comparison, the increase of lift coefficient is appreciable only in the take-off and landing phases in the first configuration, while it is noticeable during the entire flight mission in the second and third configurations.

Figure 4.19 shows the comparison of aerodynamic parameters during all simulated flights for the four configurations. The aerodynamic parameters considered are the lift coefficient and the lift-to-drag ratio.

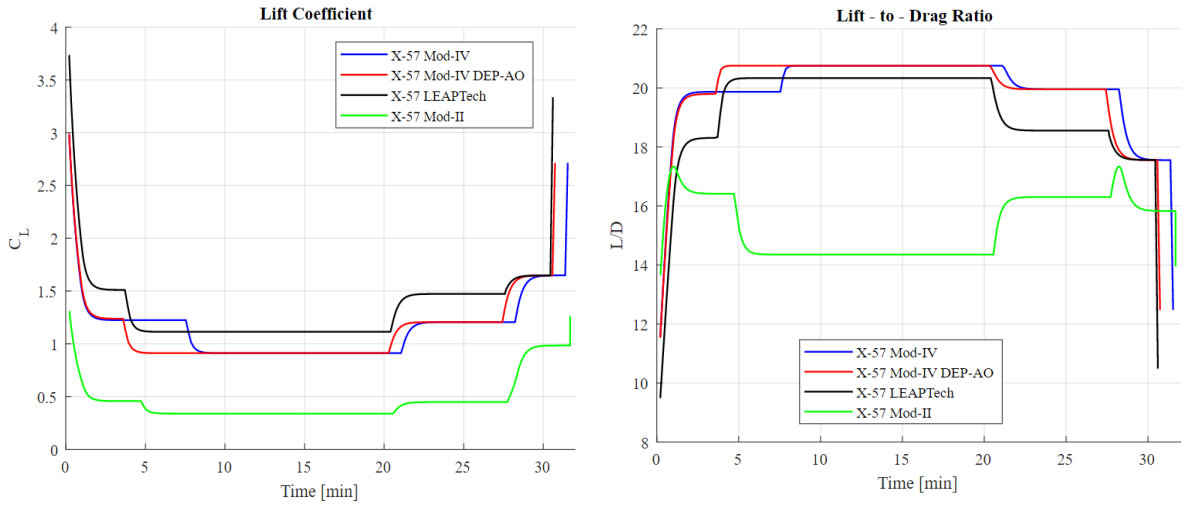

Figure 4.19: Comparison of aerodynamic parameters evolution during simulated flight.

The parameter *L/D* represents the lift-to-drag ratio and in the right plot its evolution during the mission profile is analysed. In order to make an interesting comparison, the aerodynamic parameters considered are extrapolated from the previous figures and they are summarized in Table 4.6.

Configuration	X-57 Mod-IV	X-57 Mod-IV DEP-AO	X-57 LEAPTech	X-57 Mod-II
$C_{L\,MAX}$	2.98	2.98	3.73	1.31
$L/D_{\,MAX}$	20.75	20.74	20.33	17.33
$L/D_{\,CR}$	20.75	20.74	20.33	13.67
$L/D_{\,TO}$	11.55	11.55	9.5	13.67
$L/D_{\,LND}$	12.47	12.47	10.48	13.95

Table 4.6: Comparison of aerodynamic parameters during simulated flight.

To make things clearer, the aerodynamic values presented in the above table are relative to the simulated mission profile with the Hyperion program, so the parameters $C_{L\,MAX}$ and $L/D_{\,MAX}$ are not the maximum values that the aircraft can reach but they are just the maximum values reached in the considered mission profile. The third configuration presents the maximum value of $C_{L\,MAX}$ since the high-lift motors have more power than the first two configurations. The fourth configuration has the lowest value of C_{LMAX} since the DEP system it is not implemented and this aspect also influences the aerodymic efficiency of aircraft.
By comparison, the first configuration has the maximum $L/D_{\,MAX}$ while the fourth configuration has the minimum $L/D_{\,MAX}$. It is also interesting to notice what happens when the different configurations reach the maximum aerodynamic efficiency: the first three configurations with DEP system reach the maximum efficiency during the cruise phase, while the fourth configuration reaches the maximum efficiency during an intermediate phase of climb. This effect is discussed also in [3], where it is explained that $L/D_{\,MAX}$ occurs at a higher velocity as the maximum lift capability of the wing increases for a given stall speed. This illustrates one of the benefits of using DEP to augment the lift over the wing at lower speeds. The aerodynamic efficiency at higher speeds is generally higher for smaller wings, improving the performance in cruise which is generally the flight phase with longest duration.

4.4 Summary of Preliminary Sizing Applications

Starting from the work in Chapter 3, the new sizing technique for DEP aircraft is implemented in the Hyperion program for the preliminary design phase of electric aircraft, expanding analytical skills of the program relative to DEP. The DEP preliminary design phase is applied to four different configurations of the NASA X-57 Maxwell electric aircraft, in order to develop a clear comparison with the purpose to emphasize strengths and weaknesses of the DEP system.
In order to validate the DEP preliminary design phase, the first case is compared to the real values of the NASA X-57 Mod-IV electric aircraft. The comparison shows good accordance with real values of NASA X-57 Maxwell aircraft, pointing out the good prediction of the DEP preliminary design phase for an early phase of design with Hyperion program.
The first configuration is the NASA X-57 Mod-IV aircraft, which presents an optimal compromise between wing loading and power loading for the selection of the design point in the SMP. The small

dimension of the wing surface emphasizes one of the benefits of the DEP and the MTOW is the lowest among the configurations studied. In addition to being the lightest configuration, it is also the best aircraft in terms of battery saving and power management. The final level of SOC is the highest and the parameter δ_{CR} highlights how the powered down of the high-lift motors during cruise is the best strategy. By comparison, the first configuration has the highest aerodynamic efficiency and, above all, it is obtained during cruise phase.

The second configuration is the NASA X-57 Mod-IV DEP-AO aircraft. This configuration presents the same SMP of the first configuration since it is the same aircraft but with a different management of the high-lift motors. Although the first and the second configuration are the lightest aircraft, the second is not the best aircraft in terms of battery saving and power management. The final level of SOC is lower than the first configuration's value and the parameter δ_{CR} shows that the high-lift motors always on are not convenient.

The third configuration is the NASA X-57 LEAPTech aircraft. This configuration presents the best compromise between wing loading and power loading for the selection of the design point in the SMP. The smallest dimension of the wing surface emphasizes one of the benefits of the DEP but the MTOW is relative higher than the first two configurations, due to the increase power and mass of the high-lift motors. The MCP required for the mission profile is the highest and the final level of SOC is lower than the first configuration's value. In addition, the third configuration has a lower aerodynamic efficiency than the first two configurations, showing that a wing completely used for DEP reduces its dimension but sets great limitations on aircraft performance. The results obtained with the third configuration explain that the primary purpose of high-lift motors is to augment lift of the wing at low speed and they are not designed to provide primary propulsion.

The fourth configuration is the NASA X-57 Mod-II aircraft. This configuration presents the lowest wing loading and the highest power loading. The big dimension of the wing surface emphasizes one of the drawbacks of the conventional propulsion system and the MTOW is the highest among the configurations studied. In addition to being the heavier configuration, its battery saving and power management are not convenient. The final level of SOC is lower than the first configuration value and the parameter δ_{CR} is the highest value, showing another drawback of the conventional propulsion system respect that DEP. By comparison, the last configuration has the lowest L/D_{MAX} and in particularly it is obtained during the climb phase. This analysis highlights another penalty of the conventional propulsion system that can encourage the development of the DEP system as a new frontier of electric propulsion.

Chapter 5 - Conclusion

The purpose of this chapter is to illustrate outcomes and results of the work performed in this thesis, considering a critical discussion of the overall approach on DEP modelling for performance sizing, as a starting point for future developments in this exciting and promising propulsion concept.

5.1 Concluding Remarks and Recommendations

In the present work was aimed at presenting a general method for the aircraft preliminary sizing phase dedicated to airplane provided with a DEP system. A technology survey was conducted to assess the current developments of DEP, electric motors, and aerodynamic performance and to predict future trends.

A literature survey on DEP system was carried out to compare the estimation of the variation in aerodynamic coefficients, according to methods and approaches developed by different authors. Since Reynard de Vries' approach was considered to present the most accurate model, it was selected as reference. Some modifications to the original structure of this model were implemented, based on theoretical analysis and studies, in order to improve the final results.

In order to verify the capability of the improved DEP model, a validation phase was carried out, so to analyse the model through a comparison with experimental results and CFD results in different conditions and for various types of aircraft. The DEP model was tested for the case of the NASA X-57 demonstrator [1] and for the LEAPTech wing [2], as well as with Sinnige's experimental data [13], to check whether the model is accurate also for other propeller configurations. The DEP model generally showed good agreement with CFD results and experimental data both for aircraft with DEP system and for conventional aircraft provided with few propellers. Following this validation phase, it was possible to consider the DEP model as a valid tool to estimate aerodynamic coefficients in an early phase of the design of aircraft featuring high-lift propeller systems.

Subsequently, an innovative sizing procedure for propeller-driven aircraft with the DEP system was developed, exploiting the use of the improved model. Starting from well-known design methods based on the analysis of the Sizing Matrix Plot with the standard requirements of the mission profile, a new integrated procedure mixing the conventional constraints and the new parts derived from the DEP model was introduced for the specific case of electric powered aircraft with DEP system. The core of the sizing method is a new formulation of the standard aircraft performance requirements considered in the SMP, in order to allow the study of the mission profile with the increase of the number of propellers along the wingspan. The new procedure coupled the results of the analysis of the SMP with an increment due to the DEP model, yielding an integrated sizing procedure. A complete preliminary sizing was illustrated, showing both possible advantages and the disadvantages that may arise with a DEP configuration. The new technique for the wing area and engine sizing with DEP system was validated for the case of NASA X-57 Maxwell aircraft, showing the great affinity between the SMP with DEP model and the SMP in the conventional case.

A comparison between the SMP of the NASA X-57 Maxwell and the same aircraft without high-lift motors showed a glaring example of the great advantage obtained with the DEP. The reasonable results obtained with such analyses tend to confirm the validity of DEP model implemented and the progress that can be achieved with the DEP in terms of thrust, power and weight saved.
The new sizing technique for DEP aircraft was implemented in the Hyperion program for the preliminary design phase of electric aircraft, expanding analytical skills of the program relative to DEP. The program allows to compute the time evolution of all relevant quantities considered in flight simulation, referred to aircraft sizing and performance. The overall envelope was simulated by considering all the flight phases in chain, from take-off initialization to loiter end. Hyperion was utilised to assess sensitivity of key parameters such as battery performance, cruise speed and altitude, aircraft range among others, on parameters as take-off, battery saving, wing surface and motor power.
In order to validate the new DEP preliminary design phase, the procedure was executed first for the NASA X-57 Mod-IV electric aircraft and then compared to the real values. The comparison showed good accordance with reality, pointing out the good prediction of the DEP preliminary design phase for an early phase of design with Hyperion program.
Subsequently, the application of the DEP preliminary sizing methodology was tested with four different configurations of the NASA X-57 Maxwell electric aircraft, in order to develop a clear comparison with the purpose to emphasize strengths and weaknesses of the DEP system. The comparison emphasized the benefits of the DEP aircraft respect to the conventional propeller-driven aircraft, pointing out an improvement not only related to the structural part, but also connected to aerodynamic efficiency of the aircraft during the cruise phase. It was also shown that a clear improvement in aerodynamic performance can be achieved with the use of high-lift motors only in specified phases of mission profile like take-off and landing. Through a direct comparison, it was highlighted that the primary purpose of high-lift motors should be to augment lift of the wing at low speed, while their use to provide primary propulsion is not convenient.

5.2 Future Developments

Future work and studies are foreseen relying on the developed DEP analysis and sizing technique. Indeed, the generality of the approach shall grant the ability to consider the design of aircraft of arbitrary weight category, ranging from smaller General Aviation to commuters and regional liners. Also, currently emerging applications in personal air transportation (PAVs, Personal Air Vehicles) and Urban Air Mobility (UAM) may be considered.
Concerning further improvements, the DEP model can be ameliorated in view to the following points:

1. Considering variations in lift due to the swirl, the aerodynamic effect of each propeller on the adjacent and the contribution of the increase in wetted area due to high-lift pylons and nacelles relative to the drag coefficient.
2. Tip mounted propellers are able to reduce induced drag and increase the overall lift-to-drag ratio, especially in cruise [36]. This effect should be included in the aero-propulsive interaction model for more accurate performance estimation.

3. Considering not only tractor configurations and leading edge distributed propeller configuration but also other kind of configurations (pusher, over the wing, etc.).
4. The formulation of take-off performance requirement for DEP aircraft can be improved, taking into consideration also the airborne section where the effect of the DEP system is more crucial.
5. Landing performance is heavily influenced by DEP. While blowing the wing with the distributed propellers increases the lift coefficient, thrust is also present until touch-down. This may lead to undesired acceleration in the final approach segment when there is the need to slow down the airplane. Therefore, further investigations on the formulation of landing performance requirement for DEP aircraft should be carried out to enhance accuracy of predictions.
6. The formulation of climb gradient OEI performance requirement for DEP aircraft can be formalized starting from a specified number of inoperative engines and with the remaining engines at no more than maximum continuous power, in order to investigate degraded thrust flight conditions and their effects.

Ringraziamenti

Ringrazio in primis il mio relatore, Prof. Lorenzo Trainelli, che condividendo le sue conoscenze mi ha guidato nell'organizzazione di questo lavoro e mi ha trasmesso la passione e l'entusiasmo necessari affinché la tesi prendesse forma giorno dopo giorno.
Ringrazio moltissimo i correlatori Prof. Carlo E. D. Riboldi e Prof. Alberto L. M. Rolando, sempre disponibili e pazienti, pronti a trovare soluzioni semplici a problemi molto complessi.
Ringrazio sentitamente il dott. Francesco Salucci, dottorando di ricerca presso il Dipartimento di Scienze e Tecnologie Aerospaziali, che ha saputo guidarmi in questo lungo progetto di tesi e mi ha spiegato concetti, a me a volte completamente sconosciuti, con estrema sintesi, chiarezza e semplicità.
Un ringraziamento speciale alla mia famiglia: è grazie al loro sostegno e al loro incoraggiamento se oggi sono riuscito a raggiungere questo traguardo.

Bibliography

[1] K. A. Deere, J. K. Viken and S. A. Viken, "Computational Analysis of a Wing Designed for the X-57 Distributed Electric Propulsion Aircraft," 17th *AIAA Aviation Technology, Integration, and Operations Conceference, Denver, CO,* pp. 1-22, 2017.

[2] K. A. Deere and S. A. Viken, "Computational Analysis of Powered Lift Augmentation for the LEAPTech Distributed Electric Propulsion Wing," 35th *AIAA Applied Aerodynamics Conceference, Denver, CO,* pp. 1-20, 2017.

[3] N. K. Borer, M. D. Patterson and J. K. Viken, "Design and Performance of the NASA SCEPTOR Distributed Electric Propulsion Flight Demonstrator," *16th AIAA Aviation Technology, Integration, and Operations Conceference, Washington, DC,* pp. 1-20, 2016.

[4] A. M. Stoll and J. Bevirt, "Drag Reduction through Distributed Electric Propulsion," 14th AIAA *Aviation Technology, Integration, and Operations Conference, Atlanta, GA,* pp. 1-10, 2014.

[5] B. J. Brelje and J. R. Martins, "Electric, hybrid, and turboelectric fixed-wing aircraft: A review of concepts, models, and design approaches," *Progress in Aerospace Sciences 104,* pp. 1-19, 2019.

[6] R. D. Vries and M. Brown, "A Preliminary Sizing Method for Hybrid-Electric Aircraft Including Aero-Propulsive Interaction Effects," 2018 *Aviation Technology, Integration, and Operations Conference, Atlanta, GA,* pp. 1-29, 2018.

[7] M. D. Patterson and B. J. German, "Simplified Aerodynamics Models to Predict the Effects of Upstream Propellers on Wing Lift," 53rd *AIAA Aerospace Sciences Meeting ,* Kissimee, FL, no. 2015-1673, 2015.

[8] M. D. Patterson, "Conceptual design of high-lift propeller systems for small electric aircraft," PhD Dissersation, *Georgia Institute of Technology,* 2016.

[9] E. Obert, "Method for the determination of the effect of the propeller slipstream on static longitudinal stability and control of multi-engined aircraft," *Delft University of Technology, Faculty of Aerospace Engineering,* Report LR-761, 1994.

[10] A. Jameson, "Analysis of wing slipstream flow interaction," *Tech. rep., NASA,* 1969.

[11] M. D. Patterson and B. J. German, "Conceptual Design of Electric Aircraft with Distributed Propellers: Multidisciplinary Analysis Needs and Aerodynamic Modeling Development," *52nd Aerospace Sciences Meeting,* National Harbor, Maryland, pp. 1-18, 2014.

[12] A. R. Marretta and G. Davi., "Hybrid numerical technique for evaluating wing aerodynamic loading with propeller interference," *Computes & Fluids, Palermo,* vol. 28, 8, pp. 923-950, 1999.

[13] T. Sinnige, N. V. Arnhem and T. C. A. Stokkermans, "Wingtip-Mounted Propellers: Aerodynamic Analysis of Interaction Effects and Comparison with Conventional Layout," *Journal of Aircraft,* vol. 56, no. 1, pp. 295-312, 2018.

[14] A. Jameson, "Preliminary Investigation of the Lift of a Wing in an Elliptic Slipstream," Grumman *Aerodynamics Report 393-68-6,* 1968.

[15] J. Roskam, "Methods for Estimating Drag Polars of Subsonic Airplanes," *Roskam Aviation and Engineering Corporation, University of Kansas,* 1971.

[16] S. Y. Yoo and J. C. Duensing, "Computational Analysis of the External Aerodynamics of the Unpowered X-57 Mod-III Aircraft," *AIAA Aviation 2019 Forum, California,* pp. 1-18, 2019.

[17] S. L. Schnulo, J. C. Chin and R. D. Falck, "Development of a Multi-Phase Mission Planning Tool for NASA X-57 Maxwell," *Electric Aircraft Technology Symposium, AIAA,* pp. 1-14, 2018.

[18] N. K. Borer, J. M. Derlaga and K. A. Deere, "Comparison of Aero-Propulsive Performance Predictions for Distributed Propulsion Configurations," *55th AIAA Aerospace Sciences Meeting, Grapevine,* pp. 1-16, 2017.

[19] K. A. Deere, J. K. Viken, S. A. Viken, M. B. Carter and D. Cox, "Computational Component Build-up for the X-57 Distributed Electric Propulsion Aircraft," *AIAA SciTech Forum, AIAA Aerospace Sciences Meeting, Kissimmee, Florida,* pp. 1-57, 2018.

[20] A. Filippone, "Data and performances of selected aircraft and rotorcraft," *Progress in Aerospace Sciences 36,* pp. 629-654, 2000.

[21] K. Moore and A. Ning, "Distributed Electric Propulsion Effects on Traditional Aircraft through Multidisciplinary Optimization," *AIAA Structures, Structural Dynamics, and Materials Conference, Kissimmee, FL,* doi: 10.2514/6.2018-1652, pp. 1-15, 2018.

[22] C. Courtin, M. Burton, P. Butler and A. Yu, "Feasibility Study of Short Take-off and Landing Urban Air Mobility Vehicles using Geometric Programming," *2018 Aviation Technology, Integration, and Operations Conference, Atlanta,* doi: 10.2514/6.2018-4151 , pp. 1-24, 2018.

[23] "Tecnam P2006T Aircraft Flight Manual," *Doc. No. 2006/044 4th Edition – Rev. 2 ,* 2017.

[24] "Tecnam P2006T Specification and Description," *Costruzioni Aeronautiche Tecnam SpA,* pp. 1-16, 2017.

[25] C. B. Hoover, J. Shen and A. R. Kreshock, "Whirl Flutter Stability and Its Influence on the Design of the Distributed Electric Propeller Aircraft X-57," *17th AIAA Aviation Technology, Integration, and Operations Conference, AIAA Paper 2017-3785,* pp. 1-14, 2017.

[26] M. H. Sadraey, "Aircraft design - A systems engineering approach," *John Wiley & Sons, New York,* pp. 93-160, 2012.

[27] S. Clarke, M. Redifer and T. Foster, "X-57 Power and Command System Design," *IEEE Transportation and Electrification Conference and Expo,* pp. 343-400, 2017.

[28] J. Roskam, "Airplane Design - Preliminary Sizing of Airplanes," *Roskam Aviation and Engineering Corporation, Kansas,* vol. 1, pp. 85-170, 1990.

[29] C. E. D. Riboldi and F. Gualdoni, "An integrated approach to the preliminary weight sizing of small electric aircraft," *Aerospace Science and Technology 58, Politecnico di Milano,* pp. 134-149, 2016.

[30] N. Rossi, "Conceptual Design of Hybrid-Electric Aircraft," *MSc Thesis, Politecnico di Milano, pp. 111,* 2017.

[31] M. H. Sadraey, "Aircraft Performance - An Engineering Approach," Boca Raton, FL, *CRC Press,* pp. 363-430, 2016.

[32] Borer, N. K., Nickol, C. L., Jones, F., Yasky, R., Woodham, K., Fell, J. and A. G. Samuel, "Overcoming the Adoption Barrier to Electric Flight," *54th AIAA Aerospace Sciences Meeting, AIAA SciTech 2016, San Diego, California,* pp. 1022, 2016.

[33] D. P. Raymer, "Aircraft design: a conceptual approach," *American Institute of Aeronautics and Astronautics*, Washington, DC, 1989.

[34] F. Orefice, P. Della Vecchia, D. Ciliberti and F. Nicolosi, "Aircraft Conceptual Design Including Powertrain System Architecture and Distributed Propulsion," In *AIAA Propulsion and Energy 2019 Forum,* pp. 4465, 2019.

[35] L. Trainelli, F. Salucci, N. Rossi, C. E. D. Riboldi and A. Rolando, "Preliminary Sizing and Energy Management of Serial Hybrid-Electric Airplanes," In *25th Conference of the Italian Association of Aeronautics and Astronautics, AIDAA 2019,* pp. 1510-1517, 2019.

[36] P. Della Vecchia, D. Malgieri, F. Nicolosi and A. De Marco, "Numerical analysis of propeller effects on wing aerodynamic: tip mounted and distributed propulsion," *Transportation research procedia*, vol. *29*, pp. 106-115, 2018.